
Charge-carrier Dynamics and
Surface Effects of One-dimensional
Cadmium–Chalcogenide Nanostructures

DISSERTATION

for the attainment of the degree

doctor rerum naturalium

(Dr. rer. nat.)

submitted by

Svenja Patjens

Fakultät für Mathematik, Informatik und Naturwissenschaften

Institut für Physikalische Chemie

Universität Hamburg

Hamburg, 2023

Gutachter der Dissertation

Prof. Dr. Alf Mews
Prof. Dr. Christian Klinke

Gutachter der Disputation

Prof. Dr. Alf Mews
Prof. Dr. Dorota Koziej
Dr. Tobias Vossmeier

Datum der Disputation

14.04.2023

Datum der Druckfreigabe

14.04.2023

Abstract

Semiconductor nanowires are auspicious as active components of electronic or optoelectronic devices. Tailoring of the optical and electrical properties can be achieved by tuning the nanowire diameter and thus employing the size-quantization effect. The surface of colloiddally synthesized nanowires is saturated with organic ligands that promote directional growth and passivate trap states. Consequently, the surfactants provide means to influence the morphology and the spectral characteristics of the semiconductor nanostructures.

Here, the fabrication and spectroscopical analysis of CdTe, CdSe and CdS nanowires and heterostructures thereof were conducted and correlated to the utilized ligand system in order to unveil the structure–property relation. The photoluminescence of native ligand-capped CdTe-nanowires was investigated at cryogenic temperatures, revealing feature-rich emission lines that entail a concerted series of NIR replicas. These replicas were allocated to vibrational modes of the organic surfactants. Ligand-exchange reactions were employed to manipulate the nanostructure surface post-synthetically, while retaining the coordinating effect of the original ligands during crystal growth. The anorganic ligand-exchange reaction was used to compose CdSe/CdS core/shell hetero-nanowires with precise shell dimensions. However, customization of the synthesis-ligand system enabled the reduction of the trap-induced emission in CdS nanowires, while obtaining nanowires with compatible morphologies. By using multi-modal X-ray microscopy, the electrical response of the catalytically grown nanowires could be correlated to the elemental distribution of the lithographically contacted sample.

Careful modification of both, the synthesis and the passivation ligand system can provide a useful tool to further design the optical properties of nanostructures beyond dimension tuning. Especially the anorganic ligand-exchange reaction renders a high degree of customization potential and as such is well suited to advance the applicability of nanowires in functional devices such as photosensors.

Zusammenfassung

Halbleiter-Nanodrähte sind vielversprechende aktive Komponenten für elektronische und optoelektronische Bauteile. Die optischen und elektrischen Eigenschaften von Nanodrähten können angepasst werden, indem der Nanodrahtdurchmesser variiert wird und der damit einhergehende Größenquantisierungseffekt zum Tragen kommt. Die Oberfläche von kolloidal synthetisierten Nanodrähten ist mit organischen Liganden abgesättigt, die zum Einen gerichtetes Wachstum unterstützen und zum Anderen Fehlstellen passivieren. Die Liganden ermöglichen somit eine Einflussnahme auf die Morphologie und die spektralen Eigenschaften der Halbleiter-Nanodrähte.

In dieser Arbeit wurden die Herstellung und die spektroskopische Analyse von CdTe-, CdSe- und CdS-Nanodrähten sowie daraus gebildete Heterostrukturen unter Anbetracht des verwendeten Ligandensystems korreliert, um somit die Struktur-Eigenschafts-Beziehung herauszuarbeiten. Die Photolumineszenz der nativ ligierten CdTe-Nanodrähte wurde bei tiefen Temperaturen untersucht, wodurch facettenreiche Emissionlinien mit dazugehörigen Repliken im NIR-Bereich offenbart wurden. Diese Repliken wurden den Vibrationsmoden der organischen Liganden zugeordnet. Es wurden verschiedene Ligandenaustauschreaktionen durchgeführt, um die Oberfläche der Nanostrukturen nach der Synthese zu manipulieren, wodurch der koordinierende Effekt der Originalliganden während des Kristallwachstums erhalten blieb. Unter Anwendung der anorganische Ligandenaustauschreaktion konnten CdSe/CdS Kern/Schale Heterodrähte mit wohldefinierten Schalenabmessungen entwickelt werden. Auch durch Anpassen des Syntheseligandensystems konnte die fehlstelleninduzierte Emission der CdS-Nanodrähte reduziert werden, während die Morphologie der so synthetisierten Nanodrähte vergleichbar blieb. Mit Hilfe von multimodaler Röntgenmikroskopie konnte die elektrische Antwort der katalytisch gewachsenen Nanodrähte mit der Verteilung der Elemente auf der lithografisch kontaktierten Probe korreliert werden.

Die behutsame Modifizierung sowohl des Synthese- als auch des Passivierungsligandensystems kann für die weitere Optimierung der optischen Eigenschaften der Nanodrähte abseits der Manipulation ihrer Dimensionen eine Stellschraube bieten. Insbesondere die anorganische Ligandenaustauschreaktionen bieten ein hohes Maß an Anpassungspotential und ist deshalb für die Weiterentwicklung von Nanodrähten bezüglich ihrer Verwendungsmöglichkeiten in verschiedenen Bauteilen wie zum Beispiel Photosensoren gut geeignet.

Contents

List of Figures	III
List of Tables	V
1 Introduction	1
2 Theoretical Considerations	3
2.1 Structural and Optical Properties of Semiconductors . . .	3
2.1.1 Band Structure	4
2.1.2 Crystal Structure	4
2.1.3 Interband Transitions	6
2.2 Semiconductor Nanostructures	8
2.3 Semiconductor Heterostructures	10
2.4 PL Properties of Cadmium Chalcogenides	12
2.4.1 Temporal Characteristics	12
2.4.2 Spectral Characteristics	14
2.5 Colloidal Synthesis of Quantum Nanowires	16
2.5.1 Solution-Liquid-Solid Method	16
2.5.2 Surface Modification	18
3 Methods	20
3.1 Confocal Scanning Microscopy	20
3.1.1 Excitation Unit	22
3.1.2 Confocal Scanning Setup	23
3.1.3 Cryostat	25
3.1.4 Detection Unit	25
3.2 Structural Analysis of Nanostructures	27
3.2.1 Electron Microscopy	27
3.2.2 Atomic Force Microscopy	29
3.2.3 X-ray Diffraction	30
3.2.4 X-ray Fluorescence Spectroscopy	32
3.2.5 Analysis of X-ray Beam Induced Current	34
3.2.6 Thermogravimetric Analysis	36

4	Experimental Details	37
4.1	Synthesis	37
4.1.1	Synthesis of Metal-Catalyst Particles	37
4.1.2	Synthesis of Precursors	38
4.1.3	Synthesis of Cadmium Chalcogenide NWs	39
4.2	Surface Modification	40
4.2.1	Ligand Removal via Thermogravimetric Analysis	40
4.2.2	Organic Ligand-Exchange Reaction	40
4.2.3	Colloidal Atomic Layer Deposition	41
4.3	Procedures	42
4.3.1	Sample Preparation and Device Fabrication	42
4.3.2	Structural Analysis	43
4.3.3	Chemicals	46
5	Results and Discussion	47
5.1	Photoluminescence of CdTe QNWs	48
5.1.1	Spectral Intermittency in CdTe QNWs	57
5.1.2	Surface Characteristics of CdTe NWs	60
5.2	Anorganic Ligand Exchange Reaction	72
5.3	Influence of the Synthesis Ligand-System	88
5.4	X-ray Microscopy Analysis of SLS-QNWs	97
6	Summary	110
	Bibliography	112
	Appendices	129
A	Safety and Disposal	129
B	Conference Contributions	134
C	Acknowledgments	135
D	Eidesstattliche Erklärung	137

List of Figures

2.1	Energy diagram of solids	4
2.2	WZ and ZB crystal structure	5
2.3	Electronic characteristics of semiconductors	6
2.4	Density of states for quantum structures	8
2.5	Semiconductor Hetero NWs	11
2.6	PL intermittency of colloidal NPs	13
2.7	Spectral broadening of colloidal NPs	14
2.8	Schematic of the SLS mechanism	16
2.9	Reaction scheme of colloidal atomic layer deposition	19
3.1	Schematic of a confocal setup	21
3.2	Schematic of the low-temperature confocal setup	22
3.3	Schematic of the closed-cycle cryostat	25
3.4	Schematic of a TEM	27
3.5	Schematic of electron-matter interaction	28
3.6	Schematic of an AFM	29
3.7	Lennard-Jones potential	30
3.8	XRD-reference data for CdTe	31
3.9	Principle of X-ray fluorescence	32
3.10	Energetic levels in a typical semiconductor	34
3.11	Principle of XBIC and XRF measurements	35
5.1	Electron Micrographs and band alignment of CdTe QNWs	48
5.2	CdTe QNWs synthesized with halogenated alkanes	50
5.3	XRD of CdTe QNWs	51
5.4	Spectral series of CdTe QNWs	53
5.5	Example PL spectrum of bulk CdTe at 5 K	55
5.6	Temporal evolution of the high-energy signals	57
5.7	Model calculation for the WZ/ZB potential landscape	59
5.8	Vibrational characteristics of the organic medium	61
5.9	TGA of organic ligands and the CdTe/Lig NWs	66
5.10	Vibrational characteristics of the CdTe/Lig NWs	68
5.11	NMR spectra of ligand-exchanged CdTe NWs	71
5.12	Absorption and size distribution of CdSe/ x CdS NWs	73

5.13	Influence of CdSe NW diameter	75
5.14	Emission wavelength of CdSe/ <i>x</i> CdS NWs	76
5.15	Micrographs of CdSe/CdS core/shell NWs	77
5.16	High-resolution micrographs of core/shell NWs	78
5.17	XRD of CdSe/ <i>x</i> CdS NWs	80
5.18	PL decay curves of CdSe/ <i>x</i> CdS NWs	82
5.19	Spectrally resolved map of CdSe and CdS NWs	84
5.20	PL intensity map of CdS NWs	85
5.21	Typical spectrum of CdS	88
5.22	PAs utilized for the synthesis of CdS NWs	89
5.23	PA-dependent structural characteristics of CdS NWs	90
5.24	Influence of ligand chain length on the optical properties	92
5.25	Radiative and non-radiative recombination	93
5.26	TGA of PA-covered CdS NWs	95
5.27	Sample architecture and setup	97
5.28	XRF sum spectrum of the contacted CdTe NW	99
5.29	Maps of the contacted CdTe NW	101
5.30	High magnifications SEM image	102
5.31	XRF-analysis of Bi and Pt L-lines	103
5.32	Scheme of XBIC setup	105
5.33	Comparison of lock-in and direct XBIC	106
5.34	Direct XBIC profile along the NW	108

List of Tables

2.1	Characteristics of cadmium chalcogenides	7
4.1	Beamline Settings	44
4.2	Utilized Chemicals	46
5.1	Reference XRD reflexes of CdTe	52
5.2	IR vibrational frequencies of the ligands	63
5.3	IR vibrational frequencies of the cadmium complexes	65
5.4	Diameter increment per c-ALD cycle	74
5.5	Reference XRD reflexes of CdSe and CdS	80
5.6	Lifetime parameters of CdSe/ <i>x</i> CdS NWs	82
5.7	Reference XRD reflexes of CdS	91
5.8	X-ray absorption edges	98
5.9	Characteristic X-ray transitions	100
5.10	X-ray absorption edges of the sample compounds	103
A.1	Safety instructions of the utilized chemicals	129

1 | Introduction

The ongoing miniaturization of electronic devices and the conjoined performance enhancement promise eminent potential for information technology and environmental science.^[1,2] The individual nanostructures are conceptualized to have a limited extend of at least one dimension in the range of 1–100 nm. These nano-scaled materials exhibit size-tunable properties that differ from the well-known characteristics of the corresponding bulk materials. While this class of materials is in principle established, novel nanostructures emerge frequently due to advances in synthesis. To exploit the full capacity of the nanoscopic components, the materials paradigm, namely the interrelation between processing, structure, properties, and performance, must be elucidated.

One-dimensional nanostructures such as nanowires (NWs) are particularly viable for opto-electronic applications such as sensors,^[2–6] photovoltaics,^[7,8] and photonics.^[9–11] The elongated geometry bridges both, the nanoscopic and the microscopic regime, thus promoting the implementation of nanowires in functional devices, as electrical contacting is comparably facile. The stark anisotropy may introduce polarization dependence, which further advances the sensitivity of photonic applications.^[12,13]

Owing to their direct band gaps in the visible range of the electromagnetic spectrum, cadmium chalcogenide semiconductors are of particular interest. For these II-VI compound semiconductors, economically suitable colloidal-synthesis routes have been developed. The solution–liquid–solid method allows for size-tunability and tailoring of surface properties.^[14] The inorganic/organic interface can further be modified using a self-limiting ligand-exchange protocol, which facilitates substitution of the original surfactants with organic molecules exhibiting different binding motifs or even inorganic ions. In a sequential exchange approach, even a complete inorganic shell having a thickness of several monolayers may be fabricated using colloidal atomic-layer deposition.^[15,16] By combining different materials, a variety of core/shell heterostructures can be designed as to enable the precise modification of the band alignment and the passivation of shallow trap states.^[17,18]

Further, CdE (E = S, Se, and Te) NWs typically exhibit both, wurtzite and zinc blende lattice modification. The alternation of crystallographic segments along the wire-axis results in an axial potential landscape due to the respective band gaps associated with the different lattice spacings of the two structures.^[19] This polytypism introduces crystallographic defects, such as stacking faults and twinning boundaries, which reduce the charge-carrier mobility and lifetime.^[20–22]

To identify structural characteristics that are detrimental to the optical quality, the evaluation of the optical properties has to be conducted on the single-particle level. Especially the photoluminescence intermittency of colloidal nanocrystals impairs the fluorescence quantum yield.^[23,24] While the defect-mediated processes, such as Auger recombination and surface trapping, can hardly be observed in ensemble measurements due to averaging-effects, a detailed analysis of their origins is necessary in order to further advance optical quality.^[25]

In this thesis, the optoelectronic properties of solution-based NWs were investigated with respect to surface characteristics and crystal structure alternations. For a detailed analysis of the charge-carrier dynamics, the photoluminescence of CdTe NWs having mainly wurtzite conformation was investigated at cryogenic temperatures. Postsynthetical surface treatments were conducted to gain insight into the effect of the NW–ligand interaction. Additionally, CdSe/CdS core/shell NWs were synthesized and spectroscopically analyzed as a model-system for one-dimensional heterostructures. Furthermore, the effect of varying surfactants introduced during synthesis of CdS NWs was studied. Due to the surface defects being energetically close to the band edges in CdS, the trap emission band is located in the visible region of the spectrum. The relative intensity of this defect band with respect to the near band-edge emission may serve as a means to estimate defect density.^[26–28] Thus, the passivation efficiency of the different ligands may be directly ascertained. Concludingly, the electrical performance of a CdTe NW sample was correlated to the elemental composition by simultaneously monitoring the X-ray beam induced current and the X-ray fluorescence in a multi-modal synchrotron-based experiment.

2 | Theoretical Considerations

The investigation of the structural and optical properties of one-dimensional binary semiconductor nanostructures has been the objective of this work. In the first part of this chapter, a brief theoretical background concerning the characteristics of solid-state materials is presented. The second section provides an introduction to the nature of quantum confined particles and the optical properties of these nanostructures. Subsequently, the possibility to tailor the fluorescence characteristics by using semiconductor heterostructures is illustrated. In a final section, the colloidal synthesis of nanowires is described.

2.1 Structural and Optical Properties of Semiconductors

Solid-state materials can be described by presuming a periodical arrangement of atoms in a crystal lattice. The interatomic distance is equivalent to the lattice constant in the unit cell, which is approximately equal to the size of the constituent atoms. Thus, the outer orbitals of said atoms overlap, giving rise to new wavefunctions through linear combination of atomic orbitals (LCAO).^[29]

These newly formed molecular orbitals define the electronic levels of the crystal and thus, the band structure. Depending on the arrangement of the bands and the resulting band gap, solids can be classified into metals, semiconductors and insulators. The size of the band gap is not only influenced by the elemental configuration, but also by the geometric arrangement of the atoms within the lattice and consequently, the crystal structure. Because the optical properties of a solid strongly depend on the structural properties of the material, the origin of the band structure and details about the crystal lattices typically found in the sample system discussed in this thesis are illustrated in the following sections. After the structural nature of the solid-state materials has been contemplated, the corresponding optical characteristics will be elucidated.

2.1.1 Band Structure

In a macroscopic crystal, a multitude of atoms contribute to the formation of the band structure that represents a continuum of electronic levels within the solid. The atoms are considered to consist of immobile positively charged ions and of electrons. The atomic orbitals spatially overlap in dependence on the interatomic distance. The electrons of the individual atoms contributing to the solid have to differ in quantum numbers as is stated in the Pauli exclusion principle. Consequently, the orbitals of the N atoms split into N closely-spaced discrete electronic levels. While several of these quasi-continuous bands arise in a macroscopic solid, the inert core bands are usually neglected as the periodic potential introduced by the ionic cores reduces the interaction strength of the more tightly bound core electrons. The movement of the valence electrons, however, is conceptualized to be nearly free as the static potential of the crystal lattice only evokes a weak perturbation, resulting in the formation of broad bands.^[30]

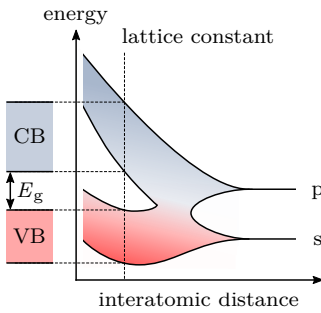


Figure 2.1: Energy diagram of solids. The electronic band structure and thus the size of the band gap E_g is dependent on the interatomic distance. The discrete electronic levels of the N single atoms evolve into continuous bands with decreasing spacing between atoms as the spatially overlapping atomic orbitals split into N levels with different energies due to the Pauli exclusion principle.

These continuous bands are separated by regions of forbidden energy ranges as is illustrated in Figure 2.1. The fundamental band gap E_g of a solid is energetically situated near the Fermi level E_F of the system, which is the chemical potential of the electrons at zero absolute temperature. Depending on the width of the band gap, solid-state materials are classified into metals, semiconductors and insulators. In semiconductors, the electronic bands below and above the band gap are denoted valence band (VB) and conduction band (CB), respectively. The distribution of electronic levels and thus the size of the band gap is influenced by the interatomic distance as can be deduced from Figure 2.1. Consequently, the temperature dependency of the lattice spacing, quantified by the linear expansion coefficient, results in a modulation of the band structure with thermal energy.^[31,32]

2.1.2 Crystal Structure

The crystal structure of a solid-state material consists of symmetric patterns of atoms forming a unit cell. Due to the periodical arrangement of the unit cell throughout the lattice, this smallest building block depicts the structure of the complete crystal. The nanostructures investigated during the course of this thesis are either II–VI or III–V binary semiconductors. These subclasses are known to form both wurtzite (WZ) and zinc blende (ZB) lattices. The former exhibits a hexagonal close packed (hcp) geometry, while the latter has a face centered cubic (fcc) structure.

Both systems have a tight arrangement of atoms amounting to the highest packing density of 0.74. They differ only slightly through the relative displacement of their hexagonal layers, resulting in individual stacking orders. On the vertices of a densely packed sheet of spheres, two relative placements of the successive plane are possible. Contemplating a stacking of layers A (gray) and B (white) as in Figure 2.2, the spheres of a third plane can be situated either exactly above those in the first layer or in the vertices being occupied by none of the preceding layers. The resulting stacking sequences ABABAB... and ABCABC... correspond to the WZ (blue) and ZB (turquoise) structure, respectively. From these different sequences, a zig-zag like or a slanted appearance of the side facets of the crystal arises. This phenomenon can be utilized to determine the crystal structure of a given nanostructure in detail. In binary semiconductors like cadmium chalcogenides, the individual atom types build the same sublattice structure with the atoms of one type being located in the tetrahedral voids formed by the sublattice of the counterion.^[31,33]

The morphology of nanocrystals (NCs), however, is not only governed by the nature of the constituent elements, but also by the surface of the structure. Colloidal synthesis poses a suitable means for phase control through the introduction of different organic surfactants. Typically, the WZ phase is considered to be the more stable and thus prevalent configuration of cadmium chalcogenide NCs such as CdSe and CdS. However, also the metastable ZB phase may be thermodynamically stabilized by careful choice of coordinating ligands.^[34] The binding motif between organic molecule and inorganic structure is of considerable importance as it may well influence the majority type of surface ions and thereby promote a specific crystal phase.^[35]

Further synthesis parameters such as reaction temperature and stoichiometry may contribute to kinetically controlled crystallization. In case of catalyst-assisted growth methods, the interrelation may be rendered even more complex due to the introduction of new interfaces. Additionally, the nucleation barriers of WZ and ZB cadmium chalcogenides are near-equal and the small difference may easily be overcome by inconsistencies of nucleation conditions during colloidal synthesis as will be discussed further in Section 2.5.^[36] The resulting polymorphous structures may exhibit varying band gaps contingent on the crystallographic conformation related to the lattice spacing. This is of particular interest in case of polytypic particles that comprise several domains having different crystal structures as will be elaborated in greater detail in Section 2.3.

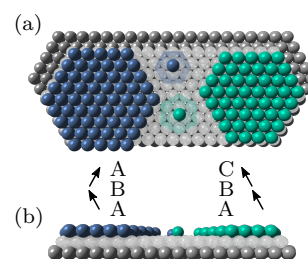
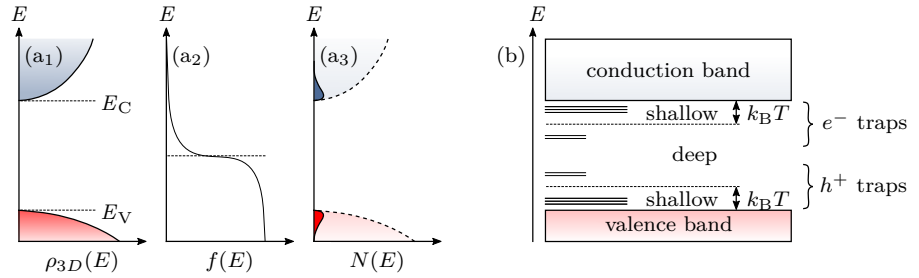


Figure 2.2: Placement of hexagonal layers in WZ and ZB structure. The position of the first (gray) and second (white) layer are similar for both cases. In case of WZ (blue) the spheres in the third layer are positioned exactly above those in the first plane. In a ZB (turquoise) structure the spheres of the third layer are situated in the vertices that are not occupied yet.

2.1.3 Interband Transitions

In a semiconducting material, an electron can be elevated from the VB into the CB across the fundamental band gap, while rendering the initial state unoccupied. The positively charged vacancy, the so-called hole, is equivalent to a quasi-particle that is similar to an electron. However, these electron–hole pairs can only be generated if the incident energy exceeds the band gap. Furthermore, direct and indirect interband-transitions have to be differentiated as not only the conservation of energy but also that of crystal momentum has to be satisfied.

Figure 2.3: Electronic characteristics of semiconductors. Based on the DOS (a₁) and the F–D distribution (a₂), the number of occupied states (a₃, grey) can be calculated for both electrons (blue) and holes (red). Additional electronic levels in the band gap originate defect states (b).



In direct semiconductors, such as the compound materials analyzed in this thesis, the transition rate is strongly dependent on the density of states (DOS), which is schematically represented in Figure 2.3a₁ for the 3D case. This probability density function ρ_{3D} expresses the number of energy levels in a system with a given volume, while the Fermi–Dirac (F–D) distribution $f(E)$ that is illustrated in Figure 2.3a₂ provides the number of fermions occupying a state with energy E at thermodynamic equilibrium. Contemplating both the DOS and the F–D distribution, the electron density N_e (Figure 2.3a₃) can be calculated as

$$N_e = \int_{E_C}^{\infty} \rho_{3D} f(E) dE = N_C \exp\left(\frac{E_F - E_C}{k_B T}\right), \quad (2.1)$$

including the Boltzmann constant k_B and temperature T as well as the temperature-dependent concentration coefficient N_C . The latter can be interpreted as the effective density of states that is dependent on the electronic effective mass m_e^* and the reduced Planck constant \hbar :

$$N_C = 2 \left(\frac{m_e^* k_B T}{2\pi \hbar^2} \right)^{3/2}. \quad (2.2)$$

The movement of the charge carriers in the crystal lattice is conceptualized by approximating them as free particles having effective masses m^* that account for the periodic potential.^[33]

These effective masses, and thereby the charge-carrier mobility, can be estimated by calculating the second derivative of the usually parabolic energy dispersion of the respective bands. If the Coulomb interaction between the oppositely charged particles is sufficient for the formation of a bound electron–hole pair, the charge carriers can be treated as a quasi-particle called an exciton. Contingent on the interaction strength, and consequently the radius of the electron–hole orbit, tightly bound Frenkel excitons and free Wannier–Mott excitons can be discriminated. While the former are highly localized and are primarily found in molecular crystals with low dielectric constants, the latter typically occur in semiconductors and extend over several unit cells due to the high dielectric screening in these crystals. By conceptualizing the exciton in analogy to the hydrogen atom and adapting the equation of the Bohr radius a_{H} to account for the dielectric constant ϵ_{r} of the medium and the reduced mass μ of the quasi-particle, the equilibrium distance $r(n)$ between the carriers with charge q forming this delocalized neutral complex may be estimated:^[37]

$$r(n) = n^2 a_{\text{X}} = n^2 \frac{\epsilon_{\text{r}} m_0}{\mu} a_{\text{H}} = n^2 \frac{4\pi \hbar^2 \epsilon_0 \epsilon_{\text{r}}}{q^2 \mu}. \quad (2.3)$$

The exciton Bohr radius a_{X} describing the ground state with quantum number $n=1$ as well as the effective masses, the band-gap energy and the lattice constants a for WZ and ZB structure of the cadmium chalcogenide materials investigated in this thesis are listed in Table 2.1. The exciton binding energy effectively reduces the recombination energy, thus introducing electronic states in the classically forbidden band gap. However, the delocalized free excitons exhibit Rydberg energies at the order of 10 meV and are consequently only observable at conditions well below room temperature (RT).^[30,40]

In addition to the excitonic reduction of the effective band gap, electron and hole trap states may introduce electronic levels below the CB edge and above the VB edge, respectively. As is illustrated in Figure 2.3b, shallow and deep defect-states can be discriminated for both charge carriers. The shallow levels are typically located in close proximity to the respective band edge and are thermally ionized at RT. If introduced by impurity elements, these states may provide free carriers and thus contribute to doping of the semiconductor. The deep levels, however, exhibit higher ionization energies than $k_{\text{B}}T$ and often impair the opto-electronic properties by acting as recombination centers.^[33,41–43]

Table 2.1: Characteristics of cadmium chalcogenides. The lattice constant a is provided for both WZ (top) and ZB (bottom) crystal configuration. The electronic properties are specified for the prevalent crystal structure.^[38,39]

	CdTe	CdSe	CdS
a	4.57	4.30	4.14
$/\text{\AA}$	6.48	6.05	5.82
E_{g}			
$/\text{eV}$	1.6	1.74	2.42
m_{e}^*			
$/m_0$	0.11	0.13	0.20
m_{h}^*			
$/m_0$	0.41	0.45	0.70
a_{X}			
$/\text{nm}$	6.7	5.4	2.7

2.2 Semiconductor Nanostructures

So far, solid-state materials have been described on the basis of their structural properties. However, material size and geometry also have an impact on the electronic and optical characteristics of nanoscaled semiconductors. Miniaturization of the material towards the wavelength of the electron wave evokes new properties that deviate from those of both the corresponding bulk structure and single molecules. In the resulting intermediate system, the motion of the charge carriers within their respective bands is restricted. Consequently, only a finite number of states per volume element and energy can be occupied. The functional form of this DOS is influenced by the degrees of dimensionality. Quantum structures can thus be classified by the number of reduced dimensions of charge-carrier propagation. The resulting types and the respective DOS functions are illustrated in Figure 2.4.^[30,44]

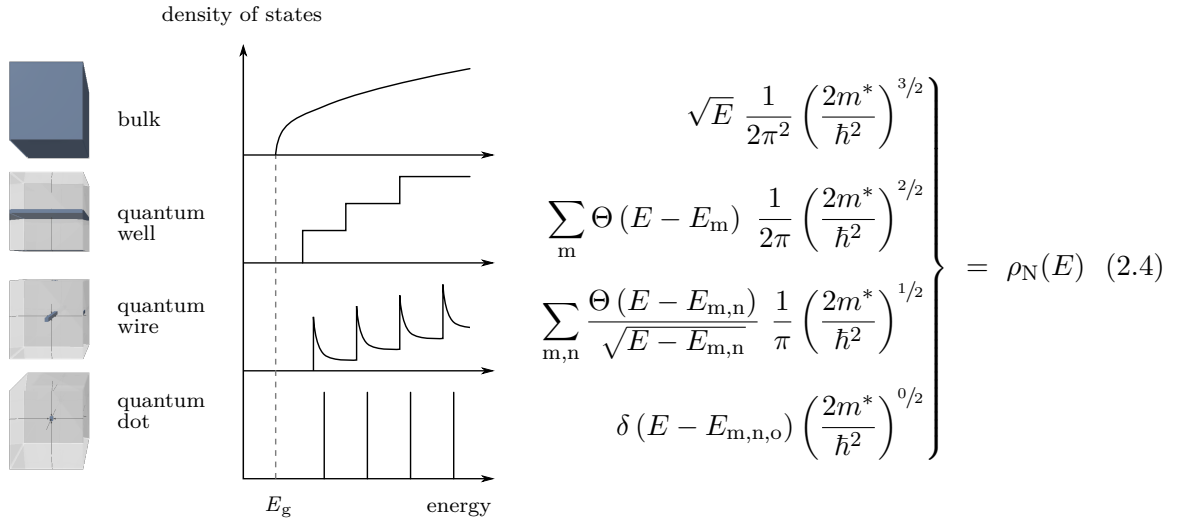


Figure 2.4: Density of states of quantum structures. The various quantum structures and their corresponding DOS functions for electrons are sketched.

A conventional particle with sufficiently large dimensions and thus three degrees of freedom may be considered as bulk material. If the charge carriers are confined in one dimension as is the case in a 2D quantum well, the continuous bulk DOS ρ_{3D} is altered to a Heaviside step function θ . Interestingly, the DOS is independent of the energy within each quantization level in quantum wells. As free motion is only possible in one dimension in a quantum wire, the DOS is changed to include a reciprocal decrease between the jumps. The DOS of fully confined quantum dots exhibits discrete quantized levels that are represented by a Dirac δ -function.^[45]

Not only the degree of dimensionality but also the extend of the quantum structure along the reduced axes influences the optical properties of these materials. The size-dependent energetic levels of the quantized states in conduction and the valence band may be described by applying the particle in a box model. The potential acting on the particle is zero inside of the box, while it presents as infinitely high potential walls that confine the particle to the box. For a one-dimensional system, the time-independent Schrödinger equation

$$\left(-\frac{\hbar^2}{2m^*} \cdot \frac{\partial^2}{\partial x^2} + V(x) \right) \Psi(x) = E\Psi(x) \quad (2.5)$$

renders the energy eigenvalue of the quantized motion. To account for the approximately spherical shape of quantum dots, a spherical coordinate system should be utilized. After separation of the Schrödinger equation into a radial and an angular part, the energy levels occurring in a particle with radius r can be extracted:^[46,47]

$$E_n = \frac{n^2 \hbar^2 \pi^2}{2m^* r^2}. \quad (2.6)$$

Due to their differences in effective mass m^* , the kinetic energy has to be calculated for both charge carriers separately. Because the effective mass of the electron is usually significantly lower than that of the hole, the kinetic energy of the electron with its corresponding higher mobility is much more subject to changes in particle size. The energy level spacing in both VB and CB is increased in particles with small radii due to this confinement energy. Contemplating the Coulomb interaction between electron and hole and the confinement energy and the energy of the bulk band gap E_g , the effective energy gap E_g^* can be calculated as

$$E_g^* = \underbrace{E_g}_{\text{bulk band gap}} + \underbrace{\frac{\hbar^2 \pi^2}{2} \left(\frac{1}{m_e^*} + \frac{1}{m_h^*} \right) r^{-2}}_{\text{confinement}} - \underbrace{\frac{1.8e^2}{4\pi\epsilon_0\epsilon_r} r^{-1}}_{\text{Coulomb}}, \quad (2.7)$$

with the factor 1.8 accounting for the spherical geometry of the particle.^[48] In addition to this geometrical limitation, the dielectric coating of the nanostructures may provide a finite potential step at the nanocrystal–ligand interface, consequently rendering Equation 2.7 postulated by Brus et al. deficient, as it applies to the model system of an infinite potential well. Similarly, nanoscopic inorganic core/shell heterostructures can only be inchoatly described by the equation.

2.3 Semiconductor Heterostructures

The opto-electronic properties of nanoparticles (NPs) may be precisely tailored by designing heterostructures that consist of differing semiconductor materials. Especially colloiddally synthesized nanoparticles often exhibit poor fluorescence quantum efficiency due to the insufficient passivation of surface traps. These trap states originate from the lower coordination number of the surface atoms. The dangling bonds at the unsaturated cationic and anionic sites may trap electrons and holes, respectively, and thus, increase non-radiative recombination. Surface ligation with organic molecules employed for precursor complexation and growth control during synthesis is usually incomplete due to steric hindrance between the surfactants. Furthermore, only one species of surface atoms may be passivated efficiently. Epitaxial layers of a semiconductor can substitute the organic ligands and coordinate both surface species of the original structure and thus increase the photoluminescence quantum yield by saturating the dangling orbitals.^[49] Additionally, the location of the charge carriers within the heterostructure and consequently the radiative lifetime can be influenced by careful combination of the different components.^[50]

Depending on the relative band alignment of the materials, semiconductor heterojunctions are classified into different types, namely straddling, staggered and broken gap structure. The junction geometry of a given combination of material A and B can be estimated by leveling the vacuum energies of the components and thus, retrieving the CB offset from the respective electron affinities χ in accordance to Anderson's rule:

$$\Delta E_{CB} = E_{CB,B} - E_{CB,A} = \chi_B - \chi_A. \quad (2.8)$$

Subsequently, the VB offsets can be calculated contemplating the band gap values.^[51]

In a type-I (straddling) structure, the band edges of the small band gap material are situated within the band gap of the other semiconductor. Thus, both charge carriers are contained to the same component. In a type-II (staggered) structure, however, both VB and CB edge have elevated energies with respect to the second semiconductor. This configuration effectively evokes charge-separation as electron and hole are spatially localized in the material with the lower CB edge and higher VB edge, respectively. A type-III (broken gap) alignment presents an extreme case of a staggered junction in which the band gaps do not overlap.

Semiconductor hetero-NWs can be realized with different geometries, which are represented in the top row of Figure 2.5. In the bottom row, the band alignment of typical material combinations and the corresponding electron (blue) and hole (red) wavefunctions are sketched. The most prominent configuration in colloidal chemistry is the core/shell structure, which is obtained by coating the preexisting particles (cores) with epitaxial layers of a second material (shell). As stated above, this procedure is well suited to improve the fluorescence efficiency and modify the effective band gap energy, especially when opting for a type-I alignment. Anisotropic nanostructures such as NWs allow for improved charge-carrier separation if the type-II junction is aligned with their long axes. Due to their extended geometry, block NWs are comparably easy to contact with electrodes and may thus be utilized in opto-electronic devices.

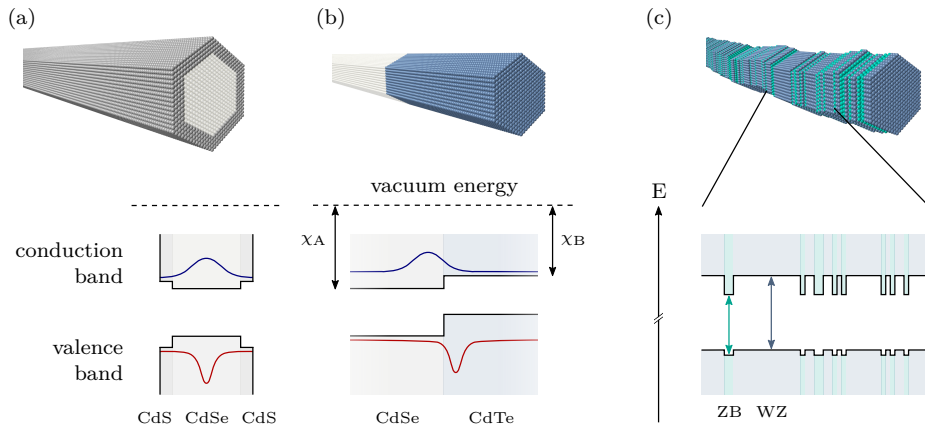


Figure 2.5: Schematic of various hetero NWs. Geometric layout (top) of core/shell (a) block (b) and polytypic NWs (c) and the respective resulting band alignment (bottom). The electron (blue) and hole (red) wavefunctions are sketched for a type-I (a) and type-II (b) heterojunction. The depiction of the quasi-type-II band alignment resulting from the crystal phase alternations is not quantitatively scaled.^[20]

Finally, colloiddally synthesized NWs present an alternating potential landscape due to their polytypic growth. The crystal structures do not only differ in nucleation energy but also in the size of their band gap. In case of CdTe, bulk values of 1.654 eV and 1.607 eV at low-temperature were reported for WZ and ZB, respectively.^[36] Based on a CB offset of 65 meV, these wires are aligned in a quasi-type-II structure. However, the phase alternations in CdTe NWs are usually frequent and especially the ZB segments consist of only a few monolayers. Consequently, the charge-carrier separation may be ineffective and the NW might have to be treated as a single structure with an average band gap instead of a heterostructure with separate domains as was reported for CdSe NWs.^[19]

2.4 Photoluminescence Properties of Cadmium Chalcogenide Nanocrystals

In this section, the temporal and spectral characteristics of the photoluminescence (PL) originating from semiconductor NPs will be elucidated. While tuning of the band gap is well established nowadays, the PL quantum efficiency and the optical stability of cadmium chalcogenide nanostructures are still to be advanced. The PL properties of colloidal nanocrystals have been reported to depend strongly on surface characteristics such as trap states and ligation.^[52,53]

2.4.1 Temporal Characteristics

The aspired radiative recombination is superseded by non-radiative decay processes, resulting in a reduction of quantum yield η_r as is theorized in Equation 2.9. The decay rates τ_r and τ_{nr} associated with the competing radiative and non-radiative cases, respectively, both contribute to the PL efficiency of the semiconductors. The depopulation of the excited state can be devised as a reaction of first order, translating to an exponential decrease in PL intensity as a function of time. For multi-exponential decays accounting for different recombination channels i , the average lifetime $\bar{\tau}$ can be determined according to Equation 2.10 using the pre-exponential factor α_i that indicates the individual amplitudes at $t = 0$. Furthermore, the fractional contributions f_i related to each decay time τ_i can be deduced accordingly.^[54] When contemplating the PL dynamics of colloidal NPs, dark states introduced by fine-structure splitting of the excitons in cadmium chalcogenide nanostructures and fluorescence intermittency associated with Auger recombination have to be discriminated.

$$\eta_r = \frac{1}{1 + \tau_r/\tau_{nr}} \quad (2.9)$$

$$\begin{aligned} \bar{\tau} &= \frac{\sum_i \alpha_i \tau_i^2}{\sum_i \alpha_i \tau_i} \\ &= \sum_i f_i \tau_i \end{aligned} \quad (2.10)$$

In case of pure excitonic recombination, the fine structure can be modeled by a three-level system involving a ground level and two individual excited levels, which account for the optically active (bright) and the optically forbidden (dark) state.^[55] Because the bright–dark splitting energy ΔE_{BD} that separates the latter is typically in the range of a few meV, mixing of these excited states occurs at RT by thermally induced redistribution of the level population. At cryogenic temperatures ($\Delta E_{BD} \gg k_B T$), bright and dark excitons can be distinguished based on the bi-exponential behavior of the fluorescence lifetime signal. Depending on the oscillator strength of the excited states, the short and long component can be attributed to bright and dark excitonic recombination, respectively.^[56,57]

The distinct intensity fluctuations of colloidal NPs known as fluorescence intermittency or blinking are theorized to be caused by randomly occurring ionization and neutralization events that render the fluorophores in charged "off" and neutral "on" conformation. The resulting intensity fluctuations of a single emitter that are schematically illustrated in the time trace in Figure 2.6a can be classified into bright "on" (turquoise) and dark "off" (green) periods by selecting a threshold "th" (yellow).

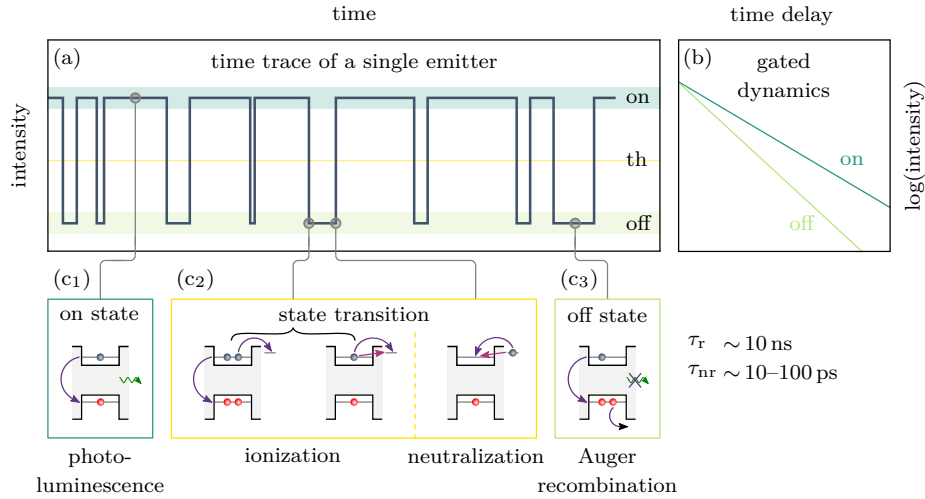


Figure 2.6: PL intermittency of colloidal NPs. Schematic intensity fluctuations of a single nanocrystal exhibiting an "on" state (blue) and an "off" state (green) (a) that entail distinct decay dynamics (b) that can be ascertained by gating the recorded time trace using a threshold (th, yellow). The "on" state (c_1) is presumed as a neutral nanocrystal, while the "off" state (c_3) is theorized to result from a charged nanocrystal that promotes Auger recombination. State transitions (c_2) associated with blinking arise from ionization ("on" \rightarrow "off") and neutralization ("off" \rightarrow "on") events. Adapted from ref. [23]

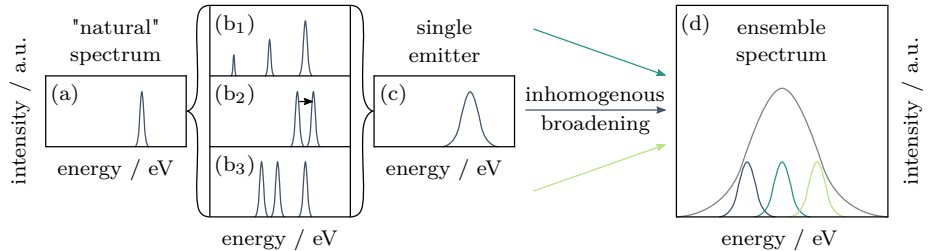
The bright "on"-state (c_1) comprises the classical PL mechanism with charge-carrier recombination in a neutral semiconducting environment. The dark "off" state (c_3) is associated with Auger-assisted recombination in the presence of electric field on the order of MV cm^{-1} that is induced by charge separation and, ultimately, excess charges in the nanostructure. The extra carrier can be presumed as a third body that facilitates three-particle recombination and thus strongly promotes non-radiative pathways, effectively quenching the PL. State transition processes (c_2) encompass randomly occurring ionization and neutralization events that are presumed as the origin of PL intermittency with power-law interval times. The charge-ejection and neutrality-restoration mechanisms that initiate and conclude the blinking cycle, respectively, are still being discussed in literature. NP ionization is hypothesized to be either a result of direct quantum tunneling, thermo-ejection (both c_2 center) or Auger auto-ionization in case of an initial multi-excitonic state (c_2 left). The reverse process, namely neutralization, is assumed to be evoked by a similar set of mechanisms (c_2 right). [23,58] Because the excess charge-carrier is ejected from the NP or at least highly localized on the semiconductor surface, which results in a reduced wavefunction overlap, the surface chemistry strongly impacts the blinking of the individual nanostructures.

The PL dynamics (Figure 2.6b) of the "on" and "off" periods can be extracted by carefully selecting the aforementioned threshold intensity, ultimately resulting in the classification into either neutral or charged conformation of the single emitter. These gated groups have been found to exhibit radiative decay times at the order of $\tau_r \sim 10$ ns and non-radiative recombination on a much smaller timescale of $\tau_r \sim 10\text{--}100$ ps.^[59,60]

2.4.2 Spectral Characteristics

The PL properties of colloiddally synthesized NPs are not only subject to temporal intensity fluctuations, but also spectral inhomogeneities and hence, spectral broadening. As previously discussed in Section 2.2, the effective band gap is dependent on both the material composition and the size/geometry of the structure. The ensemble PL spectrum is consequently a convolution of the individual spectra of the single emitters present in the probed polydispers sample. However, spectral broadening also plays a significant role on the single particle level, with several broadening processes contributing to the shape of the emission, as is schematically illustrated in Figure 2.7. These mechanisms that broaden the "natural" spectrum (a) of an individual emitter include exciton–phonon coupling (b_1), spectral diffusion (b_2) and the exciton fine-structure (b_3).^[61]

Figure 2.7: Spectral broadening of colloidal NPs. The "natural" spectrum (a) of an individual emitter is subject to several homogeneous broadening mechanisms, namely exciton–phonon coupling (b_1), spectral diffusion (b_2) and the exciton fine-structure (b_3), which evoke the single-emitter spectrum (c). The inherently broad spectra that originate from the individual emitters convolve to an inhomogeneously broadened ensemble spectrum (d). Adapted from ref.^[61]



While the investigation of the resulting single-emitter spectra (c) on the individual particle level may circumvent the effect of polydispersity (blue, green and turquoise single-emitter spectra) that leads to the inhomogeneous broadening inherent to the ensemble spectrum (d), a reliable attribution of the spectral characteristics to the material composition and morphology remains challenging. Especially in the case of NWs, single-particle and single-emitter can not necessarily be treated synonymously, as several emission centers may be present along the one-dimensional structure. To gain a better insight into the characteristics inherent to the spectrum of an individual emitter, the involved broadening mechanism attributed to interactions of the exciton with the environment are discussed.

Exciton–Phonon Coupling

Phonon sidebands arising from electronic excitations coupling to different types of nuclear vibrations contribute to homogeneous spectral broadening. As the relaxation pathways and, consequently, recombination rates, are dependent on the magnitude of the exciton–phonon interaction and its apportionment between the various phonon types, the coupling mechanisms remain an active topic of research.^[62] Here, excitonic coupling to optical and acoustic modes is discriminated, with the former happening via Fröhlich interaction, whereas the latter are mediated via the deformation and the piezoelectric potential.^[63,64] The exciton–phonon coupling-strength is best construed using the dimensionless Huang–Rhys parameter, which describes the ratio between non-degenerate exciton-level (zero-phonon line) and the various satellite phonon-sidebands.^[65–67]

Spectral Diffusion

Migrating charges evoke fluctuating local electric fields, leading to random shifts of the emission wavelength, that originate from the Stark effect. At sufficiently low bin times and cryogenic temperatures, this diffusion of the PL signal was found to exhibit not only a meandering around a central emission energy, but also distinct energetic jumps of the jitter center.^[68,69] These discrete hops in particular were reported to originate from charge trapping in deep potential wells as opposed to a more diffusive motion of the charge through shallow potentials, which are uniformly distributed on the NP surface.^[70] Furthermore, the supposedly random charge migration was found to be governed by a memory effect that is associated with the relaxation to a stable surface-charge configuration.^[71] The complexity of the potential landscape formed by the crystal itself and the molecular ligands passivating the surface sites renders a multitude of surface compositions of different energy configurations.

Exciton Fine-Structure

Finally, the excitonic levels themselves are partitioned into several fine-structure states, which in turn incur phonon interactions.^[55] The splitting is caused by the crystal-structure dependent crystal-field splitting, the spin-related exchange interaction of the charge carriers and their Zeeman interaction.^[72] The morphology of the nanostructures causes degeneracies within the excitonic levels, which can be classified into so-called dark and bright states, which can be detrimental to an efficient recombination due to charge-carrier trapping in low-energy dark states.^[73,74]

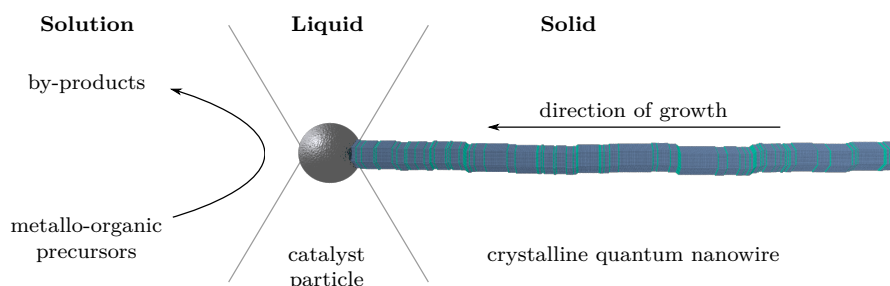
2.5 Colloidal Synthesis of Quantum Nanowires

Nanofabrication is generally actualized by either the top-down or the bottom-up approach. While the former is based on disintegration of the corresponding bulk material, the latter process is started from building blocks smaller than the aspired structure. In the first part of this section, the colloidal growth-mechanism is introduced, while the second part deals with different approaches to surface modification.

2.5.1 Solution–Liquid–Solid Method

A prominent example for the colloidal synthesis of one-dimensional nanostructures is the solution–liquid–solid (SLS) method, which was established in analogy to the vapor–liquid–solid (VLS) mechanism.^[14,75,76] During synthesis, the precursors introduced into the solution or vapor phase adsorb at the liquid-catalyst surface. The organic remnants are cleaved catalytically from the precursors before the semiconductor components dissolve into the low-melting metallic particle (liquid). Due to the limited solubility of at least one of the precursors in the catalyst droplet, supersaturation occurs, succeeded by crystallization from said particle (solid).^[77] As schematically shown in Figure 2.8, the semiconductor NW grows from the supersaturated particle at the liquid/solid interface.^[1]

Figure 2.8: Schematic of the SLS mechanism. The precursors present in the solution diffuse into the liquid catalyst particle. Crystallization is induced due to supersaturation.^[78]



The diameter of the crystallizing NW is mainly governed by the size of the catalyst nanoparticles. Consequently, the monodispersity of the metal NPs is essential for the synthesis of colloidal NWs having a narrow diameter distribution.^[79] The length of the resultant NWs is primarily constrained by the concentration of the respective precursors. Quenching of the reaction after a given time can be used as a means to influence the abundance of precursors and thus control the NW length. The wet-chemical synthesis is conducted at temperatures of 200–350 °C^[1], due to the limited temperature stability of the organic components such as coordinating solvent and aliphatic ligands. Thus, a suitable low-melting catalyst material has to be selected.

The phenomenon of melting-point depression is conducive to the variety of eligible materials as the phase-transition temperature is lowered significantly. Given the low melting point of nano-scaled bismuth particles (150 °C)^[80], the metal is well suited for the colloidal synthesis of cadmium chalcogenide NWs. However, pure Bi-NPs were found to exhibit deficient thermal size-stability, thus evoking broad size-distributions of the resultant NWs. Hence, polymer-stabilized Bi-NPs are commonly used to promote the monodispersity of the crystallizing NWs.^[77,81]

The morphology of the NWs is additionally preserved by coordinating surface ligands, which passivate the electron-poor metal surface-atoms and stabilize the nanostructures in unpolar solvents through their aliphatic chains. Typically, the anisotropic growth of colloidal nanostructures is influenced with these organic molecules through manipulation of the growth kinetics by altering the surface energy of a given facet.^[82–84]

While the one-dimensional geometry is determined by the nucleation at the liquid/solid interface during catalytic growth, the ligands indirectly influence the resulting structure by altering the reactivity of the precursor and thus, the thermolysis of the cadmium complex at the solution/liquid interface. This change in reaction kinetics has been reported to affect both NW diameter and crystal phase.^[79,85,86] Crystal-phase control in colloiddally grown NWs was recently achieved by manipulating the precursor-conversion chemistry through use of either the free *n*-tetradecylphosphonic acid (TDPA) or the deprotonated complexant, *n*-tetradecylphosphonate (TDPT). The protons provided by the free acid promote the chalcogenide-precursor cleavage, resulting in a near-stoichiometric ratio of Cd and Te dissolved in the Bi-NP, which was reported to cause polytypism. The anionic ligand species, however, binds more strongly to the metal cation than the often used di-*n*-octylphosphinate (DOPT), consequently reducing the precursor reactivity. The decrease in Cd:Te ratio facilitates solid catalyst particles that expedite the growth of mainly WZ NWs.^[22,87]

The controlled synthesis of phase-pure NWs is aspired, as crystal-structure alternations, which can be treated as planar defects similar to twinning boundaries and stacking faults, have a detrimental effect on the optical properties.^[19,20,88] In addition to their influence on the reaction kinetics, the ligands saturate the surface dangling-bonds. While the role of surface passivation and also the relation between the ligand binding-motif and shallow trap states has been thoroughly investigated,^[89,90] a systematic study on the influence of the ligand-chain length is still lacking.

2.5.2 Surface Modification

The luminescence of nanostructures has been found to be sensitive to surface ligation as well as geometry and size of the crystal.^[89] To design the luminescence characteristics and still maintain the beneficial effect of the original ligands during synthesis, a post-synthetic modification of the surface is required. The native capping molecules can be replaced with either organic or inorganic species in a ligand-exchange reaction (LER).^[89]

Specific functional groups can be utilized to tailor the bonds between the ligands and the surface atoms or to adapt the colloidal stability of the NCs in different solvents. Instead of large organic ligands even inorganic ions (e.g. S^{2-}) can be introduced for stabilization in polar media.^[15,16]

Recent advances in surface chemistry have shown, that the chemisorption of inorganic ligands can be utilized as a half-reaction in a sequential process called colloidal atomic layer deposition (c-ALD). In a second half-reaction a full layer of a binary compound can be completed. Using this self-limiting mechanism, epitaxial layers of the inorganic shell material can be deposited on the colloidal nanostructures.^[91–93]

Organic Ligand-Exchange Reaction

The NC–ligand interaction can be evaluated by adopting the concept of the covalent bond classification (CBC) that is commonly used for the description of organometallic complexes. The ligands are categorized as L-type (Lewis base), Z-type (Lewis acid) and X-type, corresponding to the number of electrons (2,-2,1) the neutral molecule contributes to the metal–organic bond.^[94–96] Consequently, L-, and Z-type ligands coordinate to surface cations and anions, respectively. The amphoteric X-type ligands, however, can interact with both, metal and non-metal surface-sites of binary nanostructures. While the charge-neutrality of the NC/ligand structure must be preserved, various ligand-exchange schemes including different binding motifs are possible. Ultimately, the LER is dependent on the acid–base equilibrium, the solubility of the free ligands and the binding-strength differences.^[97]

The ligand affinity for the NC surface may be estimated by applying the Pearson principle of hard and soft acids and bases (HSAB). It states that acids with a high charge-density and a low polarizability interact more strongly with bases exhibiting similar characteristics than with a partner with complementary properties. The dangling bonds of the positively charged surface cadmium are therefore more efficiently passivated by soft ligands.^[98,99]

Colloidal Atomic Layer Deposition

Atomic layer deposition is a technique that exploits the self-limiting nature of the sequential surface reactions during which the finite number of reactive sites is saturated by the precursor. After removal of the excess reactant, the complementary precursor is introduced. While the successive ionic layer adsorption reaction (SILAR) has already been employed as a binary reaction-sequence for colloidal core/shell synthesis, precise control of precursor concentration and reactivity remained challenging.^[100] However, an accurate determination of the total surface area is essential for high-quality epitaxial shell-growth and the avoidance of side nucleation. By exploiting the self-limiting character of the c-ALD method, which is based on purging of the unreacted molecules, the error-prone estimation of the core surface-area can be eluded.^[15]

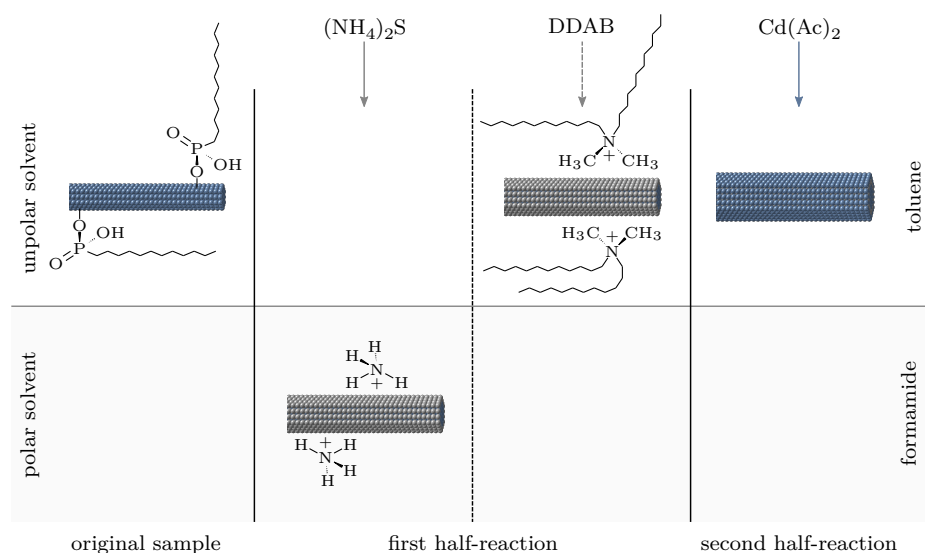


Figure 2.9: Reaction scheme of the colloidal atomic layer deposition technique. The original sample covered with native surfactants (e.g. PAs) is transferred from the unpolar (top) to the polar (bottom) phase by adding $(\text{NH}_4)_2\text{S}$. The first half-reaction is completed after the back-transfer of the S-terminated sample (gray) into the unpolar solvent using DDAB. The cycle is completed by depositing Cd (blue) on the NW surface during the second half-reaction.

The reactant removal is accomplished via a phase-transfer reaction between unpolar and polar solvents, as is exemplarily illustrated for the colloidal deposition of a CdS shell on the metal-rich surface of a NW in Figure 2.9. The native surfactants (e.g. phosphonic acids (PAs)) passivating the Cd-terminated core NWs are replaced with a nucleophilic chalcogenide monolayer (gray) that is electrostatically stabilized by the counterions (e.g. NH_4^+) in the polar formamide, while the original ligands remain in the unpolar toluene. The first half-reaction is completed by transferring the S-terminated NWs into fresh toluene using di-*n*-dodecyldimethylammonium bromide (DDAB). The c-ALD cycle is finalized with the second half-reaction that comprises the addition of the metal precursor (blue).^[15,91]

3 | Methods

In this chapter, the experimental background for the characterization of one-dimensional nanostructures is presented. The first sections provide details about confocal microscopy and supplementary spectroscopic methods used for analysis of the optical properties. The structural analysis of the colloiddally synthesized NWs is elucidated subsequently. Concluding, the calculation of exciton properties based on the effective-mass approximation is explicated.

3.1 Confocal Scanning Microscopy

Optical microscopy is a versatile method to characterize structure and geometry of a given sample. In a conventional wide-field setup, a large area of the sample is illuminated evenly and the light originating from the entire area is captured by a photosensitive detector. The resolution of such an imaging system is limited by the diffraction of light. The diffraction-intensity pattern of a radiating point source like fluorescent nanostructures results in a three-dimensional point-spread function (PSF).^[101] The Airy pattern represents said Gaussian intensity distribution projected onto the image plane. Arising from the circular aperture of a lens, this pattern comprises the bright central Airy disk surrounded by concentric interference rings.^[102] The Airy radius Δr_A describing the distance between the center spot and the first minimum is defined as

$$\Delta r_A = \frac{1.22}{2} \cdot \frac{\lambda}{n \cdot \sin(\alpha)} = 0.61 \cdot \frac{\lambda}{\text{NA}}, \quad (3.1)$$

where λ is the wavelength of light and the numerical aperture NA incorporates the refractive index n of the surrounding medium and the half angular aperture α . Two objects that are separated by Δr_A are imaged as a combined pattern with the first-order minimum of one coinciding with the principal maximum of the other, thus eliciting a discernible local minimum in the sum PSF. For two emitters of equal intensity, this amounts to the maximum lateral resolution of a diffraction-limited microscope as specified by the Rayleigh criterion.^[103,104]

In this conventional microscope a multitude of fluorescent objects in the wide sampled area contribute to the image, resulting in a significant background. To enhance the signal-to-noise ratio in a confocal setup, the excitation light is focused to a diffraction-limited spot on the sample. A pinhole is inserted in the plane optically conjugated to the illumination and the detector focus. Thus, light originating from outside of the illuminated sample volume is spatially filtered by the pinhole. As there are two confocal planes contributing to the instrument PSF, both the excitation and the detection PSF have to be considered. Due to the gaussian character of the resulting convoluted function, the full width at half maximum (FWHM) of the intensity distribution is reduced by a factor of $\sqrt{2}$ in comparison to the response of the conventional wide-field microscope. Hence, the lateral resolution^[105] of a confocal setup is given by

$$\Delta x_{\text{conf}} = 0.44 \cdot \frac{\lambda}{\text{NA}}. \quad (3.2)$$

However, the resolution of a confocal fluorescence microscope may differ from the theoretical expression stated in Equation 3.2 owing to the Stokes shift of the fluorescence. As the Airy radius depends on the wavelength of the light being diffracted, both the excitation and detection wavelengths have to be considered, when evaluating the resolution of a confocal setup.^[106]

The principle of a confocal configuration is schematically illustrated in Figure 3.1. The excitation light emitted by a laser is guided onto a beam splitter (BS), having a high transmittance. The deflected part advances into an objective and is focused onto the sample located in the object plane. The reflected excitation light and the fluorescence originating from nanostructures in the diffraction-limited spot are recollimated by the lens and directed through the beamsplitter onto the image plane. In the infinity space in which the beam is collimated, various optical elements can be inserted. A longpass filter is used to block the reflected excitation light from advancing towards the detector. A tubular lens focuses the fluorescence onto the point detector. Due to the small size of the photodiode used as detector, the redundant pinhole can be omitted. Light emanating from objects laterally or axially shifted from the illumination spot is imaged outside of the detection focus. Thus, the signal-to-noise ratio is enhanced and the resolution is improved. Consequently, only a small fraction of the sample is investigated at a time. To obtain an image of a larger area, either the sample or the microscope is raster scanned. This point-by-point detection allows for space-, energy- and time-resolved measurements.

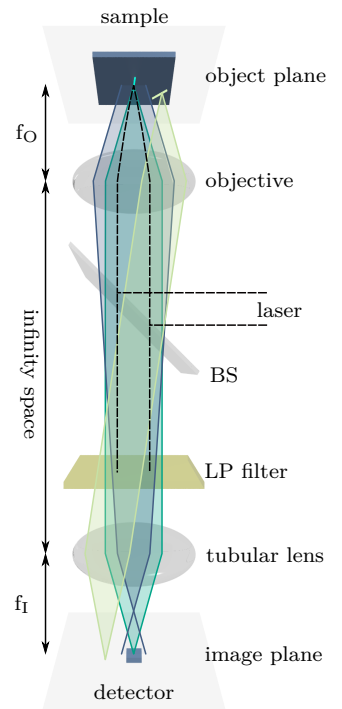
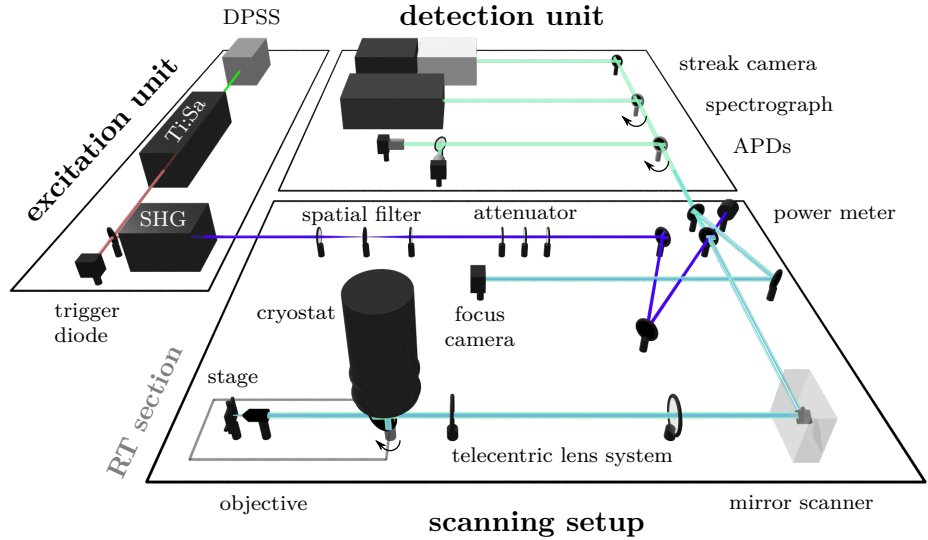


Figure 3.1: Schematic of a confocal setup. The excitation light (dashed line) is focused through the objective to a diffraction-limited spot on the sample. The reflected laser light is blocked by the longpass filter, while the light emitted from the nanostructure (turquoise) in the object plane advances to the detector. Light emanating from positions laterally (yellow) or axially (blue) shifted is not focused onto the detector positioned in the image plane.

The confocal setup that was primarily used for this thesis can be operated at low temperatures ($< 20\text{ K}$) or at room temperature (RT), is sketched in Figure 3.2 and the various components are presented in the following subsections. For the extensive optical characterization of semi-conducting nanostructures, the excitation unit has to satisfy multiple prerequisites. The wavelength of the light should allow for efficient generation of charge-carriers in the sample. Additionally, the time-resolved analysis requires pulsed excitation, ideally with a pulse repetition rate that can be adapted to the recombination kinetics of the material. Likewise, a suitable detection unit which enables the temporally and the spectrally resolved analysis has to be implemented. Finally, the scanning setup includes components for beam-shape and focus-position control.

Figure 3.2: Schematic of the low-temperature confocal setup. The laser beam is guided through several optical components onto the mirror scanner, which is used for position control of the in-plane focal spot on the sample. A mirror on a magnetic mount can be removed from the setup to switch from the LT setup to experiments at RT. Light emanating from the illuminated area advances to the detection unit.



3.1.1 Excitation Unit

For the excitation of semiconductor nanostructures various laser sources were utilized during the course of this thesis. Coherent light was generated either by different laser diodes, a white-light laser source combined with a tunable single-line filter or a sophisticated variable frequency mode-locked laser system.

The latter comprises a continuous-wave (CW) laser pumping a titanium-sapphire (Ti:Sa) laser and an optical parametric oscillator (OPO) or a second harmonic generator (SHG) for frequency conversion to the aspired wavelength regime. The 532 nm frequency-doubled diode-pumped solid-state (DPSS) pump laser consists of a neodymium-doped yttrium orthovanadate (Nd:YVO_4) crystal as gain medium emitting at 1064 nm and a lithium-triborate (LBO) crystal for second harmonic generation.

At high output powers of 8–10 W, the DPSS is exciting the titanium-doped sapphire ($\text{Ti}^{3+}:\text{Al}_2\text{O}_3$), which emits in a wavelength range of 680–1100 nm. Due to resonance conditions in the laser cavity, however, only certain lasing wavelengths can be amplified. The range of these longitudinal modes is further reduced by a birefringent filter (BRF). To switch from CW to mode-locked operation, the phase between the pulses revolving in the cavity is adjusted. The intensity of the concerted pulses is sufficiently high to exploit the Kerr-effect of the Ti:Sa crystal.^[30] The mode-locked light is focused more strongly than the CW component due to the intensity-dependent change of the refractive index in the saturable absorber material. Thus, the CW light can be removed from the cavity with a slit, while the mode-locked pulses revolve in the cavity without attenuation. Due to the length of the cavity, the system is operated with a repetition rate of 76 MHz.

To adapt the excitation light to the prerequisites of the sample, an SHG and a pulse picker can be implemented in the excitation unit. Finally, the timing of the pulses is monitored by a photodiode, which is utilized to trigger the detectors that allow for time-resolved measurements.

3.1.2 Confocal Scanning Setup

The excitation light, with applicable characteristics like wavelength and repetition rate, is guided into the confocal setup. A spatial filter unit is used to preclude aberrations in the laser output and form a collimated beam with a gaussian profile. For this, the distorted input beam is focused with a lens, resulting in the parallel fraction of the beam being refracted into a bright spot in the center surrounded by concentric rings caused by the non-parallel fraction. A circular aperture placed in the focal plane allows the primary component to pass. The off-axis irregularities in the beam are blocked by this pinhole. A second lens is used for recollimation to a smooth transverse intensity profile.

The optimized beam passes through an attenuator composed of a polarizing filter sandwiched between two birefringent retarders. The initial half-wave plate alters the polarization direction of the incident light. Via the rotational orientation of the half-wave plate with respect to the linear polarizer, intensity regulation is achieved. The final quarter-wave plate converts the polarization of the light from linear to circular, which is necessary to preclude polarization effects inherent to geometrically anisotropic samples.

A pellicle beamsplitter ($R/T = 4/96$) subsequently reflects 4% of the attenuated beam into a galvanic mirror scanner (OEM XY-Scanmodul, ARGES GMBH), while the other part is transmitted onto a power meter to monitor the excitation intensity. The mirror scanner, in combination with a telecentric lens system situated between the scanner and the objective, allows for point-by-point scanning of the sample by tilting of the installed mirrors and consequently altering the angle of entry of the beam into the objective. The lenses ensure that the beam passes through the objective irrespective of the scanner position. Scanning is actualized with a real-time computer-controlled measurement data acquisition system (ADwin gold, JÄGER MESSTECHNIK).

The setup can be used for measurements either at ambient conditions or at cryogenic temperatures under reduced pressure. A mirror can be inserted into the path of the beam behind the telecentric lens system to deflect the light into the cryostat. The objective (LMPLFLN, OLYMPUS, 100x, $NA=0.8$, $WD=3.4$ mm, $f=1.8$ mm) focuses the excitation light onto the sample, which is mounted beneath an inverted sample stage constituted of three stepping type piezoelectric motors used for horizontal positioning and vertical focus control, respectively. In the RT setup, sample positioning perpendicular and parallel to the beam is achieved via manual linear micro-translation stages. Because no prerequisites concerning vacuum and temperature stability have to be met in this configuration, the objective is readily interchangeable to adapt to the experimental demands.

In either configuration, the objective is used to recollect the light reflected and emitted by the sample. Having advanced through the telecentric lens system and the mirror scanner, a fraction of the light is reflected and focused onto a two-dimensional sensor. This camera is employed for focus control by imaging the retro-reflection of the light on the sample. The light transmitted through the beamsplitter is guided towards the detectors. Contingent on the type of measurement that is to be conducted, different filters can be inserted, namely neutral-density (ND) filters for wavelength-independent attenuation and shortpass (SP) or longpass (LP) filters to selectively remove part of the spectral components. Especially the LP filter plays a critical role as it blocks the reflected excitation light from the detection beam path.

3.1.3 Cryostat

The closed-cycle cryostat (attoDRY 700, ATTOCUBE SYSTEMS AG) itself is vacuum sealed for thermal insulation, and heat-radiation shielding is actualized through a copper shroud kept at 65 K. Stage and sample are conductively cooled to approximately 4 K through thermal contact to the helium expander chamber, the so-called coldhead. For precise temperature regulation, a heating pad is mounted in the cryostat. Although the objective is positioned in close proximity to the sample inside the cryostat as is illustrated in Figure 3.3, it is thermally coupled to the vacuum shroud to keep it at approximately room temperature.

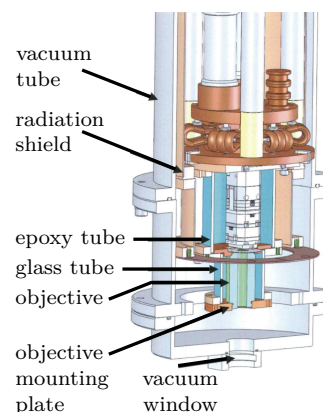


Figure 3.3: Schematic of the utilized closed-cycle cryostat. The sophisticated design comprising radiation shields and tubes ensures that the objective can be operated at RT within the vacuum chamber.^[107]

3.1.4 Detection Unit

For the characterization of the fluorescence emitted by the sample, various detectors can be utilized, depending on the information to be retrieved. Aspects of interest are the overall PL intensity, temporal and spectral properties and the correlation between the latter.

Two-dimensional images of a sample area are acquired by point-by-point scanning of the region of interest while simultaneously monitoring the PL intensity in each pixel with an avalanche photodiode (APD) (MICRO PHOTON DEVICES). These sensitive solid-state semiconducting photodetectors are working at high reverse bias voltages on the basis of the photoelectric effect. The charge carriers emitted through the photoelectric conversion of the incident photons are accelerated due to the externally applied electric field. At sufficiently high kinetic energies, an internal current gain is achieved through impact ionization within the detector material. As a result of this avalanche process the small single photon-initiated current can be amplified.

For time-correlated measurements, the APD is connected to a PicoHarp 300 TCSPC system (PDM series, PICOQUANT). This system registers the time of arrival of single photons emitted by the sample with respect to the excitation pulse. The time difference is ascertained via a time-to-amplitude converter (TAC), which ramps an electric signal upon detection of the trigger pulse. Repetition of this process results in a histogram of events over time, which corresponds to a fluorescence decay curve. By use of a second equivalent APD and a 50/50 beam splitter, photon-incidence correlation measurements can be performed to probe the nature of an emitter. Because the time elapsing between the detection of photons on one APD with respect to the second is investigated, these antibunching experiments can be conducted with both pulsed or CW excitation.

The spectral distribution of the PL is analyzed with a spectrograph combined with an adjacent charge-coupled device (CCD). A two-dimensional array of photoactive capacitors allows for the spatial distribution of the incoming photons to be recorded. In a depletion layer evoked by an applied bias, electron-hole pairs are generated through impact ionization. While the holes are moved towards the substrate due to the electric field, the electrons remain confined in the nearest potential well. Readout is actualized by the concept of a bucket brigade describing the pixel-by-pixel transport of the electrons accumulated in the various capacitors towards the output register. In a second cascade along the output register, the charge carriers are transferred to the amplifier and subsequently converted into a voltage that is proportional to the intensity of the light.

The correlation between fluorescence kinetics and spectral information can be determined by employing an additional beamsplitter between APD and CCD as to monitor both detectors synchronously. However, the various lifetimes being retrieved may not directly be attributed to different spectral features. To gain access to this type of interrelated information, the spectrally distributed output of the spectrograph can be guided through the device onto an APD. Especially to investigate the PL dynamics on very short time-scales a streak camera can be utilized to monitor the PL lifetimes versus spectral position.

The data acquisition system facilitates multiple measurement modes that are programmed in LabVIEW. Parameters such as scan area, number of pixels and integration time can be defined in the graphical user interface and the intensity information collected via the goldbox are visualized concurrently to the scanning procedure. The primary imaging mode can be combined with the output of a trigger signal per pixel to synchronize the time of detection with the advance of the focus. Thus, spectrally or temporally resolved data may be retrieved for all spatial coordinates.

Furthermore, the modular and accessible design of the optical setup can facily be extended. By implementing a second scanning device, excitation and detection focus on the sample can be effectively decoupled to probe the charge-diffusion length in the structure under test.

3.2 Structural Analysis of Nanostructures

To gain insight into the structural properties of quantum NWs such as geometry and crystallinity, a multitude of feasible methods is available. Information about NW diameter and crystal structure is important for the evaluation of the spectroscopic characteristics because both have an influence on the effective band gap of semiconductor nanostructures. Additionally, the presence of single NW on the substrate should be validated to preclude ensemble averaging effects. Since not only the structure of the inorganic NW itself, but also the organic ligand-shell, significantly affects the PL, analysis of the surfactants is needed.

3.2.1 Electron Microscopy

Higher resolving power can be accomplished by using a source of illumination with high energy. The wavelength of the accelerated electrons used as the illuminating beam in these microscopes is multiple magnitudes of order shorter than that of visible photons. Although these imaging systems have limited magnification due to diffraction, the actual resolving power is reduced by the aberration of the magnetic fields used for beam shaping in analogy to optical lenses in a conventional microscope. The essential components of electron microscopes (Figure 3.4) comprise the electron gun that accelerates the electrons towards the anode, electrostatic and electromagnetic lenses, detectors, the vacuum system and an electromagnetic shielding. Two main types of electron microscopes are commonly used to investigate nanoscopic structures: the transmission electron microscope (TEM) and the scanning electron microscope (SEM).^[108]

In **transmission electron microscopy**, a micrograph is retrieved from the interaction of the electrons and the sample they pass through. The resulting image depends on the acceleration voltage and the magnification of the system as well as on the atomic number and the thickness of the sample. To ensure that the accelerated electrons are transmitted through the sample, high acceleration voltages of 100 to 400 kV are used.^[109] For inorganic samples, such as semiconductor nanoparticles, voltages above 200 kV are typically applied. In imaging mode, electrons that are transmitted through the sample without any interaction, are registered to form a bright-field (BF) image, while the scattered electrons are blocked by an aperture inserted in the back focal plane. Likewise, a dark-field (DF) image can be obtained by detecting diffracted electrons at specific angles instead of the central beam.

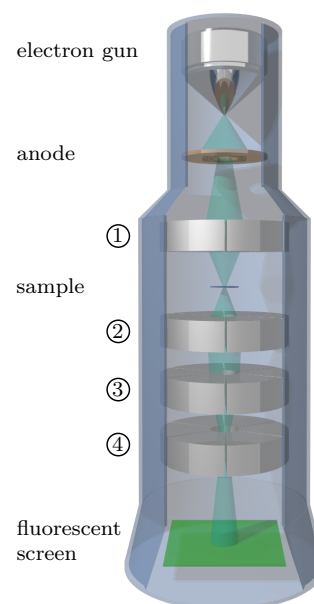


Figure 3.4: Layout of components in a TEM.

The electrons are accelerated from the gun towards the anode and are subsequently transmitted through the sample before being detected with a fluorescent screen. Shape control of the beam is actualized via magnetic lenses (circled numbers), namely ① condenser ② objective aperture ③ intermediate and ④ projector lens.

Contrast arises from elastic and inelastic scattering events. Some electrons are scattered elastically by the positively charged atomic cores of the sample, which alters the trajectory, thus removing them from the image plane. Inelastically scattered electrons may be precluded from detection due to their loss of kinetic energy. Changes in amplitude and phase of the electron waves upon scattering result in different contrast types. While most images contain both amplitude and phase contrast, the latter may be neglected at the lower magnifications typically used in a conventional TEM. The more prominent amplitude contrast can be subdivided into mass-thickness and diffraction contrast. Thick samples or elements having high atomic numbers cause large scattering angles, which result in dark regions in the micrograph as the scattered electrons are blocked by the objective aperture. In polycrystalline samples, diffraction contrast may be utilized to visualize crystallographic domains due to the specific orientation of the grain with respect to the incident beam.^[110]

To image not only grains but the position of the atoms within crystal lattice in detail, the phase contrast can be analyzed to compute a micrograph with atomic resolution as is done in high-resolution TEM (HRTEM). In this mode, contrast is generated through interference of the electron wave on the atom columns of the crystal. Although only the amplitude of the resulting interference pattern is detected, information about the crystal lattice is retrieved from the phase of the exit electron wave.^[111]

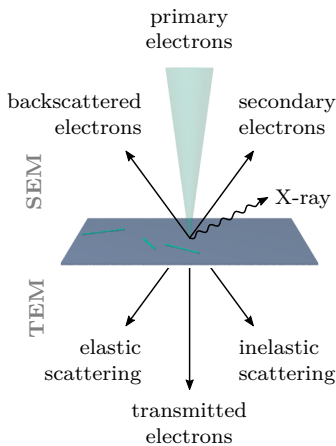


Figure 3.5: Electron-matter interaction in an EM. The primary electrons interact with matter (the sample) to scatter elastically or inelastically. These deflected electrons can be detected either downstream (TEM) or upstream (SEM) of the sample as BSE or SE.

In **scanning electron microscopy** an image is produced by raster scanning the focused electron beam over the surface of a sample. Comparably low acceleration voltages of 5 to 30 kV are applied as to reduce penetration depth.^[108] Similarly to the contrast formation in TEM, the image is obtained by detecting electrons originating from elastic and inelastic scattering events as is depicted in Figure 3.5. Instead of imaging the projected geometry of the specimen, the sample surface is visualized in an SEM with a large depth of field, which results in a three-dimensional appearance.

This is mainly due to the comparatively low energy of the secondary electrons (SE) and their short mean-free path in solids. This allows only electrons that are ejected from surface-near atoms by inelastic scattering interactions of the primary beam with the sample to be collected. Thus, the topology of the sample can be rendered. However, no in-depth information can be gained by monitoring the signal of the SE due to their small escape length. Instead, the composition of the sample can be mapped by detecting the backscattered electrons (BSE), since the strength of backscattering increases with the atomic number of the probed material.

Because of their high energy, the elastically scattered BSE can emerge from a larger interaction volume, which limits the resolution of the micrograph. Additionally, only relative differences in atomic mass of adjacent regions can be imaged, while an element-specific analysis is not possible via this material contrast. Identification of the elements present in the sample can be achieved by analyzing the characteristic X-rays that are emitted when an electron from the inner shell of an atom is removed by the electron beam and subsequently replaced by an electron from an outer shell. ^[112,113]

3.2.2 Atomic Force Microscopy

To circumvent the diffraction limit, an atomic force microscope (AFM) can be utilized. This imaging system is probing the surface of a sample on an atomic scale. The sample topology can be characterized due to attractive and repulsive forces between the sample and a mechanical profilometer that is raster scanned over the region of interest in close proximity to the surface. ^[114] The interactions between sample and probe result in deflection and torsion of the cantilever, which are monitored by a laser that is focused onto the back of the cantilever as is schematically shown in Figure 3.6. Variations in detection position of the reflected beam on the quadrant photodiode are used to reconstruct the topographic images. ^[115]

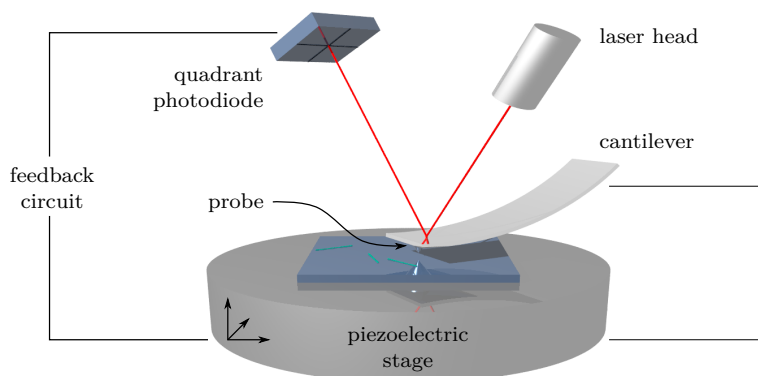


Figure 3.6: Schematic of an AFM. The deflection of the cantilever is monitored via a laser reflected onto a photodetector. A proportional-integral feedback-circuit is used for height adjustments of the cantilever.

To explain the working principle of an AFM in more detail, the nature of the interactions and their influence on the local potential have to be contemplated. The combination of long-range attractive and short-range repulsive forces can be visualized using the interatomic Lennard-Jones potential, which is illustrated in Figure 3.7. Attractive components like Van der Waals forces, that arise from electromagnetic-field fluctuations and that are independent of chemical composition, take effect over a distance of several nanometers. At much lower distances of below 1 nm, ionic and Pauli repulsion are the dominant forces. ^[116]

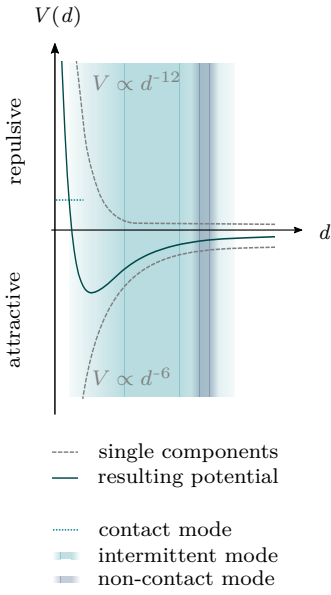


Figure 3.7: Lennard-Jones potential. Attractive and repulsive forces between sample and probe form a potential V , that is dominated by the former interaction at long distances d , while the latter is more significant at short ranges. The different imaging modes work in different regimes, resulting in varying probe-sample distances.

An AFM can be operated in three imaging modes, namely contact, intermittent and non-contact mode. Scanning in contact mode is conducted in the repulsive regime with the probe being in mechanical contact with the solid surface at a chosen force. In this static approach, changes in cantilever deflection are directly proportional to variations in topography. In intermittent (tapping) mode, the cantilever is driven to oscillate close to resonance. Being influenced by both the attractive and the repulsive components, the probe contacts the sample intermittently at the point of maximal deflection. The damped amplitude of the oscillation with respect to the driving signal is used as the main feedback parameter. Additionally, the phase of the cantilever oscillation can be monitored to obtain information about different materials present in the sample. For imaging in the dynamic non-contact mode, which is operated solely in the attractive regime, the drive-frequency is modulated to the resonance frequency of the cantilever. In this mode, the variation in resonance frequency due to long-range forces is utilized for feedback.

The intermittent mode is typically used to image semiconductor nanostructures. In comparison to contact mode, the mechanical contact between sample and probe is reduced, thereby circumventing the large lateral forces that may cause damage to both the sample and the probe. The force during periodic contact, may exceed the constant force used for the static measurements. For even more gentle conditions as are beneficial for soft surfaces, the non-contact mode can be utilized. However, these measurements are usually conducted in vacuum conditions, rendering the intermittent mode more convenient for NWs.^[117]

3.2.3 X-ray Diffraction

In addition to NW geometry, the crystal structure of the semiconductor is influential on the optical properties and should thus be analyzed. The regular array of atoms composing the crystal can be investigated by means of X-ray diffraction (XRD). The incident electromagnetic X-ray waves are scattered elastically by the electrons of the atoms forming the crystal. Consequently, spherical waves with the same frequency emanate from the scattering centers, which superpose to form an interference pattern. In case of a periodic arrangement of atoms and thus, electrons, the secondary waves interfere constructively if the condition described by Bragg's law^[118] in Equation 3.3 is satisfied:

$$n \cdot \lambda = 2 \cdot d \cdot \sin \theta. \quad n \in \mathbb{N} \quad (3.3)$$

Consequently, reflection spots arise only in specific locations in the diffraction pattern originating from a lattice with an interplanar distance d . For a comprehensive analysis of the crystal structure, either the wavelength λ or the angle of incidence θ have to be varied. This can be circumvented to some extent, if a powder, providing a statistical orientation of the sample, is used instead of a single-crystal. For anisotropic nanostructures however, the reflexes of some crystal directions may be hardly detectable in a conventional XRD-setup, as the orientation of the structures on the substrate is limited due to their geometry. The shape of the peaks in the resulting diffractogram is influenced by the size of the analyzed crystal as the FWHM declines with increasing number of lattice planes.^[119]

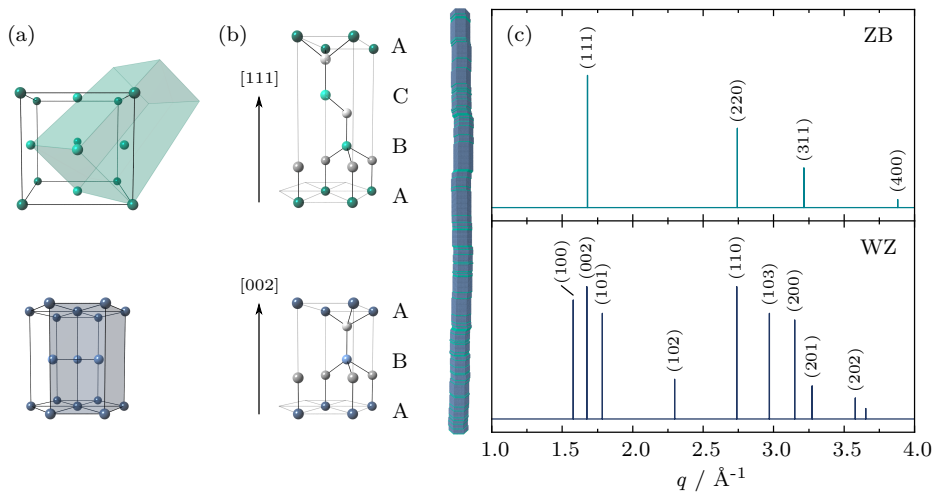


Figure 3.8: XRD data for CdTe. Representation of ZB (turquoise) and WZ (blue) crystal structure with (a) highlighted unit cells and (b) their crystallographic orientation in a CdTe NW. (c) The respective stick patterns of zb-CdTe (PDF-no.00-015-0770, top) and wz-CdTe (PDF-no.00-019-0193, bottom) are annotated with their Miller indices.

The NWs investigated during the course of this work consist of ZB and WZ segments. The orientation of the unit cells with respect to the long wire axis and the corresponding XRD stick-patterns are shown in Figure 3.8. A NW consists of only a limited number of lattice planes in most crystallographic directions, thus rendering the diffraction peaks broader than in a bulk crystal. Although this restriction does not apply to the fast-growth axis (z-axis), the shape of the peak is influenced by stacking faults and alternations in crystal structure. Thus, the NW comprises several small crystal grains, which are stacked together with a defined orientation. Careful analysis of the diffractograms can reveal the crystal phases present in the NW and give an estimate about their relative amount.^[88,120]

3.2.4 X-ray Fluorescence Spectroscopy

Another method exploiting the high energy of the X-ray photons is X-ray fluorescence (XRF) spectroscopy. With energies exceeding the binding energy of core-atomic levels, the X-ray photons excite the corresponding core-electrons, concurrently creating a vacancy. This unoccupied state is subsequently repopulated with an electron from a higher energy level, resulting in the emission of a secondary X-ray photon. This process is illustrated in Figure 3.9a for the transitions $K\alpha$ and $K\beta$. Contingent on the electronic configuration of the atoms in a material and the probe energy, a characteristic spectrum comprising the possible spectral lines is emitted as is exemplarily shown for CdTe (L-transitions) in Figure 3.9b. [121,122]

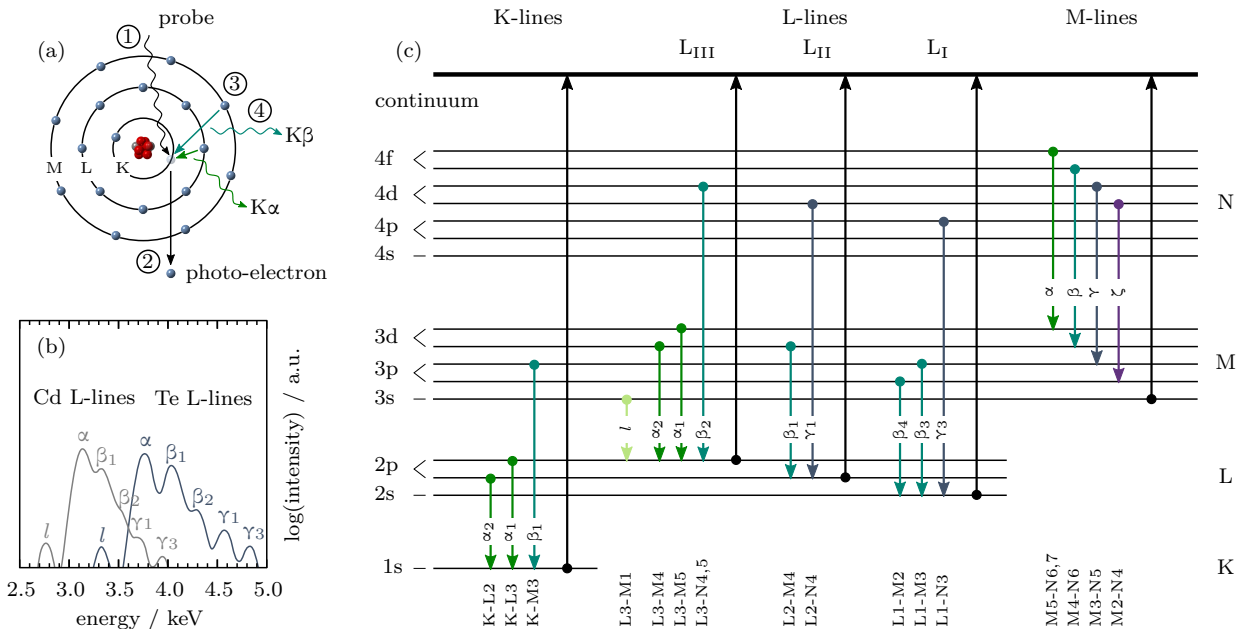


Figure 3.9: Principle of X-ray fluorescence. Schematic representation of the excitation of a core-electron (bold) by the incident X-ray photon. (a) The created vacancy (transparent) is repopulated with an electron from a higher shell resulting in the emission of XRF photons, which evoke characteristic XRF lines that are exemplarily shown as CdTe L-lines in gray (Cd) and blue (Te)(b). The major XRF lines (colored) and the absorption (black) are sketched to visualize their origins and elucidate both, Siegbahn and IUPAC nomenclature (c).

Depending on the origin of the photo-electron and the electron replacing it, the transitions are labeled according to the Siegbahn nomenclature using the letters K, L, M in combination with lower-case greek letters. The newer IUPAC notation uses a more systematic approach to label the involved orbitals unambiguously as depicted in Figure 3.9c. [122,123]. The prominent $L\alpha_1$ line (Siegbahn) for example, is denoted L3-M5 (IUPAC) in correspondence to the repopulation of a $2p_{3/2}$ hole with a $3d_{5/2}$ electron.

The strength of the XRF lines depends on the absorption coefficient and thus the excitation energy as well as on the transition probability. The individual XRF peaks that fingerprint the element i are centered around the transition energy E_i and can be described by the Gaussian function

$$g(E) = \frac{N_i}{\sigma_i \sqrt{2\pi}} \cdot \exp\left(-\frac{(E - E_i)^2}{2\sigma_i^2}\right), \quad (3.4)$$

comprising the standard deviation σ_i , the energy E and the number of counts N_i that relate to the integral of the function. While the transition energies are unique for each element and spectrally narrow, the various XRF peaks often overlap due to the broadening introduced by the detector, thus rendering quantification of the sample compounds intricate.^[122]

The XRF analysis may be further complicated by the elastic Rayleigh and the inelastic Compton scattering. While the peak originating from the former process is centered at the energy of the probe, the energetic position of the signal evoked by the latter is influenced by the geometry of the setup. In forward scattering configuration, the Compton peak is spectrally situated in proximity to the Rayleigh peak. However, this geometry is only suitable for X-ray transparent samples. In contrast, the smaller angle in the backward scattering configuration allows efficient collection of XRF photons, while the Compton peak is shifted towards lower energies closer to the XRF peaks attributed to the elements of interest. To minimize the spectral overlap between XRF and Compton peaks, a position of the detector in the sample plane at an angle of 90° with respect to the beam is aspired.^[124]

The often complex X-ray spectra are additionally affected by processes occurring in the detector rather than in the investigated sample. The primary XRF photons originating from the sample may evoke secondary XRF events within the detector-absorber material. The energy shift between the resulting escape peak and the primary XRF peak corresponds to the XRF transition energy of the absorber element. Other spurious peaks are caused by multiple photons impinging on the detector within the temporal resolution of the module. These pile-up peaks manifest at energies corresponding to the sum of the contributing XRF photon energies. In complex sample architectures, the XRF photons may be re-absorbed. Because the extent of this self-absorption is largely dependent on the sample thickness, the orientation of the sample with respect to the XRF detector is usually a critical parameter. However, this generally detrimental effect is negligible in case of the studied system due to the small diameter of the NWs.^[125]

3.2.5 Analysis of X-ray Beam Induced Current

X-ray based methodologies can be combined in a multi-modal approach to exploit the various light-matter interaction processes. The core-holes that have been created concurrently to the ejection of the photo-electrons during the initial excitation event are repopulated via Auger or XRF processes, which in turn generate vacancies in shallower levels. The resulting particle shower evokes a multitude of electron-hole pairs, which subsequently thermalize to the band edges of the semiconductor. Equivalent to optically excited electron-hole pairs, the X-ray generated charge-carriers can either recombine or contribute to an electrical current in an external circuit that is referred to as X-ray beam induced current (XBIC). The core levels and the band edges in a semiconductor are schematically illustrated in Figure 3.10, with typical energies for hard X-ray and optical transitions provided as annotations, respectively. Contrary to an absorption event just above the band gap, a single X-ray induced de-excitation cascade leads to multiple electron-hole pairs.^[126,127]

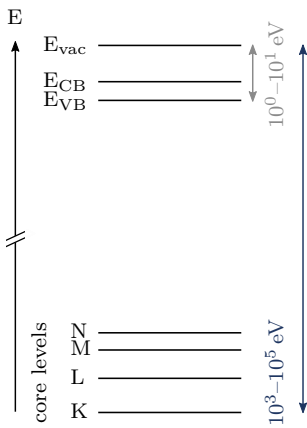


Figure 3.10: Energetic levels in a typical semiconductor. A single X-ray absorption event in the core levels causes a particle shower that generates multiple charge-carriers which thermalize to the band edges.

The XBIC signal is dependent on the local charge-collection efficiency and can consequently serve as a measure of the device performance. For the extraction of the small X-ray induced electrical signal, amplification and noise-separation procedures are applied by means of lock-in amplification. By demodulation of the electrical signal originating from the sample against a periodic reference signal, both direct current (DC, raw signal) and alternating current (AC, modulated signal) can be evaluated.^[128]

A multi-modal experimental setup comprising XRF and XBIC detection is illustrated in Figure 3.11, including a schematic of the principal signal paths (turquoise) required for the evaluation of the electrical response. The substrate with the lithographically contacted sample (Section 4.3.1) is attached and electrically connected to a printed circuit board (PCB) with sockets for a coaxial cable. The PCB in turn is mounted on a sample holder that is screwed to a kinematic base plate. The sample is probed by an intensity modulated X-ray beam (blue). The periodic modulation of the initially continuous synchrotron radiation is achieved by means of an optical chopper, which additionally provides the reference frequency as output signal. The amplitude of the raw electrical signal is matched to the range of the analog-to-digital converter of the lock-in amplifier (LIA) by means of a pre-amplifier (PrA). The PrA can additionally be utilized to apply a bias voltage to the sample. By splitting the pre-amplified raw signal, the DC signal can be ascertained without further analysis in the LIA, while the AC signal is retrieved via frequency mixing with the sinusoidal

reference signal and subsequent employment of a low-pass filter. Consequently, the modulated electrical signal induced by the periodic probe is isolated from contributions with other frequencies.

For data acquisition, voltage-to-frequency (V2F) converters are commonly utilized. However, the amplifier outputs are typically branched and recorded with two separate V2F devices to account for negative and positive contributions, respectively. To circumvent the splitting of the pre-amplified signal, the direct signal may also be retrieved by using an additional demodulator in the LIA without employing a low-pass filter, thus effectively accepting all frequency components.^[129]

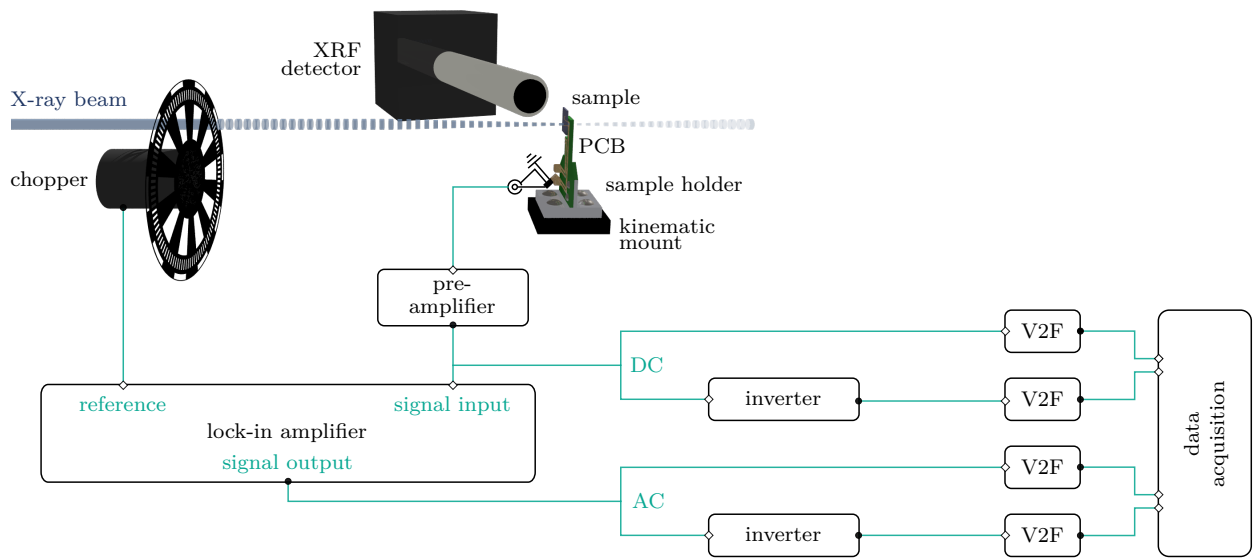


Figure 3.11: Principle of XBIC and XRF measurements. The incoming X-ray beam (blue) is modulated by the chopper. The X-ray fluorescence originating from the sample is collected by the fluorescence detector positioned close to the sample/beam interaction point. The electrical signal is pre-amplified and either fed into the lock-in amplifier and demodulated against the reference signal (chopper frequency) or directly passed to the data acquisition unit. Before being converted from a voltage to a frequency both DC and AC signal are split into two branches, one of which is inverted as to accept negative contributions. The signal path is illustrated according to ref.^[129]

The combination of XRF and XBIC analysis enables the spatial correlation of the elemental composition with the electrical performance of the nanostructure. While the resolution of the former might be enhanced by using the much smaller probe of an electron microscope at the cost of lower sensitivity, the latter is mainly influenced by the diffusion length of the charge-carriers, which often exceeds the spot-size by orders of magnitude. Additionally, the versatile X-ray setup can be readily upgraded to include further modalities such as XRD and X-ray excited optical luminescence (XEOL).^[130]

3.2.6 Thermogravimetric Analysis

The organic surfactants used for colloidal synthesis of NW are another component that is considered to influence the optical properties of semiconductor nanostructures. The thermal stability of the organic molecules can be investigated through thermogravimetric analysis (TGA). During these measurements, the weight of a sample is monitored while the temperature is varied over time. Both, physical and chemical phenomena that induce a change in weight may be ascertained. These processes include adsorption and desorption as well as chemisorption and thermal decomposition.

For the analysis, the previously dried substance is loaded into a heat-stable crucible (e. g. Al_2O_3), which is placed on a precision scale enclosed by a furnace. Conventionally, the temperature is increased with a constant rate, while sequential temperature ramps can also be programmed. To prevent the sample from oxidation, the TGA can be conducted under inert gas atmosphere. Instead of plotting the TGA curve, the corresponding first derivative (DTG curve) may be calculated for enhanced visualization of the deflection points, which render information about the thermal reaction.

If the measurement parameters are adequately chosen, a plateau of constant mass will have been reached at the end of the temperature ramp. This corresponds to the solid residue that is thermally stable under the experimental conditions. Provided that the geometry of the semiconductor nanostructure has been determined, the number of particles can be estimated. Thus, the surface saturation with the organic ligand that has been removed during the TGA may be calculated.

4 | Experimental Details

In this chapter, the synthesis procedures for the investigated nanostructures are described. The first section presents an overview of the wet-chemical synthesis of one-dimensional semiconductors, the second part elucidates surface-modification methods for these colloidal NPs. Consecutive sample-preparation steps are specified in the third section.

4.1 Synthesis

The fabrication of monodispers NWs in solution is dependent on various parameters. These include the high-boiling coordinating solvent as well as the different precursors and the metal-catalyst particles. The latter were prepared antecedent to the NW synthesis. The experimental parameters reported here reflect the standard procedure. Auxiliary, different additives were included to influence the morphology of the NWs during growth.

4.1.1 Synthesis of Metal-Catalyst Particles

The metallic bismuth NPs were synthesized following a protocol proposed by Wang and Buhro.^[77] A solution of dried octadec-1-en (ODE) and poly(1-hexadecene)_{0.67}-*co*-(1-vinylpyrrolidinone)_{0.33} (PHD-*co*-PVP) was prepared prior to use by Ann-Katrin Sassnau.

Under nitrogen atmosphere, 0.140 g (0.444 mmol) bismuth(III) chloride (BiCl₃) were dissolved in 1.1 mL tetrahydrofuran (THF) to form a milky suspension. While continuously stirring, 10 g of the 25 wt% PHD-*co*-PVP-ODE solution were injected at room temperature before adding 0.12 g lithium bis(trimethylsilyl)amide Li[N(SiMe₃)₂]. After the solution had turned red, the temperature was increased to 200 °C. The resulting dispersion was cooled to room temperature after 16.5 hours and 0.5 mL of the synthesis mixture were retrieved for isolation and purification, while the remainder was stored under inert conditions as a stock solution. To isolate the Bi-NPs, the aliquot was mixed with 1 mL of toluene and 4 mL of methanol and subsequently centrifuged at 24 400 *relative centrifugal forces* (RCF).

Purification was achieved by decanting the supernatant and redispersing the precipitate in the mixture of toluene and methanol (1:4, v:v). The suspension was sonicated for thorough mixing before centrifugation. The purification cycle was repeated twice and the isolated black Bi-NPs were stored in 3 mL of toluene under inert conditions.

4.1.2 Synthesis of Precursors

Cadmium Precursors

In a typical nanowire synthesis, a pre-synthesized cadmium complex having either di-*n*-octylphosphinic acid (DOPA) or *n*-tetradecylphosphonic acid (TDPA) as coordinating ligand was used as the cadmium precursor. These complexes were prepared using cadmium acetate dihydrate ($\text{Cd}(\text{ac})_2 \cdot 2\text{H}_2\text{O}$) following procedures established by Wang et al.^[22]

Cd(DOPT)₂ was prepared by dispersing $\text{Cd}(\text{ac})_2$ and double stoichiometric equivalents of DOPA in ODE. The flask was degassed and subsequently back-filled with nitrogen, repeatedly. After three cycles, the dispersion was degassed under reduced pressure for 30 min. The reaction gradually cleared while being heated to 150 °C under nitrogen atmosphere. After 30 min at temperature, a vacuum was progressively applied, resulting in the formation of a colorless precipitate. The suspension was stirred for 60 min and ensuingly cooled to RT. 30 mL of acetone were added and the precipitate was retrieved by centrifugation at 24 400 RCF and subsequent decantation of the supernatant. The precipitate was redispersed in fresh acetone, centrifuged and the supernatant decanted. This procedure was repeated three times, before the colorless crystalline powder was dried under reduced pressure.

Cd(TDPT)₂ was prepared accordingly. A dispersion of $\text{Cd}(\text{ac})_2$ and double stoichiometric equivalents of TDPA in ODE was degassed and subsequently back-filled with nitrogen for three cycles. The suspension grew gradually turbid during degassing for 60 min. The reaction was heated at 200 °C under nitrogen atmosphere for 30 min. A vacuum was progressively applied, after the suspension had cooled to 100 °C. The flask was back-filled with nitrogen and 30 mL acetone were added, resulting in a colorless precipitate. Through centrifugation at 24 400 RCF and subsequent decantation of the supernatant, the precipitate was retrieved. For purification, the precipitate was redispersed in fresh acetone and the procedure was repeated three times. A colorless crystalline powder was obtained through drying of the precipitate under reduced pressure.

Chalcogenide Precursors

For NW synthesis, tri-*n*-octylphosphine (TOP) chalcogenide stock solutions (0.025 M) were utilized. For the preparation of TOPE (E = Se, Te), 10 mL of the solvent were added to 0.25 mmol of the respective chalcogenide powder under nitrogen atmosphere at RT. The respective solutions were stirred for at least 24 hours prior to use.

4.1.3 Synthesis of Cadmium Chalcogenide NWs

In a typical synthesis of CdE (E = Se, Te) NWs 5.0 g tri-*n*-octylphosphine oxide (TOPO) and 35 mg (50 μ mol) Cd(DOPT)₂ were heated to 100 °C under nitrogen conditions. The mixture cleared as both TOPO and the cadmium precursor melted. The solution was mixed for one hour under reduced pressure at 100 °C, as to remove excessive water. Subsequently, the solution was heated to 250 °C under nitrogen atmosphere and one-third stoichiometric amounts of the chalcogenide-precursor solution (0.025 M) premixed with 20 μ L of the Bi-NPs suspension were injected. The reaction was kept at temperature for three minutes and ensuingly cooled to RT by removing the heating mantle. At 100 °C, 10 mL of toluene were added to the suspension.

The isolation and purification procedure comprises centrifugation at 24 400 RCF and subsequent decantation of the supernatant under inert conditions. The precipitate was redispersed in 10 mL of toluene before sonification for thorough mixing. The purification cycle was repeated three times and the resulting stock solution was stored in nitrogen atmosphere. This standard procedure was applied for the synthesis of both CdTe and CdSe NWs. Optionally, di-*n*-octylphosphine (DOP) was injected together with the TOPE solution.

The CdS NWs however, were mainly synthesized by Ann-Katrin Sassnau following a different protocol. For a standard synthesis, 32 mg (0.25 mmol) CdO, the desired phosphonic acid (PA) and 5 g TOPO were heated to 350 °C under nitrogen atmosphere. The mixture was continuously stirred at temperature until the solution had cleared. The reaction was degassed at 110 °C under reduced pressure for one hour, subsequently back-filled with nitrogen and heated to 300 °C. After the temperature had stabilized, the premixed sulfide-precursor solution consisting of TOPS (2 M), Bi-NPs and 500 μ L TOP was injected. The reaction was quenched after three minutes and cooled to RT by removing the heat source. 10 mL of toluene were added to the dispersion at 100 °C. The CdS NWs were retrieved and purified as described before but under ambient conditions.

4.2 Surface Modification

Surface passivation is a critical parameter for the growth kinetics during synthesis as well as for the resulting optoelectronic properties. Therefore, different approaches to the modification of the semiconductor surface have been chosen. The original organic surfactants have been replaced by either different organic molecules or by inorganic layers. Additionally, the surfactants have been stripped from the NWs using TGA setup.

4.2.1 Ligand Removal via Thermogravimetric Analysis

The post-synthetic heat treatment was conducted in a conventional TGA (TGA 209 F1 Iris, NETSCH-GERÄTEBAU GMBH) instrument. A fraction of the stock solution was purified and diluted with toluene under nitrogen atmosphere. 3 μ L of the suspension were transferred onto a Si/SiO₂ substrate. The wafer was placed in an aluminum crucible and the ensemble was heated to 600 °C at a rate of 20 K/min under a flow of protective gases (N₂). The thermal stability of inorganic/organic core/shell system was investigated using an established TGA procedure. The purified NW suspension was centrifuged and the precipitate was dried under reduced pressure. The resulting powder-like sample was filled into a ceramic Al₂O₃ crucible and heated to 600 °C at a rate of 10 K/min under protective nitrogen flow. The thermal response of the organic surfactants DOPA and TOPO was analyzed using the same protocol. Prior to the measurements, a corresponding thermogravigram of the empty crucible was recorded.

4.2.2 Organic Ligand-Exchange Reaction

The DOPT-capped CdTe NWs were subjected to a ligand-exchange reaction to replace the initial long-chained surfactants with pyridine following a protocol established for cadmium-based NCs.^[131] In preparation of the surface treatment, 1.5 mL of the CdTe NW stock solution were purified under inert conditions. The sample was centrifuged at 24 400 RCF and the supernatant subsequently decanted. The precipitate was redispersed in 5 mL of toluene by sonification. The purification cycle was completed twice. For the LER, the purified NWs were redispersed in 10 mL of pyridine following a third centrifugation step. The reaction mixture was heated to 65 °C while stirring continuously. After 3 h at temperature, the dispersion was stirred for 12 h at RT. The pyridine-capped CdTe NWs were retrieved by centrifugation and decantation. The precipitated CdTe/Pyr NWs were redispersed in 1.5 mL toluene for storing.

4.2.3 Colloidal Atomic Layer Deposition

The synthesis of core/shell NWs utilizing the c-ALD procedure was carried out by Sara Grunewald following a protocol proposed by Ithurria and Talapin.^[15] In preparation of the first c-ALD cycle, 200 μL of a CdSe NW sample stored in toluene were added to 1 mL toluene and 1 mL formamide (FA) in a 4 mL vial. For the first half-reaction, the NWs were transferred from the nonpolar phase into the polar phase by adding 4 μL of an aqueous solution of diammonium sulfide ($(\text{NH}_4)_2\text{S}$, 40–44%) and continuous stirring at 900 rpm for 5 min at RT. To verify the completion of the phase transfer, the clearing of the previously blackish upper toluene phase to a colorless solution and the concurring clouding of the lower FA phase were monitored. The polar dispersion was rinsed twice with toluene and the nonpolar phase subsequently discarded and replaced by 1 mL of fresh solvent. The NWs were transferred back to toluene by adding 45 μL of didodecyldimethylammonium bromide (DDAB, 0.1 M) in toluene and 90 μL of tetraethylammonium bromide (Et_4NBr , 0.1 M) in FA while stirring for 5 min. After the successful phase transfer indicated by the clouding of the toluene phase, the clear polar phase was discarded and the mixture rinsed twice with fresh FA. For the second half-reaction, 1 μL FA and 60 μL of $\text{Cd}(\text{ac})_2 \cdot 2\text{H}_2\text{O}$ (0.1 M) dissolved in FA were added. The reaction was stirred for 5 min at RT before the still colorless polar phase was discarded. The unpolar dispersion was rinsed twice with fresh FA and the c-ALD cycle was completed by adding 1 mL of the polar solvent to re-establish the two immiscible phases.

4.3 Procedures

4.3.1 Sample Preparation and Device Fabrication

The NWs were stored in a highly concentrated stock solution. For measurements on substrates, such as TEM and PL spectroscopy, a fraction of the stock solution was diluted with toluene. To reduce the size of NW bundles, the dispersion was ultrasonicated for 1 min prior to deposition. Depending on the characterization method to be applied, 3 μL of the sample were dropcast either onto a grid membrane or a Si/SiO₂ substrate. To minimize sample degradation, the NW deposition was usually conducted in a glovebox and the sample was transported and stored in a vial filled with nitrogen before being mounted in the experimental setup.

For electrical measurements, single NWs were electrically contacted using platinum as contact metal. In preparation, the Si/SiO₂ substrates were pre-patterned with macroscopic gold contact-pads and conductive-paths as well as platinum markers using optical and electron-beam lift-off lithography (EBL), respectively. The macroscopic structures consisting of a 5 nm titanium adhesion layer and a 35 nm gold layer were fabricated using the positive photoresist (AZ ECI 3012) and a metal ion free developer (AZ MF 726). For patterned exposure with a UV-lamp (366 nm), a photomask was utilized. The microscopic markers consisting of a 20 nm platinum layer were transferred using a two-layer positive e-beam photoresist system (AR-P 631-679 series) and the high-resolution developer (AR 600-55). This 50K/950K double layer was irradiated according to a pre-defined pattern, using an SEM (Quanta 3D FEG, FEI, 7 keV, 360 μA). The respective metal films were transferred using physical vapor deposition (PECS-682, GATAN). The lithographic procedures were concluded using acetone as stripping agent.

The subsequently deposited NWs were analyzed using AFM and their position and orientation registered relative to the pre-deposited markers. Contacting of the NWs with platinum leads was finalized using individual masks for the EBL procedure described above. The device was mounted on a PCB and electrical contact was established via wire bonding (Bonder 5310/5330, FEK DELVOTEC) between the gold contact pads on the substrate and the electrodes of the PCB. The lithography process was conducted by Nicklas Giese. The nanolithography masks were designed using the vector graphics editor Inkscape and the KLayout Editor to illustrate the position of the NW and transfer the sketch into the software ELHPI *Quantum* for the final layout of the electrodes.

4.3.2 Structural Analysis

X-ray Diffraction

For XRD analysis, a fraction of the stock solution was concentrated via centrifugation and the resulting precipitate was transferred into a glass capillary ($\varnothing = 0.1$ mm, $d = 0.01$ mm). The powder XRD measurements were performed by Philip Harder, using a microfocus laboratory X-ray source (I μ S, INCOATEC, 50 kV, 1000 μ A) equipped with a Cu emitter. For operation in transmission geometry, a 2D-detector (MAR300, MARXPERTS) was positioned downstream of the sample. A CeO₂ standard was used for calibration and background correction was performed by measuring an empty capillary. Orientation effects of the NWs were significantly reduced by using capillaries instead of substrates and by exploiting the Debye–Scherrer configuration.

Nuclear Magnetic Resonance

The proton nuclear magnetic resonance (¹H-NMR) measurements were performed by Thomas Hackl using a 600 MHz NMR spectrometer (Avance III HD 600, BRUKER). In preparation of the analysis, a fraction of the stock solution as well as the ligand-exchanged NW suspensions were diluted with toluene before centrifugation. The precipitates were subsequently redispersed in toluene. Having repeated the purification cycle three times to remove excess ligand-molecules, the procedure was concluded by redispersing the NWs in toluene-d₈. To promote the homogeneity of the respective NW suspensions during the measurement, the NMR tubes were placed in an ultrasonic bath just before the investigation.

Infrared Spectroscopy

The molecular vibrations were analyzed using an infrared (IR) spectrometer (FT-IR Vertex 70, BRUKER) in transmission geometry. Both the original and the ligand-exchanged NWs were concentrated via centrifugation under nitrogen atmosphere and the precipitates were dried under reduced pressure. The resulting powder-like NW samples were mixed with KBr salt to form pellets for the IR-characterization, which was performed by Ute Gralla. The background was retrieved by measuring a pure KBr pellet.

Electron Microscopy

Geometry and morphology of the colloiddally synthesized NWs were analyzed via transmission electron microscopy. Carbon film coated copper grids or 40 nm SiO₂ membranes were used as transparent substrates. The latter are arranged on a 200 nm Si₃N₄ grid structure suspended in a regular TEM disk, that is mountable in various instruments for correlative investigations. Overview micrographs were obtained with a compact high-performance TEM (JEM-1011, JEOL) operated by Ann-Katrin Sassnau and Andreas Nielsen. Detailed images on the single-particle level for crystal-structure analysis were collected by Andreas Kornowski with a HRTEM (JEM-2100 F, JEOL).

The nanolithography scribing procedure was conducted by Andreas Kolditz using a field-emission SEM (Quanta 3D FEG, FEI). The same instrument was utilized by Charlotte Ruhmlieb to image the contacted CdTe NW sample.

Scanning X-ray Microscopy

Hard X-ray synchrotron radiation was used for scanning X-ray microscopy including XRF and XBIC measurements. The nanoimaging experiment was performed at the nanoprobe beamline 26-ID-C of the Advanced Photon Source (APS) at Argonne National Laboratory.^[132] The incident X-ray beam with a photon energy of 8.4 keV and a photon flux of $4.2 \cdot 10^8$ ph/s was focused to a FWHM spot size of 30 nm \times 30 nm by a Fresnel zone plate. The sample was positioned at a nominal angle of 75° relative to the probe in a vacuum chamber.

An in-depth investigation of the heavy metal particles was conducted in the micro hutch of beamline P06 of PETRA III at DESY (Deutsches Elektronen-Synchrotron)^[133] at a beam energy of 18 keV (above the Bi_{L1}-edge) and a photon flux of $4.7 \cdot 10^8$ ph/s. The FWHM of the horizontal (h) and vertical (v) focus, achieved with a set of Kirkpatrick–Baez (KB) mirrors, was determined to be 395 nm \times 215 nm. The sample was positioned perpendicular to the incoming beam at ambient conditions.

The **electrical** measurements were performed at 26-ID-C utilizing an ultra-high frequency lock-in amplifier (UHFLI, ZURICH INSTRUMENTS) in combination with a current pre-amplifier (SR570, STANFORD RESEARCH SYSTEMS) operated in low-noise mode with an amplification factor of 5 pA/V. The XBIC signal was demodulated against the chopping frequency of 7.3 Hz, using a time constant of 0.137 s.

Table 4.1: Parameters of the hard X-ray beamlines used for X-ray microscopy.

APS – 26-ID-C	
Energy	8.4 keV
Flux	$4.2 \cdot 10^8$ ph/s
Spot size (h)	30 nm
Spot size (v)	30 nm
Atmosphere	vacuum
PETRA III – P06	
Energy	18.0 keV
Flux	$4.7 \cdot 10^8$ ph/s
Spot size (h)	395 nm
Spot size (v)	215 nm
Atmosphere	ambient

For **fluorescence** measurements, a single-element silicon drift detector (Vortex EM, HITACHI HIGH-TECH SCIENCE CORPORATION) in combination with a digital pulse processor (Xspress3, QUANTUM DETECTORS) was used at P06, whereas a four-element silicon drift detector (Vortex-ME4, HITACHI HIGH-TECH SCIENCE CORPORATION), read out with a multi-channel digital pulse processor (xMAP, XIA), was used at 26-ID-C. At both facilities, the energy dispersive detectors were positioned inboard of the sample at an average angle of 90° relative to the probe.

Large-area nano-XRF/XBIC scans (26-ID-C) ($2\ \mu\text{m} \times 14\ \mu\text{m}$) covering the complete CdTe NW, including the metal contacts, were performed using the hybrid motors that raster scan the zone-plate focus across the sample.^[132] With a bin time of 0.7 s and a probe modulation with a duty cycle of 50%, an effective dwell time of 0.35 s was achieved. With these experimental settings, a high-resolution scan ($50\ \text{nm} \times 50\ \text{nm}$ step size) and a series of scans ($280\ \text{nm} \times 50\ \text{nm}$ step size) with varying bias voltages were obtained.

The μ -XRF scans (P06) that detail on the elemental distribution in distinct regions of interest ($1\ \mu\text{m} \times 2\ \mu\text{m}$, $25\ \text{nm} \times 25\ \text{nm}$ step size) throughout the device were sampled with a dwell time of 1.0 s without X-ray beam modulation. The respective data sets were corrected for photon flux variations as monitored with the upstream ion chamber as well as for potential deviations in dwell time.

The evaluation of the XRF spectra was conducted using XRF analysis-tools that have been developed at different synchrotron facilities, namely MAPS (APS) and PyMca (European Synchrotron Radiation Facility). For the preliminary visualization of the scans at beamline 26-ID-C, the established tool MAPS was used. The complementary μ -XRF spectra that were obtained at P06 using a higher beam energy were fitted by Christina Ossig using the conventional program PyMca. However, these tools are deficient for the analysis of trace elements and fitting of individual peaks. Thus, a custom XRF-fitting code written by Catharina Ziska was applied to the nano-XRF data.^[134] This script allowed for the independent parametrization of the XRF peaks originating from individual transitions.

The measurements were conducted in collaboration with Michael Stückelberger with support of Christian Strelow (at APS) and Giovanni Fevola (at PETRA III) with assistance from local beamline staff.

4.3.3 Chemicals

The substances that were used during the course of this thesis are listed in Table 4.2 including acronyms, chemical purity and supplier.

Table 4.2: Details of the utilized chemicals.

Substance		Purity in %	Supplier
Name	Acronym		
Diammonium sulfide	-	40–44 w% H ₂ O	Alfa Aesar
Acetone	-	99.8	VWR Chemicals
Bismuth(III) chloride	BiCl ₃	100	ABCR
Bismuth nanoparticles	Bi–NPs	-	(1)
1-Bromoheptane	-	99	Sigma Aldrich
Cadmium acetate	Cd(ac) ₂	99.99	Sigma Aldrich
Cadmium oxide	CdO	99.99	Chempur
1-Chloroheptane	-	99	Sigma Aldrich
Didodecyldimethylammonium bromide	DDAB	98	Sigma Aldrich
Di- <i>n</i> -octylphosphine	DOP	-	(2)
Di- <i>n</i> -octylphosphine oxide	DOPO	-	(2)
Di- <i>n</i> -octylphosphinic acid	DOPA	-	(2)
Formamide	FA	99.0	Sigma Aldrich
Hexane	-	97	Acros Organics
1-Iodoheptane	-	98	Sigma Aldrich
Lithium bis(trimethylsilyl)amide	Li[N(SiMe ₃) ₂]	-	ABCR
Methanol	-	99.8	Acros Organics
Octadec-1-ene	ODE	92	Merck
Octadecylphosphonic acid	ODPA	99	PCI Synthesis
Octanoic acid	-	99.5	Acros Organics
Octylphosphonic acid	OPA	99	ABCR
Poly(1-vinylpyrrolidon)- <i>graft</i> -(1-hexadecen)	PHD- <i>co</i> -PVP	-	Ashland
Propan-2-ol	-	99.7	VWR Chemicals
Pyridine	Pyr	100	Merck
Selenium	Se	99.5	Acros
Sulfur	S	99.99	Sigma Aldrich
<i>n</i> -Tetradecyl- phosphonic acid	TDPA	97	ABCR
Tellurium	Te	99.99	Sigma Aldrich
Tetraethylammonium bromide	Et ₄ NBr	99	Sigma Aldrich
Tetrahydrofuran	THF	99.5	Acros Organics
Tri- <i>n</i> -octylphospine	TOP	97	ABCR
Tri- <i>n</i> -octylphosphine oxide	TOPO	99	Sigma Aldrich
Toluene	-	99.85	Acros Organics

(1) The substance was prepared by Ann-Katrin Sassnau

(2) The substance was prepared by Andreas Nielsen

5 | Results and Discussion

In this chapter, the experimental findings will be evaluated and contextualized to concepts established in literature, which were introduced in the previous chapters. Within this project, a variety of one-dimensional cadmium chalcogenide heterostructures has been investigated. The discussion is thus divided into several sections pertaining to the different sample systems and their respective characteristics being analyzed.

First, the spectroscopic properties of organic-ligand covered CdTe NWs are highlighted. Due to their polytypism, these wires present as a special case of longitudinal heterostructures, which is assumed to affect charge-carrier localization. Second, the influence of the ligand system that forms an organic shell and may be presumed to establish a radial heterostructure, is discussed on the basis of different post-synthetic ligand alteration-processes. More specifically, complete ligand-stripping as well as different ligand-exchange reactions have been conducted, with the latter including both, organic and inorganic substituent surfactants. Third, the expedience of different ligands utilized *ab-initio* during synthesis of cadmium chalcogenide NWs as opposed to the postsynthetic treatment is deliberated with respect to the spectral properties and the morphology of the nanostructures. Finally, the electrical response of SLS-grown QNWs is correlated to their elemental distribution to retrieve the structure-property relationship using X-ray microscopy in the last section.

5.1 Photolumuminescence of CdTe QNWs

The intriguing combination of the potentially unhindered electron mobility in longitudinal direction and the confinement effects in radial direction in one-dimensional nanostructures poses an interesting case-study for exploring the electronic and optical properties of said quantum structures with respect to their structural composition.

A previous study on SLS-grown CdSe QNWs has disclosed the blinking behavior and the origins of spectral features observed at cryogenic temperatures.^[19] These low-temperature spectra of individual CdSe QNWs presented with two distinct groups of peaks, which were labeled near-band-edge (NBE) and trap (T) emission. Both emission groups exhibit temporal intermittency and slight energetic shifts that fluctuate individually and on different time scales without any obvious correlation. As origin of these emission bands, the polytypism-induced type-II potential landscape along the CdSe-QNW axis was considered. Self-consistent calculations of the charge-carrier localization in the QNWs affirm that the lengths of WZ and ZB segments in CdSe QNWs are insufficient as to evoke an effective axial confinement. For the observed NBE–T spacing, much longer segments are required, which typically do not occur in these SLS-grown QNWs, due to the near-equivalent nucleation energies of WZ and ZB modification.^[19,135]

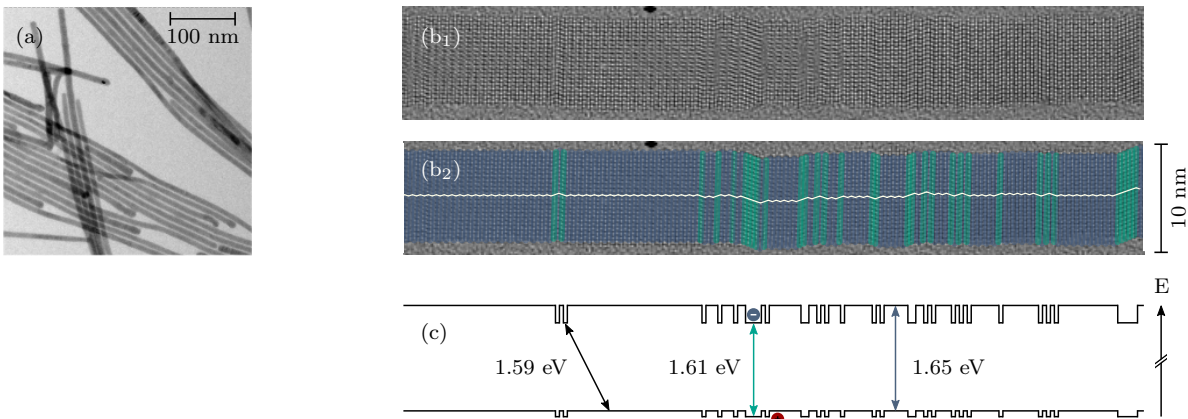


Figure 5.1: Electron Micrographs and band alignment of CdTe QNWs. Conventional TEM image of an ensemble of CdTe QNWs (a) and a high-resolution micrograph of an individual CdTe QNW from the same batch without (b₁) and with (b₂) highlights for WZ (blue) and ZB (turquoise) segments. The white line serves as a guide to the eye and further emphasizes the ABA ("zigzag") and ABC ("zigzig") sequence of the respective crystal phase. The theoretical band alignment (c) corresponding to the pictured QNW segment is sketched, representing the quasi-type-II heterostructure along the wire axis.^[36]

Control over crystal structure during colloidal synthesis has been found to be complicated, due to the extensive number of parameters and their interdependence in this solution-based approach. Especially reaction temperature, ligation and the high-boiling solvent are susceptible criterions that have been demonstrated as means to synthesize near-phase-pure CdTe QNWs. As the solvent TOPO does not only provide a reaction medium, but can also act as surfactant, it is of particular interest. Having found several contaminants, detrimental or beneficial towards the synthesis, Wang et al. identified DOP as one of the impurities that can promote phase-purity in CdTe QNWs.^[77,136] The choice of Cd-precursor further contributes to the final phase-alternation frequency. A mix of TDPA- and DOPA-complexated cadmium was reported to enhance the WZ amount.^[22]

These carefully concerted parameters for the SLS-growth of cadmium chalcogenide QNWs were found to have the biggest effect when synthesizing CdTe QNWs, possibly due to a more suitable combination of nucleation barriers than for the other CdE QNWs. Thus, this sample system was used to further investigate the influence of polytypism on the optical properties on the single-particle level. The phase-alternations of an SLS-grown CdTe-QNW sample with a heightened WZ/ZB ratio are analyzed in Figure 5.1. The TEM image in (a) reveals an ensemble of mainly straight wires exhibiting a mean diameter of 8.3 nm. The corresponding HRTEM micrograph of an individual QNW in Figure 5.1b does indeed reveal the presence of both, WZ and ZB segments. For ease of perceptibility, the WZ and ZB lattice planes have been color-coded in blue and turquoise respectively. A lattice plane was categorized into the WZ crystal phase, when an ABA ("zigzag") stacking order was observed, while the ZB crystal phase was assumed for an ABC ("zigzig") sequence.

The band gaps of CdTe in WZ and ZB modification were reported to amount to 1.654 eV and 1.607 eV, respectively. Taking into account the conduction band offset of 0.065 eV, a type-II sequence of individual quantum wells arises as is depicted in Figure 5.1c. The prevalence of the WZ conformation can be verified on the basis of Figure 5.1b. Further, the remaining ZB segments only extend up to a few ML (≤ 5) at a time, rather forming stacking faults than larger intervals and thus, sufficiently large potential wells. While near phase-purity was reported in the literature, no higher WZ/ZB ratios or a more suitable distribution of the ZB fraction within longer segments was achieved using the traditional SLS-routine.

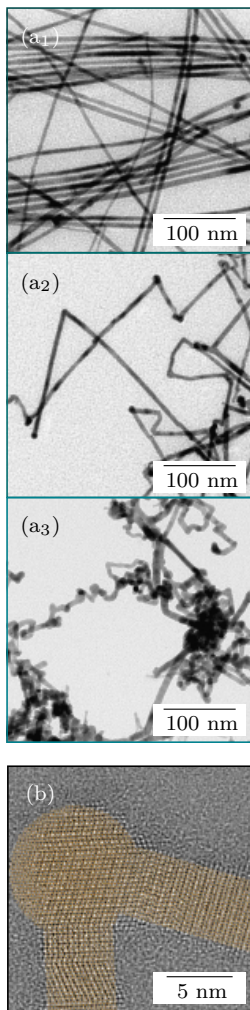


Figure 5.2: TEM images of CdTe QNWs synthesized with halogenated alkanes as additives. During synthesis, different mole equivalents of 1-bromoheptane were injected, namely (a₁) 0.5, (a₂) 1.0 and (a₃) 1.5. The HRTEM micrograph overlaid with the atomistic model (b) emphasizes the local distribution of WZ and ZB segments, reproduced from ref. [140]

However, the addition of halogens during synthesis has been reported to have an effect on the crystal structure of colloiddally grown nanostructures.^[137–139] An analogous approach was used to further influence the crystal structure of the SLS-grown CdTe QNWs. For comparability, the alkyl halides 1-chloroheptane, 1-bromoheptane and 1-iodoheptane were added before the reaction was heated to the aspired reaction temperature. Series of different molar equivalents of additives with respect to the amount of cadmium precursor were conducted in cooperation with Philip Harder and Florian Johst. As no significant differences upon variation of halides were observed, only the series using 1-bromoheptane is discussed here for the molar equivalents 0.5, 1.0 and 1.5 (Figure 5.2a). The mean diameters of the QNWs Br-Hep_{0.5} and Br-Hep_{1.0} were found to amount to (6.7 ± 1.0) nm and (6.7 ± 1.2) nm, while no reliable diameter could be retrieved for sample Br-Hep_{1.5}.

The most prominent feature of the QNWs is the amount of kinks that increases with higher molar equivalents of Br-Hep. The majority of the QNWs in Figure 5.2a₁ is straight and unbranched, whereas the QNWs in the center panel exhibit a lot of kinks that interestingly appear to have similar angles. The highest molar equivalent of Br-Hep evoked a multitude of kinks such as the aspired one-dimensional structure is hardly discernible. In the HRTEM of a kinked CdTe QNW synthesized with equimolar amounts of Br-Hep in Figure 5.2b three different segments can be defined. In the segments before and after the kink the WZ phase is prevalent, while the central part has ZB modification. This has further been backed using an atomistic model^[140] as an overlay to the HRTEM image. The kink itself seems indeed to be formed by a single ZB crystal, which evokes a change in growth direction with a distinct angle, ultimately resulting in further crystallization on one of the equivalent facets. The angle was observed to be $(70.9 \pm 8.8)^\circ$, which is in good agreement with the theoretical angle of 70.5° .^[141] It becomes apparent that the enlarged ZB segments evoke these kinks, if they are of sufficient extend as to allow crystallization on one of the facets. Therefore, a critical ZB-segment length, which is presupposed by the QNW diameter, can be defined.

The p-XRD analysis in Figure 5.3 does ratify the assumption of an increase of ZB with increasing amounts of additive. The stick patterns (bottom panel) represent the relative intensities of the various reflexes for both crystallographic configurations, namely WZ (blue) and ZB (gray), which are also listed in Table 5.1. The reference patterns reveal that the QNWs do exhibit polytypism. To render a conception of the orientation of the crystallographic planes within the one-dimensional nanostructures,

the normal vectors of the relevant planes in both, wz-QNWs (blue) and zb-QNWs (gray), are illustrated in Figure 5.3b. In case of these highly anisotropic heterostructures, those reflexes with longitudinal and those with radial contributions have to be discriminated as the different number of planes along and perpendicular to the growth direction of the NWs result in different coherence lengths, which in turn influences the width of the corresponding peak. The coinciding longitudinal reflexes WZ(002) and ZB(111) are mainly influenced by the phase alternations, while they should exhibit optimal signals in phase-pure species, due to the extensive coherence length along the NW. The FWHM of the predominantly radial reflexes WZ(100) and WZ(110)/ZB(220) on the other hand, can be used as a measure for the NW diameter.

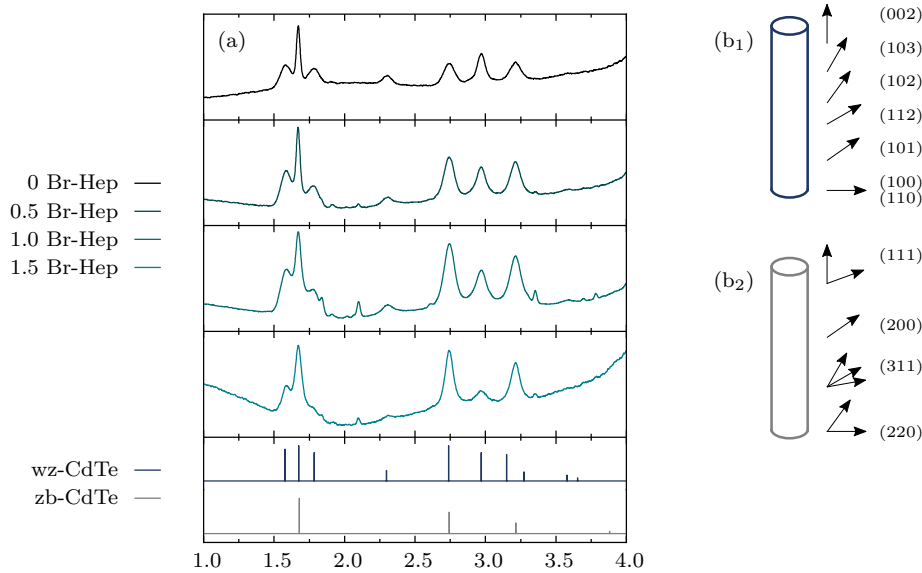


Figure 5.3: XRD of CdTe QNWs with Br-Hep additives. Powder diffractograms of CdTe QNWs (a) synthesized with different molar equivalents of Br-Hep additive, namely 0 (black), 0.5 (green), 1.0 (turquoise) and 1.5 (light blue). The stick patterns of wz-CdTe (PDF-no. 00-019-0193, top, blue) and zb-CdTe (PDF-no. 00-015-0770, top, gray) are shown for comparison in the bottom panel. The respective miller indices can be retrieved from Table 5.1. The orientations of the lattice-plane normals of WZ (b₁, blue) and ZB (b₂, gray) with respect to the NW are illustrated for clarification.

Contemplating the WZ(103)/WZ(110) ratio as proposed by Harder et al., the conventional CdTe QNWs (0 Br-Hep) were found to be mainly composed of WZ segments.^[88] The decrease of said ratio with increasing amount of Br-Hep further substantiates the assumption of an increase in ZB rate. Nonetheless, even in the extreme case of the 1.5 Br-Hep synthesis, the ZB rate does not exceed 50%, despite the strongly altered morphology.

Table 5.1: Reference X-ray diffraction reflexes of CdTe WZ (top) and ZB (bottom) crystal phase, respectively.

Miller index	q \AA^{-1}	I a.u.
(100)	1.58	0.9
(002)	1.68	1.0
(101)	1.79	0.8
(102)	2.30	0.3
(110)	2.74	1.0
(103)	2.97	0.8
(200)	3.15	0.75
(201)	3.27	0.25
(111)	1.68	1.0
(220)	2.74	0.6
(311)	3.22	0.3
(400)	3.88	0.06

One predicament of the kinks with respect to the characterization of the optical properties of the polytypic QNWs would be the altered surface chemistry in the kink region with respect to a conventional mainly-WZ QNW. Halides are furthermore used as passivation agents in colloidal nanostructures, which would introduce an additional parameter to be contemplated with respect to the recombination kinetics. Finally, the alkyl-halide treated QNW samples did not exhibit any PL signal at room temperature or even at cryogenic temperatures. The latter issue may be tackled by conducting the complete synthesis under inert atmosphere, as has proven to be advantageous for CdTe QNWs in general. A trade-off between kinks and the aspired longer ZB segments has to be made, when the aforementioned difficulty of insufficiently sized quantum wells shall be obviated. With ZB-segment length just below the critical value, mainly straight QNWs could probably be synthesized. The critical ZB-segment length does however directly translate into a maximal ZB-well size, which ultimately is on the order of the QNW diameter. For future utilization of these alkyl-halide treated QNWs, a detailed analysis of the resulting crystal phase distribution is necessary for different sets of reaction parameters with amounts of the alkyl-halide additives below equimolarity.

Consequently, conventionally-synthesized CdTe QNWs with a high WZ rate were used for the studies on the PL characteristics. For this analysis, the QNWs were sonicated and subsequently transferred onto a substrate via dropcasting. Initially, AFM studies were conducted to locate suitable QNWs. As a reliable distinction between single QNWs and small bundles of these colloiddally grown nanostructures could not be obtained and the CdTe QNWs proved to be susceptible to ambient conditions, this sample preparation step was foregone. In auxiliary TEM-studies, the tendency of the QNWs to form bundles could be confirmed. Preliminary electron-microscopic measurements were thus conducted to optimize the QNW concentration and reduce the size of the bundles before the PL characterization. Prior to the in-depth PL analysis, coarse rectangular scans were performed to discover luminescing structures of interest. These were probed with respect to their spectrally-resolved emission characteristic. Therefore, spectra were collected on structures that neither featured a multitude of concurring emission lines nor suffered from too low intensities. To retrieve information about both spatial inhomogeneities and temporal evolution, series of consecutive spectra were collected at several points along the wire axis.

Figure 5.4a reveals the temporal evolution of the emission at one specific point on the QNW. The PL was monitored over the course of 1 h with each spectrum being integrated for 2 s. The spectral information is conveyed on the abscissa of the graph and the time is plotted on the ordinate, while the PL intensity is represented on a false-color scale.

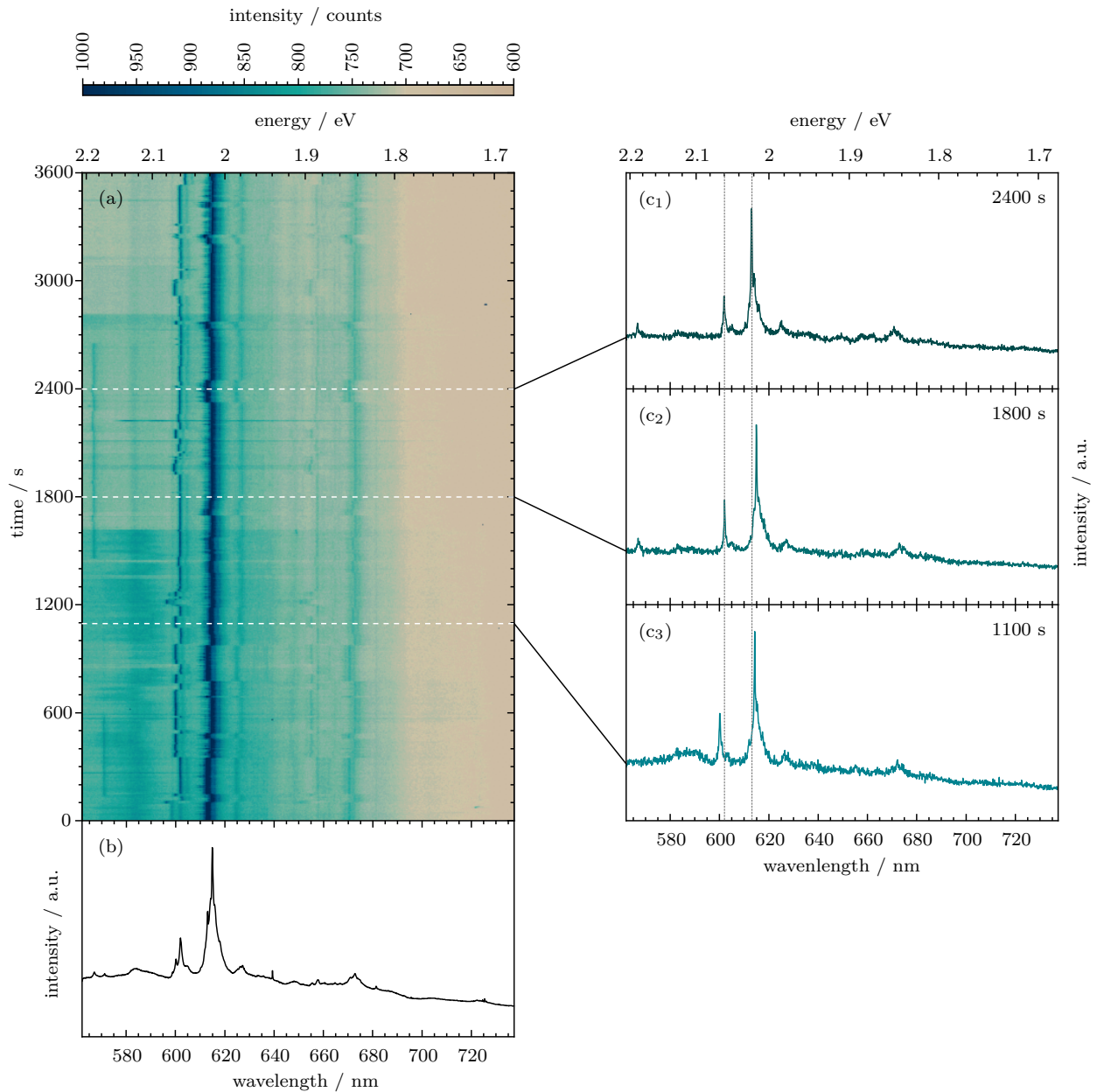


Figure 5.4: Spectral series of CdTe QNWs. The consecutive spectra (a) recorded with an integration time of 2 s have been obtained at cryogenic temperatures with CW excitation to monitor their temporal evolution. The sum spectrum (b) integrated over all spectra collected during the complete series, is depicted in the bottom panel. Three individual spectra (c) corresponding to the horizontal lines in (a) represent the PL emission at times 2400 s, 1800 s and 1100 s.

Each row comprises an individual spectrum recorded at a given time. In contrast, the sum spectrum that is integrated over the total monitoring time is depicted in the bottom panel in Figure 5.4b. Interestingly, the two main features at ~ 600 nm and ~ 613 nm exhibit sharp maxima and distinct side peaks, rather than an inhomogeneously broadened peak, which would be initially expected in case of spectral migration. Indeed, are all the observed lines subject to spectral fluctuations that are, however, perceived as discrete jumps on the timescale of the measurement rather than the continuous wandering which was reported for CdSe QNWs. Furthermore, no pronounced intensity fluctuations are observable in these CdTe QNWs in contrast to the aforementioned sample system, where switching between strong emission ("on state") and no emission "off state" is common.

Note, that the recorded emission is at relatively high energies for CdTe at cryogenic temperatures, even when considering strong confinement effects. Treating the polytypic QNWs as superstructures of individual one-dimensional quantum wells in first approximation, the Brus formula that is detailed in Equation 2.7 can be utilized to estimate the effective band gap of the QNW segments. Assuming a mean QNW diameter of 6.9 nm, the parameters of bulk CdTe detailed in Table 2.1 and a relative permittivity of 10.16, the effective band gap increases to 1.95 eV. To exclude other points of origin for these high-energy emission lines such as impurities in the substrate, different types of substrates were used. While an origin of the emission other than the QNW can not be disregarded completely, due to the nature of the synthesis, these characteristic emission lines were only found in regions in which QNWs were previously registered in a two-dimensional raster-scan.

Interestingly, Bi₂Te₃ nanostructures have been reportedly used as plasmonic enhancers,^[142] which could be beneficial to the otherwise weak PL signal emitted by the QNWs. Yet, the catalyst particle is commonly perceived as remaining intact and can usually still be located at the QNW tips, which would rather result in a highly localized enhancement with respect to the longitudinal extend of the one-dimensional semiconductor. The primary emission is thus assumed to originate from CdTe QNW species.

For a more detailed insight into the temporal evolution of the spectral discontinuities, three individual spectra representing the PL emission at different times are depicted in Figure 5.4c with the corresponding frames being highlighted by dashed white lines in panel (a). The vertical dashed lines mark the peak positions of the emission at 2400 s and serve as a guide to the eye to evaluate the spectral shifts in the other frames. It can be seen, that the two distinct features at ~ 600 nm and ~ 613 nm change independent from each other. The higher energy peak in frame 1800 s in (c₂) appears at the same spectral position, while the lower energy one is slightly bathochromically shifted with respect to the reference in (c₁). In the individual spectrum at 1100 s in panel (c₃), the latter peak appears in the same position as in (c₂), while the first peak is shifted to slightly higher energies.

The second particularity in the spectral series in Figure 5.4a are line replicas of the previously discussed primary lines. The most prominent replica can be discerned at ~ 655 nm and ~ 673 nm for the higher and lower energy primary line, respectively. The discrete nature of the spectral intermittency and, consequently, the unique temporal evolution of the emission lines is propitious for the identification and assignment of the line replicas. To gain perspective on the origin of these PL emission peaks including the primary lines and the replicas, the low-temperature spectrum of a classical bulk CdTe sample reported in literature is depicted in Figure 5.5.^[143]

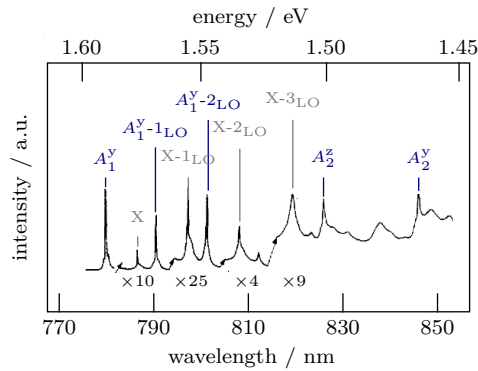


Figure 5.5: Example PL spectrum of bulk CdTe at 5 K. The spectrum of the p-type crystal is dominated by the principal bound-exciton lines of acceptors "y" and "z". Reproduced from ref^[143].

This study discussed shallow acceptors A and donors D as cause for defect levels as opposed to deep native defects such as Cd vacancies or interstitials. In the presence of these impurity centers, the photo-excited exciton (X) can form neutral defect-bound exciton complexes. Recombination of these three-particle complexes entails the annihilation of the exciton, while the hole of the neutral acceptor (or the electron of the neutral donor) typically remains in its ground state.

In the case of the high-purity p-type crystal, the two distinct lines A_1^y and A_1^z in the NBE region were identified as the principal bound-exciton lines (blue) of the two neutral acceptors A^y and A^z . In addition to the lines attributed to the bound-exciton recombination, a sequence of phonon replicas with an energy separation of 21.3 meV that are denominated $A_1^y - n\text{LO}$ has been reported. Recombination of the free exciton evokes a similar sequence of replicas $X - n\text{LO}$, but shifted to lower energies with respect to the complex. The additional lines A_2^y and A_2^z are attributed to two-hole transitions that arises, if the hole of a neutral acceptor remains in an excited state. Broader peaks at lower energies (not displayed) can be assigned to transitions between ionized acceptors A^- and donors D^+ forming donor-acceptor pairs (DAPs). In addition to the type of acceptor, the peak energy was reported to be influenced by the number of acceptor density and the excitation intensity.

Despite theoretical knowledge about these defect-induced lines, the accurate assignment of the NBE peaks in the PL spectra of nanostructures is impeded by spectral shifts and confinement effects.^[19,143] Furthermore, colloidally synthesized nanostructures are passivated by a multitude of different organic molecules and defects including lattice inhomogeneities and chemical impurities are prevalent.

5.1.1 Spectral Intermittency in CdTe QNWs

The temporal evolution of the emission in the high-energy section of the spectrum may render information about the type of luminescence center. To gain insight into the dynamics of the spectral discontinuities, the different groups of emission lines in Figure 5.6a were investigated in detail. Both of these independent sets, situated around 600 nm (group I) and 613 nm (group II), have been found to comprise several distinct sublimes. For reasons of clarity, only the intensity profiles of the two most prominent sublimes a and b of each group were extracted as time-traces. The normalized time-traces are illustrated in the panels b₁ and b₂ of Figure 5.6, while the respective histograms of "on" and "off-states" corresponding to the individual sublimes are depicted in Figure 5.6c. The slope of the extracted data originates from the overall decrease of PL intensity during the measurement.

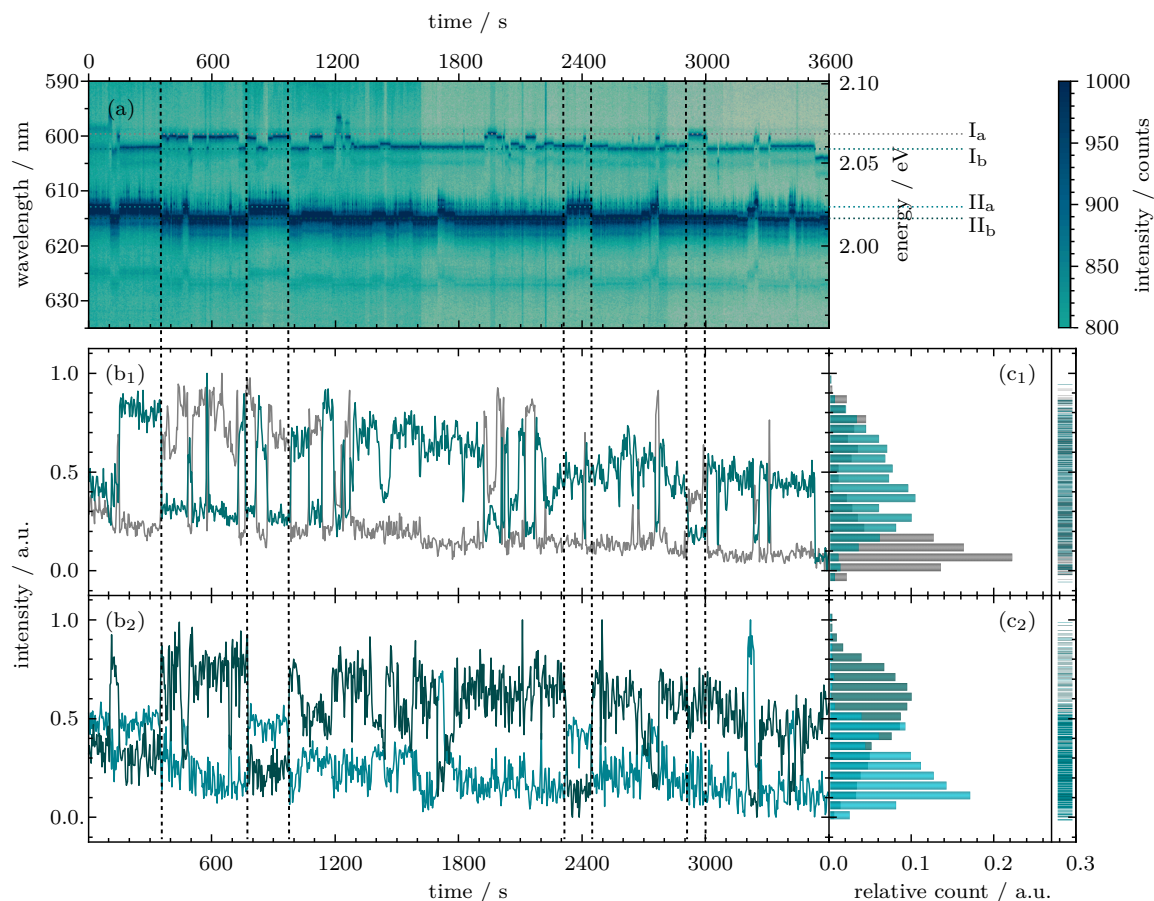


Figure 5.6: Temporal evolution of the high-energy signals. The spectral series of the main peaks is represented on a color scale (a). Two complementary timetraces have been extracted of both emission-line groups around 600 nm (b, top) and 613 nm (b, bottom), respectively. The corresponding histograms show the distribution of on and off-states (c).

The high-energy subline I_a (gray) of the first band I reveals distinct "on" and "off-states". The corresponding subline I_b (turquoise) exhibits a switching behavior that is complementary to the former subline. While I_a is predominantly switched off in the second half of the measurement, subline I_b shows an "on-state" that is affected by the overall loss of PL-intensity. Consequently, the pronounced bimodal distribution of the I_a histogram may not be observed in the I_b case. The sum of the two time-traces should reveal almost continuous "on-state" and "off-states" that are interrupted by small intervals in which neither of the two chosen sublines contribute to the emission of the group. These intermittencies arise from additional sublines (e.g. at 1200 s and 3550 s) that were excluded from the analysis due to their short overall on-time. The emission of the complete group of lines is continuous in time and only discontinuities in spectral position occur. A similar behavior can be observed within the second band II. Due to the higher PL intensity of sublines II_a (blue) and II_b (green), the time-trace can not be as cleanly extracted as is the case for band I. In addition, one of the replica of subline II_a coincides with the spectral position of subline II_b . Thus a type of intermediate "gray-state" is spuriously registered. A threshold had to be defined accordingly to find a trade-off between recording an actual primary subline, discarding signal "leaking" from other lines and eliminating contributions from replicas. The complementary character of the sublines within their respective group indicates that they have the same origin that is subject to some type of local fluctuation. The groups themselves exhibit different switching frequencies and are thus found to originate in individual excitonic complexes.

In literature, the continuous spectral wandering in CdSe was attributed to charged defect sites promoting DAP recombination that is associated with trap emission. This was further backed by the presence of the pronounced LO-phonon sidebands, which are strongly promoted through the spatial configuration of ionized donors and acceptors.^[19] The line groups I and II in Figure 5.6a however, are spatially narrow which would rather indicate neutral defects as the cause of the emission. In addition, some kind of memory-effect is observable, when contemplating each group separately. Spectral discontinuities have been theorized to emerge from migrating charges inducing the quantum-confined Stark effect through manipulation of the local charge density, which typically evokes a continuous spectral shift. Switching between distinct emission lines, however, has been reported by Fernée et al., who hypothesized that the rearrangement of surface ligands induces variations in surface configuration.^[71]

To exclude the morphological characteristic as the cause for the spectral modulation, the exemplary HRTEM image of an individual CdTe in Figure 5.7a from the same batch was used as a basis for the model calculation of an exciton complex in the potential landscape formed by the phase alternations. Here, the same procedure for the allocation of crystal planes in NWs as already described before on Page 48 was employed, with the lattice planes being highlighted in the established color code. The self-consistent calculations were performed by solving the Schrödinger equation on a three-dimensional grid, as was detailed by Franz et al.^[19] The resulting localization of the electron-hole pair in the quasi type-II potential landscape is shown in Figure 5.7b, where the vertical axis represents the energy, while the horizontal axes indicate the radial and axial extend of the calculated segment. For the construction of the potential landscape, the aforementioned band gaps and the CB offset of CdTe were applied in combination with a QNW diameter of 7.6 nm and an external potential of 5 eV. The grey potential wells signify the potentials of electron and hole including the potential of the QNW generated by the crystal structure and the Coulomb interaction between the charge-carriers. The surface plots visualize the calculated charge-carrier wave functions and reveal the insufficient extend of the ZB segments. These wells proof to be too small as to effectively confine the holes, while the electrons could probably be confined to the individual WZ segments. However, charge-separation would be ineffective if only one charge-carrier is confined, while the other remains mobile. This could indicate that some configurations are more favorable and thus introduce the surmised memory effect. The observed phase alternations may also contribute to the formation of multiple default passivation-situations that occur repeatedly and further add to the complexity of the overall potential landscape.

Surfactants are assumed to be involved in the formation of the additional NIR replicas of both, group I and group II, discernible in Figure 5.4. These were further evaluated by determining the spectral position of the respective primary subline and noting the relative spectral positions of all corresponding replicas. With most of those replicas being located well above 1200 cm^{-1} , it is assumed that they are of organic origin, namely vibrations attributed to the functional groups of the ligands, rather than being evoked by lattice vibrations of the semiconductor. It was reported by Lifshitz that the surface-ligand bonding may not only introduce additional electronic states, but that crystalline electronic states could potentially couple to molecular vibrational states.^[144]

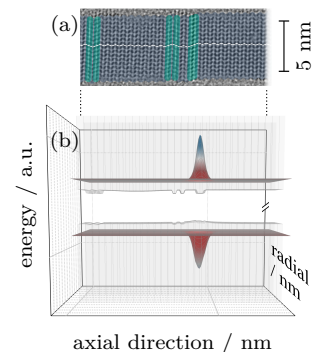


Figure 5.7: Model calculation for the WZ/ZB potential landscape. The crystal phase alternations of WZ (blue) and ZB (turquoise) of the CdTe QNW depicted in the HRTEM (a) was used to template the calculation of the exciton complex in the quasi type-II potential landscape (b) of the longitudinal heterostructure. The surface plots localize the charge-carrier wave functions along the QNW.

5.1.2 Surface Characteristics of CdTe NWs

To gain insight into the nature of the NIR-replicas, the vibrational characteristics of the organic surfactants were probed by means of Fourier transform IR (FTIR) spectroscopy. This method has previously been utilized to monitor the ligand-exchange reaction between TOPO-capped cadmium chalcogenide NPs and surfactants such as pyridin and oleic acid.^[145,146]

Here, the IR bands of the ligand-capped CdTe NWs are compared to those inherent to the ligands and the cadmium precursors. Additionally, as-grown CdTe NWs were heated to 600 °C under nitrogen atmosphere in a TGA setup to remove the organic ligands from the surface of the semiconductor and FTIR spectra of these purified NWs were obtained. The CdTe NWs with the intact ligand shell (CdTe/Lig NWs) exhibit a multitude of vibrational bands that concur well with the characteristics of DOPA and TOPO, which were used as ligands and solvent during the SLS synthesis. The coordination of the primary ligand DOPA to the cadmium surface-sites of the NW may be best represented by the cadmium precursor $\text{Cd}(\text{DOPT})_2$. This cadmium complex has been synthesized from cadmium acetate and the phosphinic acid. To exclude that residues of acetate on the NW contribute to the IR spectrum of the CdTe/Lig NWs, the original cadmium compound was included in the investigation. Furthermore, cadmium oxide (CdO) was added to the measurement series, as cadmium chalcogenide nanostructures are prone to partial oxidation of the surface due to insufficient ligation.^[147]

Based on the characteristic absorption by specific functional groups, the IR spectra of the organic ligands may be classified into two frequency regions, namely functional-group and fingerprint ($< 1500 \text{ cm}^{-1}$) region. The distinctive IR bands corresponding to stretching vibrations ν of the alkyl chain are situated in the high-frequency region. The fingerprint region that contains multiple IR peaks arising from various deformation vibrations was subdivided into a medium and a low-frequency domain. The former region primarily includes in-plane deformation modes δ and stretching modes of double bonds. The low-frequency region comprises deformation modes originating from out-of-plane vibrations. While the fingerprint region is highly specific and allows for identification of organic molecules, the detailed analysis of individual modes is tedious due to the abundance of functional groups and thus vibrational frequencies. However, the medium-frequency domain is of the most interest when analyzing the coordination of the ligand to the semiconductor surface as the vibrational modes of the anchoring group are located within this region.

The normalized IR spectra of the different systems are shown in Figure 5.8a, while the corresponding molecular structures with their respective functional groups are complementary illustrated in Figure 5.8c. The possible anchor groups of the cadmium precursors (top), CdTe NWs (center) and free molecules (bottom) are highlighted with squared markers. The components of the hydrocarbon remnants are exemplary marked with circles. The corresponding spectral positions of the vibrational features are color-coded in the IR graphs. An enlarged view of the medium-frequency region (Figure 5.8b) in which the characteristic IR bands of the anchor groups are located is presented for a detailed analysis of the relevant IR spectra.

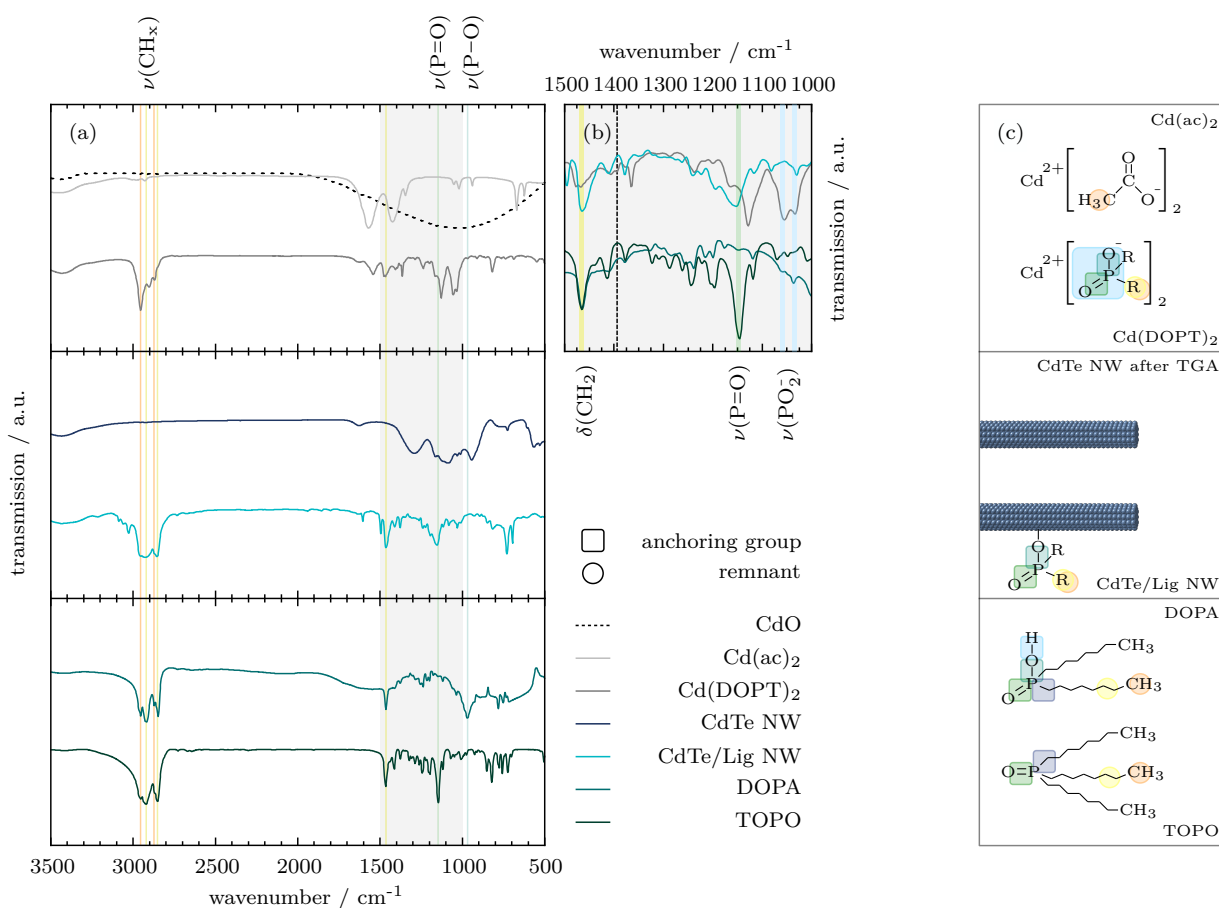


Figure 5.8: Vibrational characteristics of the organic medium. FTIR spectra of the cadmium precursors (a, top), the semiconductor system before (CdTe/Lig) and after (CdTe) TGA (a, middle) and the ligands (a, bottom). Prominent frequencies of the different functional groups are highlighted in the enlarged representation of the fingerprint region between 1500–1000 cm⁻¹ (b). The functional groups are specified in the schematics of the molecular structure of the investigated precursor (c, top), CdTe NW (c, center) and ligand (c, bottom) systems.

The coordinating solvent **TOPO** that is commonly used for synthesis of anisotropic nanostructures has been characterized extensively and is thus used for comparison. Furthermore, the molecule may act as surfactant if the ligation of the nanostructure by the designated ligand is insufficient.^[148] The peak positions retrieved from the IR spectrum of the free molecule are in good agreement with those found in the literature.^[146,149] The prominent peaks in the functional-group region that are located at 2952/2869 cm^{-1} and 2918/2850 cm^{-1} may be attributed to the asymmetric and symmetric stretching vibrations of the CH_3 (orange) and CH_2 (yellow) groups that constitute the long alkyl chains, respectively. Likewise, the absorption in the fingerprint region at 1465 cm^{-1} and below 850 cm^{-1} can be assigned to the in- and out-of-plane deformation vibrations of the CH_2 group, respectively. The P=O stretch mode of the anchor group has been identified at 1145 cm^{-1} . TOPO has been reported to bind to the cadmium surface atoms via the P=O (green) head group, which results in both, frequency and amplitude changes of the vibrational mode.^[145]

The primary ligand **DOPA** that was introduced into the system as the cadmium precursor preferentially coordinates to the NP surface via the P–OH (turquoise) group. More specifically, the anhydride DOPT tightly binds to the cadmium ions.^[150,151] Thus, the free molecule as well as the $\text{Cd}(\text{DOPT})_2$ complex were investigated. While the P=O stretch vibration of the phosphinic acid at 1145 cm^{-1} is very weak in the DOPA spectrum, the P–OH stretch mode at 968 cm^{-1} is clearly discernible. The broad feature between 1500–1850 cm^{-1} can be attributed to the OH vibration.^[152] The absence of both IR bands assigned to the components of the P–OH group in combination with the additional peaks at 1056 cm^{-1} and 1033 cm^{-1} in the spectrum of the **cadmium complex** indicates a monodentate configuration via the oxygen lone-pair electrons of the deprotonated acid group. This is further confirmed by the intensity of the distinct P=O mode at 1128 cm^{-1} . The additional modes correspond to the asymmetric and symmetric stretch frequencies of the PO_2^- (blue) head group of the ligand.

The spectral position of the more distinct peaks in the IR spectra of the unbound ligands and their assignment to the absorption by the vibration modes of different functional groups are given in Table 5.2. The peak assignment for the IR spectrum of the commonly used solvent TOPO was adopted from the literature and subsequently adapted to the peaks observed in the absorption spectrum of DOPA.^[149] In addition to the type of vibration, namely stretching ν , in-plane δ and out-of-plane γ deformation, the intensity of the respective peaks is specified.

Table 5.2: IR vibrational frequencies and the corresponding functional groups of the organic medium.^a

System	Observed peak position and assignment					
	3000–1500 cm ⁻¹		1500–1000 cm ⁻¹		1000–500 cm ⁻¹	
TOPO	2952 [s]	$\nu_{as}(\text{CH}_3)$	1465 [s]	$\delta(\text{CH}_2)$	850 [m]	$\gamma(\text{CH}_2)$
	2918 [s]	$\nu_{as}(\text{CH}_2)$	1413 [m]	$\delta_s(\text{CH}_3)$	821 [m]	$\gamma(\text{CH}_2)$
	2869 [sh]	$\nu_s(\text{CH}_3)$	1377 [m]	$\delta_s(\text{CH}_3)$	777 [m]	$\gamma(\text{CH}_2)$
	2850 [s]	$\nu_s(\text{CH}_2)$	1286 [w]	$\delta(\text{CH}_2)$	756 [m]	$\gamma(\text{CH}_2)$
			1244 [m]	$\delta(\text{CH}_2)$	723 [m]	$\gamma(\text{CH}_2)$
			1195 [m]	$\delta(\text{CH}_2)$		$\gamma(\text{CH}_2)$
			1145 [s]	$\nu(\text{P}=\text{O})$		
		1118 [sh]				
DOPA	2952 [s]	$\nu_{as}(\text{CH}_3)$	1463 [s]	$\delta(\text{CH}_2)$	781 [m]	$\gamma(\text{CH}_2)$
	2920 [s]	$\nu_{as}(\text{CH}_2)$	1409 [w]	$\delta_s(\text{CH}_3)$	752 [m]	$\gamma(\text{CH}_2)$
	2871 [sh]	$\nu_s(\text{CH}_3)$	1377 [w]	$\delta_s(\text{CH}_3)$	715 [m]	$\gamma(\text{CH}_2)$
	2846 [s]	$\nu_s(\text{CH}_2)$	1284 [w]	$\delta(\text{CH}_2)$		
			1253 [sh]			
			1238 [m]	$\delta(\text{CH}_2)$		
			1198 [sh]	$\delta(\text{CH}_2)$		
			1145 [w]	$\nu(\text{P}=\text{O})$		
			1118 [w]			
			1037 [m]			
		968 [s]	$\nu(\text{P}-\text{OH})$			

^a The indices s and as refer to the symmetric or asymmetric stretching (ν), in-plane (δ) and out-of-plane (γ) deformation vibrations, respectively. The intensity is indicated by the symbols [s], [m], [w], [sh] and [br] translating to strong, medium, weak, shoulder and broad.

Since the precursor was synthesized using **cadmium acetate**, the IR spectrum of this preliminary cadmium source is ascertained. Due to the small size of the acetate, the number of IR bands is comparably low. Similarly to the long-chained molecules, the stretch modes and the out-of-plane deformation modes of the methyl group are distinguishable in the functional-group and the low-frequency fingerprint region, respectively. The two pronounced IR bands at 1570 cm⁻¹ and 1421 cm⁻¹ correspond to the asymmetric and symmetric stretch modes of the carboxylate surface anchor group.^[153] Residues of the acetate may evoke the $\nu_{as}(\text{COO}^-)$ mode at 1541 cm⁻¹ present in the spectrum of Cd(DOPT)₂. However, metal and organic ligand are cleaved during NW synthesis and the low boiling point of the free acetic acid at 118 °C^[154] in combination with the high excess of the phosphinic acid in relation to the number of cadmium surface sites should preclude the adsorption of the acetate on the NW.

The IR spectrum of the ligand-capped **CdTe/Lig NWs** exhibits a multitude of vibrational bands. The features in the functional-group region are in good agreement with the absorption arising from the alkyl chains. The additional signals above 3000 cm^{-1} can be attributed to aromatic C–H stretch modes of toluene. Residues of the storing solvent may have remained in the CdTe/Lig sample after the preparation procedure, which included centrifugation and subsequent drying of the precipitate. The auxiliary features at 1604 cm^{-1} and 1494 cm^{-1} may equivalently be ascribed to the C–C stretch modes in the aromatic ring. While the CH_2 -deformation vibration at 1463 cm^{-1} and the P=O stretch vibration at 1149 cm^{-1} that are characteristic of both phosphorus-based ligands are intense, neither the P–OH band of the free DOPA nor the doublet associated with the PO_2^- mode of the anhydride are clearly discernible.

However, even after the purification process of the NW dispersion, a perceptible amount of the original synthesis solvent TOPO remains in the sample. The long-chained phosphine oxide is likely to build a network of molecules around the nanostructure. While an organic shell with a thickness of several ligand layers is formed, only a fraction of the molecules is adsorbed onto the anorganic surface. Consequently, the IR spectrum of the CdTe/Lig sample may primarily comprise absorption modes arising from unbound TOPO. For TOPO saturating the dangling bonds on the surface of CdSe NPs, an experimental red-shift of the P=O stretch vibration of $\sim 60\text{ cm}^{-1}$ was reported.^[145] Here, the peak position remains unaltered with respect to the free TOPO spectrum. The broadening of the peak may be evoked by a superposition of multiple absorption modes of the different residues present in the sample. Thus, the signal of the bound DOPT may be concealed by the excess of the free molecules in the multilayer organic shell.^[155] To exclude, that the peaks originate from preliminarily unpassivated and subsequently oxidized surface sites, cadmium oxide was included in the investigation. The IR spectrum of the substance (dashed line) exhibits a broad signal spanning the whole of the fingerprint region. Due to the small width of the modes in the CdTe/Lig NW spectrum, it is safe to assume, that the peaks are of organic origin.

In accordance to the peak assignment of the unbound organic molecules, the IR modes of the cadmium complexes are itemized in Table 5.3. Supplementarily to the vibrations of the free ligands, those of acetate and toluene were retrieved from the literature for a comprehensive analysis. While the origin of the majority of the modes could be established, some peaks remain unassigned. The low-frequency vibration can most likely be attributed to deformation modes within the alkyl chain.

Table 5.3: IR vibrational frequencies and the corresponding functional groups of the cadmium complexes.^a

System	Observed peak position and assignment					
	3000–1500 cm ⁻¹		1500–1000 cm ⁻¹		1000–500 cm ⁻¹	
Cd(DOPT) ₂	2954 [s]	$\nu_{\text{as}}(\text{CH}_3)$	1467 [d]	$\delta(\text{CH}_2)$	858	$\gamma(\text{CH}_2)$
	2902 [m]	$\nu_{\text{as}}(\text{CH}_2)$	1406 [w]	$\delta_{\text{s}}(\text{CH}_3)$		
	2868 [m]	$\nu_{\text{s}}(\text{CH}_3)$	1377 [sh]	$\delta_{\text{s}}(\text{CH}_3)$		
	2846 [sh]	$\nu_{\text{s}}(\text{CH}_2)$	1365 [m]			
	1625 [w]		1236 [w]			
	1541 [m]	$\nu(\text{CO}_2^-)$	1164 [sh]			
		residues	1128 [s]	$\nu(\text{P}=\text{O})$		
			1056 [s]	$\nu_{\text{as}}(\text{PO}_2^-)$		
		1033 [s]	$\nu_{\text{s}}(\text{PO}_2^-)$			
Cd(ac) ₂	2927 [w]	$\nu_{\text{s}}(\text{CH}_3)$	1421 [s]	$\nu_{\text{s}}(\text{CO}_2^-)$	939 [w]	
	1570 [s]	$\nu(\text{CO}_2^-)$	1342 [m]	$\delta_{\text{s}}(\text{CO}_2^-)$	669 [m]	
			1049 [w]	$\nu_{\text{s}}(\text{C}-\text{OH})$	622 [m]	
			1020 [w]	$\nu_{\text{s}}(\text{C}-\text{C})$		
CdTe/Lig NW	3086 [w]	$\nu_{\text{r}}(\text{CH})$	1494 [m]	$\nu(\text{C}-\text{C})$	846 [w]	
	3060 [w]	$\nu_{\text{r}}(\text{CH})$	1463 [s]	$\delta(\text{CH}_2)$	817 [m]	
	3026 [m]	$\nu_{\text{r}}(\text{CH})$	1409 [m]	$\delta_{\text{s}}(\text{CH}_3)$	729 [s]	
	2954 [sh]	$\nu_{\text{as}}(\text{CH}_3)$	1377 [m]	$\delta_{\text{s}}(\text{CH}_3)$	694 [s]	
	2922 [br]	$\nu_{\text{as}}(\text{CH}_2)$	1240 [w]	$\delta(\text{CH}_2)$		
	2869 [sh]	$\nu_{\text{s}}(\text{CH}_3)$	1222 [d]			
	2854 [s]	$\nu_{\text{s}}(\text{CH}_2)$	1193 [m]			
	1604 [m]	$\nu_{\text{r}}(\text{C}-\text{C})$	1149 [s]	$\nu(\text{P}=\text{O})$		
		1116 [sh]				
		1082 [m]				
		1029 [m]				

^a The indices s and as refer to the symmetric or asymmetric stretching (ν), in-plane (δ) and out-of-plane (γ) deformation vibrations, respectively. The intensity is indicated by the symbols [s], [m], [w], [sh] and [br] translating to strong, medium, weak, shoulder and broad.

The surfactants of the original CdTe/Lig NWs were thermally removed at up to 600 °C to prepare a pure anorganic CdTe-NW sample. A thermogravimetric analysis was conducted concurrently to monitor the ligand-stripping process. This method allows for the analysis of thermal characteristics via variations in substance mass that are induced by temperature changes. Information about thermal stability, phase transitions and desorption can be retrieved from the shape of the resulting TGA curve. The first derivative of the thermogravigram (DTG curve) is commonly utilized for a detailed analysis of the inflection points that are critical to determine the nature of the thermally induced processes.

The TGA curves (colored) and the respective derivatives (dashed) of the CdTe/Lig NW (top) sample as well as those of pure unbound DOPA (center) and TOPO (bottom) are shown in Figure 5.9a. The fingerprint region of the corresponding FTIR spectra is reproduced in Figure 5.9b, accordingly. The spectra of the NW samples before and after the TGA procedure are illustrated in light blue (CdTe/Lig) and dark blue (CdTe), respectively. The measurements were conducted with a heating rate of $20\text{ }^{\circ}\text{C min}^{-1}$ at normal pressure under nitrogen atmosphere.

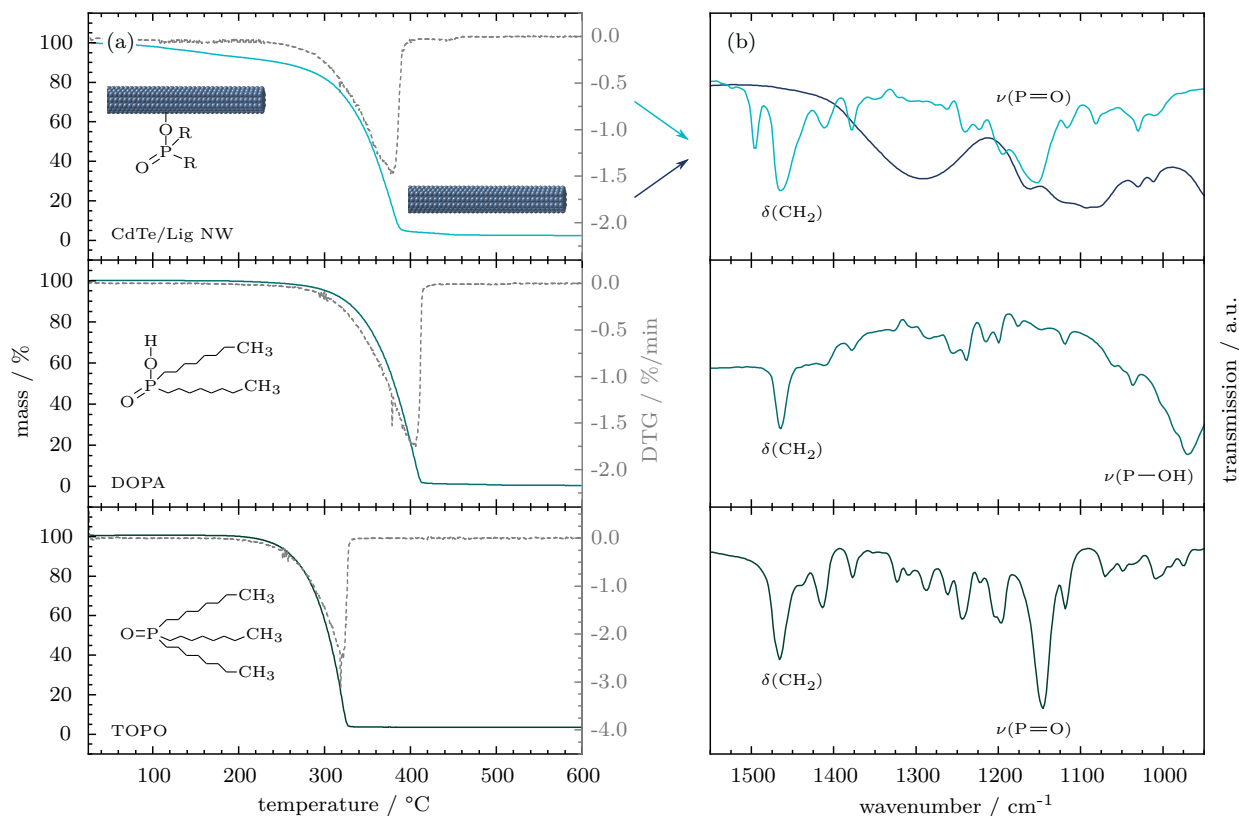


Figure 5.9: Thermogravimetric analysis of the organic ligands and the CdTe/Lig NWs. Thermogravigrams (colored) and the respective differentials DTG (gray) (a) of the CdTe/Lig NWs (top) and the ligands DOPA (center) and TOPO (bottom). The relevant vibrational peaks are labeled in the corresponding IR spectra (b) of the free ligands and the NW sample before (CdTe/Lig, light blue) and after (CdTe, dark blue) the TGA.

The thermogravigrams of the pure ligands each exhibit only a single degradation step. In both cases the sample mass remains nearly constant until a temperature of $261\text{ }^{\circ}\text{C}$ for DOPA and $210\text{ }^{\circ}\text{C}$ for TOPO is reached. The degradation peaks observable at $411\text{ }^{\circ}\text{C}$ (DOPA) and $326\text{ }^{\circ}\text{C}$ (TOPO) marks the end of the thermal response. The steep slope indicates a rapid mass loss due to vaporization of the aliphatic molecules. The mass of the thermally stable residues amounts to 0.5% and 3.5% , respectively.

The thermogravigram of the CdTe/Lig sample however, reveals a slow mass loss of 10% until a temperature of 246 °C is reached. The subsequent stark thermal response ceases at a temperature of 389 °C. The observed temporary plateau corresponds to a remaining mass of 5.6%. A final thermally stable state is reached at 453 °C as indicated by the DTG curve. The mass of the residue amounts to 2.7%. Evaluation of the DTG curve renders two different thermal processes within the initial slow response that may be attributed to the vaporization of water and toluene and thus, drying of the sample. Furthermore, the inhomogeneous shape of the degradation peak suggests the concurrence of two thermal processes. The low-temperature shoulder may potentially be attributed to the vaporization of the free TOPO, while the global minimum of the differential could indicate the loss of unbound excesses of DOPA. The small final decrease may be evoked by the desorption of the anhydride bound to the cadmium surface sites of the semiconductor.

The small amount of the thermally stable component could indicate a loss of the complete sample system including the semiconductor instead of mere elimination of the organic fraction. However, similar semiconductor/ligand systems of different shapes have been experienced to have large thermally stable amounts. A more likely cause for the small residual mass is the difficulty to sufficiently purify QNW suspensions. Excessive amounts of free ligand were probably transferred into the crucible, which would further explain the texture of the sample that appeared jellylike and would further back the assumption of a larger organic matrix around the untreated CdTe/Lig NW, which significantly affects the FTIR spectrum of the as-synthesized sample. Despite the slender amount of inorganic residues, enough material of the TGA-treated sample could be gained from the crucible and subjected to an FTIR analysis. As the final desorption of an organic species during TGA indicates the presence of an actual passivating surfactant-layer, the FTIR spectrum of Cd(DOPT)₂ will be used as an additional reference to circumvent the corruption of the CdTe/Lig spectrum by the excessive amounts of free organic molecules.

Comparison of the FTIR spectra of the as-synthesized CdTe/Lig NWs (light blue) and the bare CdTe NWs (dark blue) in the top panel of Figure 5.9b reveals strong deviations in vibronic response. First, the alkyl signals in the region above 1350 cm⁻¹ are completely suppressed in the TGA-treated sample, validating the successful removal of any alkyl species. The alteration of the peak shape below in the head-group region renders further evidence towards the presence of mainly the inorganic material.

The FTIR fingerprint-regions of the precursor $\text{Cd}(\text{DOPT})_2$ and the $\text{CdTe}/\text{Lig-NW}$ sample are reproduced in Figure 5.10a for comparison to the NIR replicas in panel (b), which were extracted from the spectral series. The spectral shifts of the replicas were obtained by determining the spectral position of the primary zero-phonon line and subsequently noting all replicas in a selection of representative individual spectra. In each frame, five separate readings were conducted in order to reduce observer's bias. The stick-pattern intensity of the four sublines in Figure 5.10c was chosen to represent the emission intensity as it was observed in the spectral series as opposed to the frequency with which the line was read out in the procedure. The number of replicas found for the sets I_a – II_b remained constant within the sets throughout the series. Only towards the end of the measurement some replicas became hardly discernible, which can however be attributed to the overall decrease in intensity.

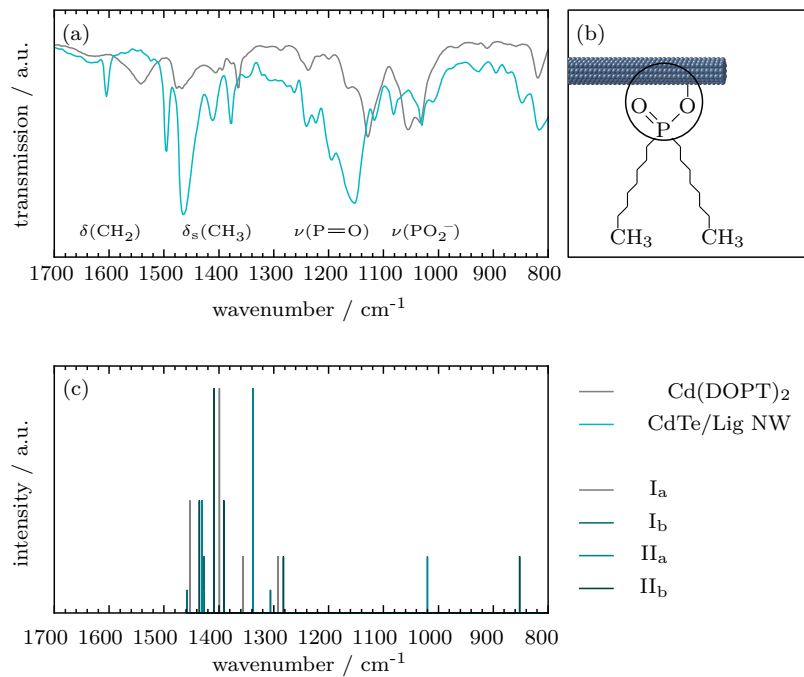


Figure 5.10: Vibrational characteristics of the $\text{CdTe}/\text{Lig NWs}$. FTIR spectrum (a) of the as-synthesized CdTe/Lig system and the NIR replicas (b) retrieved from Figure 5.4 that are color-coded according to their respective zero-phonon line. The surmised semiconductor–ligand system is sketched in (c)

Together, these lines form a pattern of vibrations that does indeed strongly resemble the fingerprint IR-spectrum of organic molecules such as DOPA. Interestingly, most replicas are registered in the region above 1250 cm^{-1} , which coincides with the vibrational frequencies of the alkyl chains rather than the head-group.

The latter is the functional group that would intuitively be considered first, when contemplating excitation–ligand coupling, due to its close proximity and actual coordination to the surface of the nanostructure as is sketched in Figure 5.10b. The vibroelectronic coupling in colloidal CdTe nanocrystals has already been evidenced by Noblet et al., who used a two-color sum-frequency setup to excite the ligand vibration with the IR-fraction while the semiconductor was probed with the visible light laser. There, five ligand vibration modes were identified that exhibited a visible-wavelength dependent intensity response, although most of the corresponding IR modes are not coordinated to the surface sites. Further, this spectroscopic procedure was reported to unveil variations in ligand disorder.^[156,157] Finally, the non-radiative electronic-to-vibrational energy transfer (EVET) can couple vibrational modes to electronic transitions in a multi-phonon process. In case of a large Huang–Rhys factor, even the bridging of multiple bonds was reported. The underlying mechanism of EVET remains under debate and different hypotheses including hybridized electronic states at the interface, resonant EVET and dipole–dipole coupling have been proposed.^[158]

While the retrieved replicas can not yet be allocated to an IR mode, the similarity of the two types of spectra in Figures 5.10a & c are striking. It should be noted, that the replica spectrum was obtained at cryogenic temperatures, while the FTIR spectra were recorded at ambient conditions, which might induce energetic shifting of the vibration modes. Future investigations, including the use of different ligands, could help to shine light onto the mechanism inherent to the EVET process.

Postsynthetic Surface Treatment

As discussed in the previous sections, the coordination type of the ligands and the resulting interaction strength, as well as the surface coverage, play a crucial role when tailoring the emission of nanostructures. The coordination of the ligand molecules to the surface sites is mainly determined by the anchoring group, while the overall surface coverage is to an extent also influenced by the geometry of the ligand due to sterical hindrance. However, the respective ligand systems are well established to obtain nanostructures with the desired geometry and crystal structure. A postsynthetic surface treatment poses an excellent possibility to investigate the benefits of various ligands while retaining the original structural properties.

Ligand Removal via Heat Treatment

In a first approach, a simple ligand-removal procedure by exploiting the thermal response of the semiconductor–ligand interface that induces the ligand-desorption during TGA. Instead of loading a crucible with the dried ensemble sample, the NWs were first transferred onto a marked substrate and analyzed regarding their spectral characteristics. Subsequently, the complete substrate was placed in the TGA setup and the conventional TGA procedure was conducted under inert atmosphere before the sample was placed in the cryostat for further investigation. However, no emission was observed after heat-treatment, although the presence of the NWs could be confirmed atomic-force microscopically. This could either be due to the excessive amount of newly exposed dangling bonds and the concomitant increase in trap sites, or degradation of the unpassivated surface. Furthermore, CdTe has been found to be highly sensitive to ambient atmosphere, which is why they are mounted in the cryostat in a nitrogen stream. This precaution is however not possible when conducting the heat treatment in the TGA setup. Nonetheless, the suppression of all kinds of emission lines including the NIR replicas does imply an organic origin for these secondary features.

Organic Ligand Exchange Reaction

Naturally, the preservation of primary emission is desirable. In order to tackle the issue of surface degradation resulting from the heat-treatment approach, LERs were conducted. The final ligands had to meet the prerequisite of comprising fundamentally different functional groups than the original surfactant system. Within the confines of this condition, organic molecules that had been reportedly used in LERs on similar material systems, have been selected. Apart from the primary objective of altering the NIR replicas, which are hypothesized to originate from the functional groups, these distinctive variations facilitate the verification of the LER. Consequently, pyridine was chosen as the aspired ligand system. Additionally, octanoic acid was considered as an alternative ligand to the aggregation-prone pyridine. But due to the limited amount of sample available for the surface-treatment experiments, a choice between the two options had to be made with the ease of the LER outweighing the potentially better colloidal stability. Besides, does pyridine provide better deviation from the original capping ligand with respect to functional groups. The success of the LER detailed in Subsection 2.5.2 was monitored using NMR spectroscopy. Figure 5.11 discloses the obtained ^1H -NMR spectra of

CdTe/TOPO (green) and CdTe/pyr and the corresponding free ligands. The comparison of the two NW spectra reveals similar signals between 0.5 ppm–1.5 ppm, which can clearly be attributed to TOPO. Although a small pyridine contribution can be distinguished at 8.5 ppm, the purification and ligand-exchange procedure was probably insufficient. Therefore, no quantitative analysis of the NMR-data was performed. In order to pursue this branch of experiments, designated NW samples only for the purpose of advancing ligand-exchange procedures on these colloiddally instable structures should be synthesized. This would allow more extensive purification routines and the direct comparison of different secondary ligand systems. Employing DOSY-NMR on these samples could also contribute to the value of the analysis, as discrimination between bound and unbound species is more facile. However, the NMR investigation itself requires optimal timing as the stability of the suspension remains deficient.

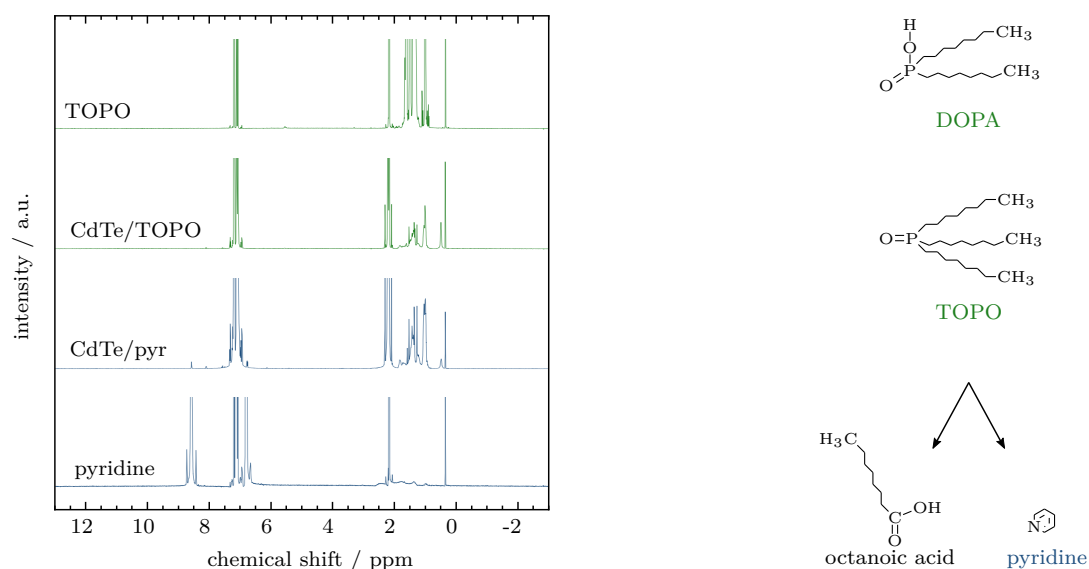


Figure 5.11: ^1H -NMR spectra of ligand-exchanged CdTe NWs. The CdTe/Lig NWs covered with TOPO (green) or pyridine (blue) and the corresponding pure ligands are compared in order to evaluate the success of the ligand-exchange reaction. The native ligands DOPA and TOPO as well as the ligands octanoic acid and pyridine, which were preliminarily selected for the exchange are schematically illustrated.

A conducive approach to the LER could be the implementation of a phase-transfer reaction, which ensures purging of excessive unbound ligands and may promote the exchange of the organic molecules. Such a procedure is already employed within the colloidal atomic-layer deposition of anorganic species.

5.2 Anorganic Ligand Exchange Reaction

The surface ligands do not only influence the optoelectronic properties of the nanostructures themselves but are reported to create highly insulating barriers around the colloidal nanomaterials.^[159] While an OLER to smaller molecules may decrease the thickness of the barrier and reduce the number of surface traps at the inorganic–organic interface, dangling bonds and charge-trapping surface sites will remain to some extent. The deposition of a few epitaxial monolayers of an anorganic material has been shown to sufficiently isolate the electron wave function from the unpassivated anionic sites.^[160] Furthermore, the anorganic shell provides means to modulate the charge-carrier confinement and thus the PL characteristics.

For the deposition of an epitaxial shell and thus tailoring of various hetero-nanostructures with high quality, precursor reactivity and concentration have to be adjusted precisely. The successive ionic layer adsorption and reaction (SILAR) method enables controlled shell growth while the secondary nucleation of separate NPs is contained. The layer-by-layer deposition technique is based on the calculation of the required amount of each precursor for the successive monolayers. The estimation of the total core surface-area is predicated on exact values for the nanostructure geometry and concentration. Insufficient addition of the respective precursors evokes incomplete layers, while an excess may favor secondary nucleation, especially since the free precursors remain in the reaction mixture.^[161] The exchange of the organic ligands with an anorganic species via the colloidal ALD technique allows for precise control of shell growth. The self-limiting nature of the half-reactions precludes the adsorption of more than one monolayer. Additionally, secondary nucleation is suppressed as the free precursors can efficiently be removed from the reaction.^[15] The phase transfer that is conducted during the exchange reaction is additionally beneficial to the control over the reaction as it renders feedback about the success of the ligand-stripping process. Especially the shell growth on anisotropic nanostructures is more attainable using the c-ALD method, since the tedious and inaccurate computation of the core surface-area is redundant.

Here, CdSe NWs were used as core material to have an additional feedback and exploit the room-temperature photoluminescence, which is not observable for CdTe NWs. Other characteristics like synthesis parameters and the resulting geometry and crystal structure are comparable between the two materials. To manufacture a type-I heterostructure CdS was chosen as the shell component. The growth of CdSe/CdS nanocrystals and

nanoplatelets via the *c*-ALD approach has been introduced by Ithurria and Talapin.^[15] The delicate colloidal stability of nanowires as well as the polytypism, represent a challenge when applying the *c*-ALD method to these highly anisotropic nanostructures. However, CdSe/CdS core/shell NWs were successfully synthesized by Sara Grunewald using the sequential phase transfer of the *c*-ALD approach. The steady-state absorption spectrum of the CdSe/*x*CdS NWs (Figure 5.12a) can give an estimate about the diameter after each *c*-ALD cycle *x* as well as side nucleation. Two extinction peaks at 695 nm and 565 nm are clearly discernible in the spectrum and the respective first derivative of the CdSe core NWs. The position of the first excitonic transition remains steady throughout the series, indicating that the confinement of the NWs has not been altered. However, the exciton Bohr radius of CdSe is reported to be 5.6 nm^[162], which is well below the diameter of the CdSe core NWs.

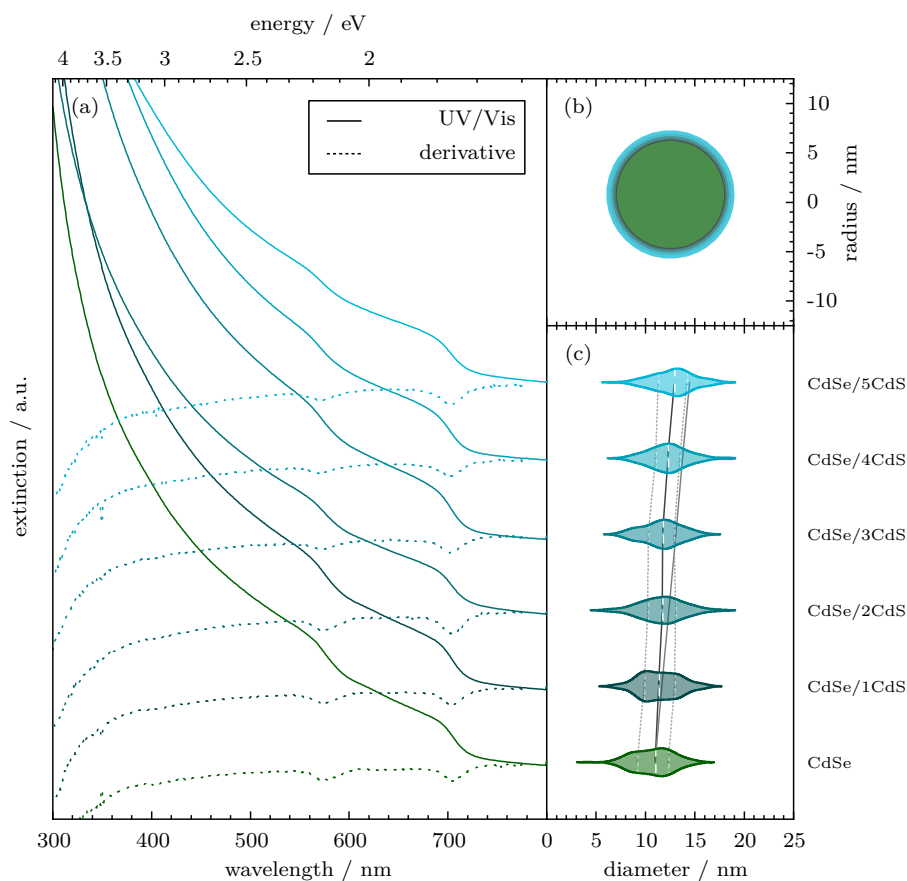


Figure 5.12: Absorption and size distribution of CdSe/*x*CdS NWs. Steady-state absorption spectra normalized to the first excitonic transition and the corresponding first derivative (dashed) of the core/shell NWs (a). The proportions of the core structure and the successive MLs are sketched for comparison (b). The size distribution of the CdSe/*x*CdS NWs after each *c*-ALD cycle *x* is represented with violin plots (c) with the 25th and 75th percentile (dashed), the experimental median diameter d_{ex} (black) and theoretical diameter d_{th} (gray).

Consequently, the additional width introduced by the shell would not induce a significant delocalization of the wave function. The lack of an additional absorption peak implies that no side-nucleated NPs remain in the dispersion after purification. Furthermore, the direct excitation of the CdS shell and an incidental absorption peak around 500 nm could not be observed. When contemplating the geometry of the heterostructure as schematically depicted in Figure 5.12b, the material ratio of CdS may be insufficient as to evoke a perceptible transition signal in the absorption spectrum.

The violin plots of the CdSe/ x CdS NW samples in Figure 5.12 reveal, that the median diameter of the core/shell NWs did indeed increase successively, despite the stable spectral position of the first absorption maximum. The black line connects the medians of the respective size distributions and serves as a guide to the eye. The increase in median diameter d_{ex} during the first two cycles is smaller than the calculated value (gray line) with an increment of 0.7 nm per CdS ML. No deposition was observed for the third cycle. Shell growth during the final cycles occurred as calculated with the slope of both the median and the theoretical diameter line concurring well. The dashed lines that interconnect the 25th and the 75th percentile of the sequential distributions remain approximately parallel to each other. The two percentiles mark the lower and upper quartile, which comprise the smallest and largest 25% of the data, respectively. The values for the experimental and the theoretical value d_{ex} and d_{th} as well as the differences δ_{25} and δ_{75} between the median and the percentiles are given in Table 5.4. The interquartile range (IQR) remains comparable throughout the c-ALD procedure, indicating a constant diameter increment of all NWs. Therefore, the efficiency of shell deposition is estimated to be independent from the NW diameter. However, a discrepancy between the calculated and the experimental increment has been observed for the first two shell deposition cycles. Furthermore, the distribution of the core NWs is slightly skewed towards larger diameters, while the median diameter of the CdSe/1CdS NWs is close to the mean value. The concurring small decrease of the IQR might be due to an incomplete removal of the original ligands stabilizing the CdSe NWs. Thus, the ligand-stripping during the first half-reaction may be dependent on the NW diameter, whereas the subsequent deposition cycles after the initial exchange are independent of the size of the anorganic material. This has further been validated with a c-ALD series starting from core NWs that exhibit a bimodal size distribution. While a diameter increase was observed for both sub-species, growth of the smaller core/shell NWs was more inhomogeneous.^[163]

Table 5.4: Increment of NW diameter d per c-ALD cycle x .

x	d_{ex}	$\frac{\delta_{25}}{\delta_{75}}$	d_{th}
/ nm			
-	10.97	$\frac{-1.83}{1.31}$	-
1	11.31	$\frac{-1.45}{1.62}$	11.67
2	11.69	$\frac{-1.47}{1.37}$	12.37
3	11.72	$\frac{-1.47}{1.17}$	13.07
4	12.26	$\frac{-1.24}{1.20}$	13.77
5	12.88	$\frac{-1.60}{1.28}$	14.47

To analyze the impact of the mere diameter increase of the anorganic material on the optical properties without contemplating the effect of the heterostructure, CdSe core NWs having different diameters were compared. The steady-state extinction (solid lines) normalized to the first absorption edge and the corresponding normalized PL spectra (dashed) are shown in Figure 5.13 for CdSe_{11.0}, CdSe_{18.2} and CdSe_{28.4} NWs. The PL spectra were obtained in a confocal setup on a single particle level. It has to be noted, that the spectra of individual NWs can vary strongly due to the polydispersity of the investigated samples. Furthermore, the PL characteristics have been found to depend on the measurement location on the investigated anisotropic structure. Thus, interparticle as well as intraparticle deviations have to be considered. While detailed investigations of these single-particle effects are important as to probe the origin of trap states, they are not expedient when contemplating the general spectral evolution of these NW samples. In order to reduce the influence of both inter- and intrawire variations, the PL spectra were collected at different positions of a single structure as well as on different wires. The individual spectra were normalized and a mean quasi-ensemble PL spectrum was subsequently retrieved. Although the CdSe NW samples cover a large diameter range, no significant changes in the optical data can be observed. The constant spectral position of the quasi-ensemble PL peaks suggests, that even the smallest CdSe_{11.0} NWs do not exhibit confinement effects, which is in line with an exciton Bohr radius of 5.6 nm. Consequently, no pronounced bathochromic shift of the PL maximum with the successive addition of CdS MLs that could be induced by the lifting of confinement conditions is expected.

The consecutive PL spectra (solid lines) and the corresponding extinction data (dashed lines) of the CdSe/*x*CdS NWs are shown in the waterfall diagram in Figure 5.14a. As assumed, the changes in spectral position of the PL maximum are minimal. For a more detailed analysis, the emission wavelength and the FWHM have been retrieved and plotted with respect to the CdSe/*x*CdS diameter in Figure 5.14b. The PL maxima (circles) and the FWHM (squares) exhibit opposing trends. Contrary to the preliminary assumption of a bathochromic change of the emission maximum, a small hypsochromic shift was detected. The disrupted diameter increase between *c*-ALD cycles two and three has been observed to result in a slight shift back to a longer emission wavelength and a concomitant increase of the FWHM. However, this shift is insignificant compared to the mean blue shift induced by a successful addition of a ML.

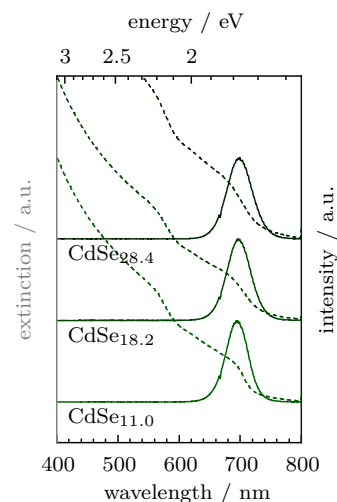


Figure 5.13: Influence of CdSe NW diameter. UV-Vis (dashed) and PL (solid) spectra of CdSe NWs having diameters of 11.0 nm (bottom), 18.2 nm (center) and 28.4 nm (top). The extinction spectra are normalized to the first transition.

Even more prominent than the discussed discontinuity are the values retrieved for the two final cycles as the largest FWHM of the series occurs in cycle four together with the largest shift of the emission wavelength to higher energies. Contemplating the shape of the violin plots representing the size distributions, the final sample seems to contain a fraction of smaller NWs than even cycle one. Although a multitude of NWs was used to evaluate both the geometric and the optical properties and the aliquots were taken directly after re-dispersion, these findings are strongly influenced by the colloidal stability of the nanostructures, which decreases with increasing c-ALD cycle. Especially the final cycle has been reported as having been complicated to conduct due to the increased agglomeration and insufficient phase transfer.^[163] Additionally, the values retrieved for the optical properties of the CdSe/5CdS NWs have to be interpreted cautiously as no individual one-dimensional structures have been found in the confocal PL scan, despite them being clearly visible in the TEM.

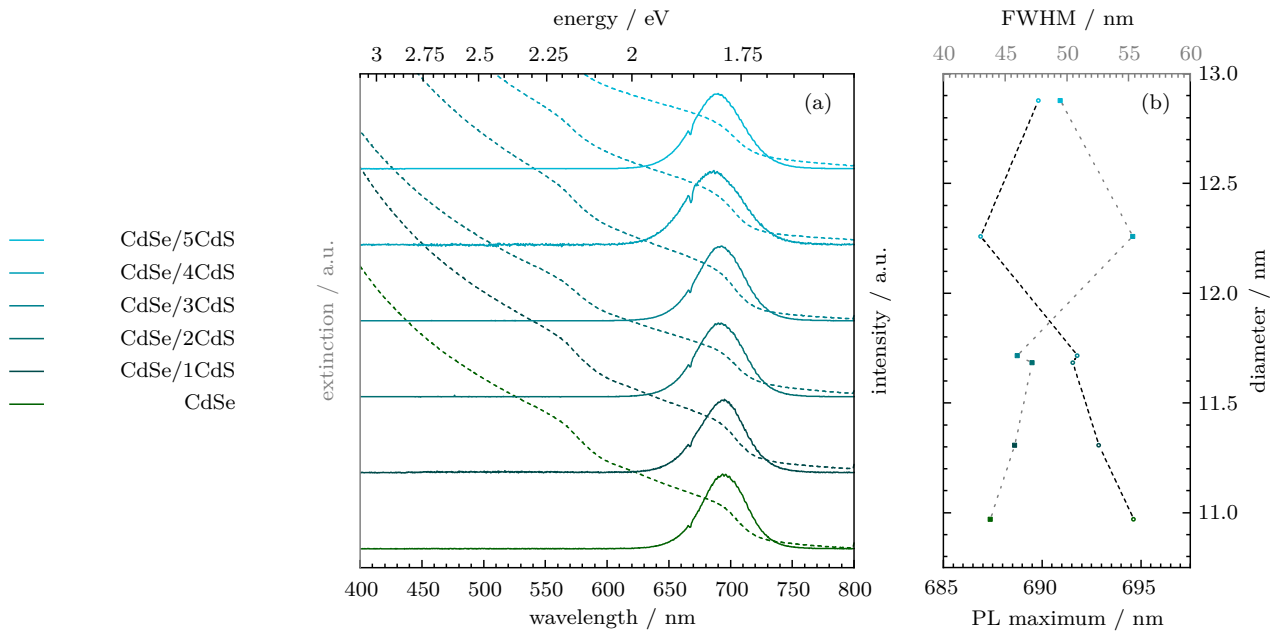


Figure 5.14: Emission wavelength of CdSe/*x*CdS NWs. From the normalized quasi-ensemble PL spectra (a) the peak wavelength and FWHM were retrieved and plotted versus the core/shell NW diameter (b).

Nonetheless, general trends for both the PL maxima and the FWHM can be observed, which seem to correlate with the evolution of the size distribution for the respective c-ALD cycles. The slight changes of the optical characteristics may be attributed to a change in dielectricum surrounding the semiconductor resulting from the anorganic LER rather than a lifting of confinement conditions.

It was reported, that the *c*-ALD grown core/shell NWs are structurally unstable and degrade over time, while the original core NWs are stable over long periods of time. Since the initial ligands are removed during the process, colloidal stability may suffer during the *c*-ALD procedure. Furthermore, residues of the reducing agent FA may disintegrate the anorganic material.^[163] The phase transfer of the colloidal NWs and consequently the LER utilized for the shell deposition was found to be increasingly unreliable with decreasing diameter of the core NWs, which is why non-quantized CdSe parent NWs were used for this study.

The deposition of a shell on quantized NWs using a single-source precursor has been demonstrated before. The preliminary shell consisting of nanorods was subjected to a ripening process to ultimately form a smoother coating. However, the morphology of the obtained heterostructures differs strongly from the *c*-ALD grown shells.^[164] The core/shell structures synthesized via the self-limiting *c*-ALD method and the calculation-based rod nucleation approach are shown in Figure 5.15. The homogeneous shell obtained through the epitaxial growth facilitated through *c*-ALD (a) presents a stark contrast to the nanostructured shell that has formed after ripening for 4 h (b₁) and 24 h (b₂) of the nanorods that originally nucleated at the parent NWs during the latter approach. The typical polytypism of SLS-grown cadmium chalcogenide NWs has been reported to induce nucleation centers on the NW surface, which have been exploited for shell formation via the rod nucleation mechanism. The ripening process has been found to successively convert the elongated shell particles into thermodynamically more stable spherical particles. Through diffusion along the core NW, intrarod material transport and reshaping occurs until bead-like structures have formed along the NW. Although these exhibit the same crystal phase and orientation as the template, the final shell has strong variations in diameter. In addition to the inhomogeneous shell morphology, the amount of precursor needed for an aspired shell thickness has to be estimated in analogy to the calculations conducted for the SILAR method.^[164]

This estimation however is especially error-prone when pertaining to colloidal NWs as both NW concentration and length can not be readily determined, which in turn renders the calculated surface area highly inaccurate. Auxiliary, side nucleation in solution, which is subjective to several parameters such as the ligand system, solvent and temperature fluctuations may significantly reduce the amount of available precursor and thus reduce the thickness of the shell. Finally, the phase alternations in the NWs may contribute to the imprecision of the calculation-based process,

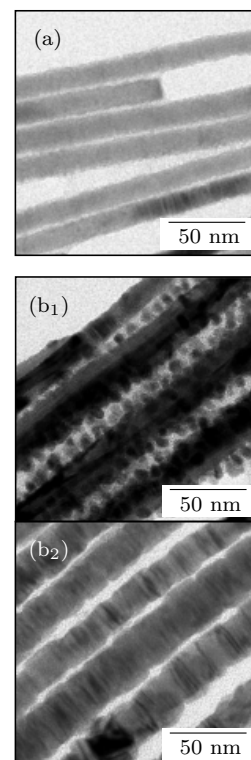


Figure 5.15: Micrographs of CdSe/CdS core/shell NWs. The shells were deposited using different mechanisms. The NWs that exhibit a smooth shell (a) were fabricated using the *c*-ALD approach. The NWs produced via rod nucleation after ripening for 4h (b₁) and 24h (b₂) as published by Li et al.^[164] are shown for comparison.

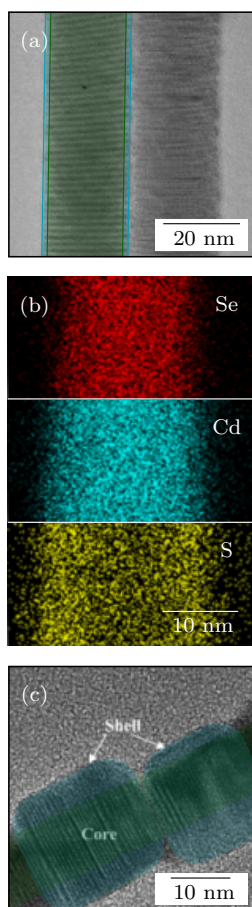


Figure 5.16: High-resolution micrographs of core/shell NWs. TEM analysis of a CdSe/4CdS heterowire synthesized via the c-ALD approach (a). The region of the CdSe core (green) and the CdS shell (light blue) are highlighted exemplarily for one NW. An additional EDX mapping reveals the spatial distribution of the semiconductor compounds (c). The HR image of the core/shell wire grown via the rod-nucleation technique has been adapted from Li et al.^[164] to include highlights for the core (green) and the shell (light blue).

as the nucleation of the nanorods has been reported to primarily occur on the (111) equivalent faces of ZB segments.^[164,165] Variation in ZB/WZ ratio and especially segment length and phase-alternation frequency resulting from slightly different synthesis conditions may thus influence the number of nucleation sites and consequently, the nanorod density during shell growth. Naturally, the core NWs used for the c-ALD technique also exhibit polytypism, as they have been synthesized using the same SLS-approach with similar conditions. However, no effect on the shell deposition beyond templating of the crystal structure and orientation has been observed for this anorganic LER even in the HRTEM that is reproduced in Figure 5.16a. For better visualization, core and shell regions are highlighted in green and light blue, respectively. No pronounced distortions or interruptencies have been observed which is in contrast to the HRTEM image of the rod-nucleated core/shell NWs displayed in Figure 5.16c that was adapted from ref^[164] to include the same color code as in (a) to highlight core and shell material, although clearly discernible in this case. As previously discussed, nucleation of the nanorods as an intermediate shell system is occurring at the ZB-phase surface. Extended WZ segments may thus lead to sections that have to be coated solely via surface diffusion.

The quality of the shell deposition is also limited by the slight lattice mismatch between CdSe and CdS of 3.86% (WZ) and 3.95% (ZB), which can not be compensated without distortions over longer distances. Although the same lattice constraints do apply to the shell growth using c-ALD, all lattice spaces are readily accessible through the ligand exchange associated with the phase-transfer. Therefore, a growth mechanism similar to the classical layer-by-layer growth may be assumed to occur during this heteroepitaxy. The transition from layer-by-layer (Frank–van der Merwe) to island-based (Volmer–Weber) growth, which form the basis of the intermediary Stranski–Krastanov mechanism, is governed by the chemical potential of the deposited layers. At a critical thickness, the accumulated strain energy surpasses the tolerable wetting-misfit, concomitant with the introduction of dislocations and ultimately the formation of islands.^[166] While the wetting layer can include several monolayers of the shell material at small lattice mismatches, one has to keep in mind that these deposition mechanisms pertain to flat two-dimensional substrates rather than the one-dimensional NWs, which exhibit additional strain along the waist of the structure. Consequently, strain release would have to be highly anisotropic, which may hinder the formation of islands as the increased surface energy in comparison to the classical case cannot be compensated.

Finally, charge-neutrality has to be maintained during each half-reaction of the c-ALD process, which renders the adsorption of additional ions unlikely. These limitations together with the decrease in colloidal stability probably hinder the successful deposition of an additional ML of shell material in case of the CdSe/CdS NWs used for this study. To verify, that a shell had indeed been deposited, although hardly distinguishable in the HRTEM (Figure 5.16a), an EDX analysis was conducted. The comparison between the chalcogenide channels, denoted Se (red) and S (yellow), in Figure 5.16b ratifies the presence of a heterostructure comprising a CdSe core and a CdS shell, as the latter extends further in the radial direction (horizontal). Furthermore, the Se channel has a higher intensity in the center of the NW than at the edges, which is in agreement with the projection of the spatial distribution of the material in a cylinder. The same applies to the distribution of the metal, only with a larger diameter due to Cd (blue) being the cationic species in both heterostructure compounds. For anion S on the other hand, the regions of highest intensity can be found right at the edges of the structure, which is caused by the tube-like geometry of the shell.

To evaluate the morphology of the heterostructure and get an estimate about the prevalent crystal structure, p-XRD data was collected. Note, that different samples than previously discussed were used as to have sufficient material for the measurement. Nonetheless should they represent the general structural characteristics well as they have been synthesized under the same conditions. The diffractograms of the core CdSe NWs (green) and the core/shell CdSe/4CdS NWs (light blue) are displayed in the center panel of Figure 5.17a. The stick patterns of CdSe (top) and CdS (bottom) are displayed for both crystallographic configurations, namely WZ (blue) and ZB (gray), respectively. The CdSe reference patterns reveal, that the core NWs do indeed exhibit polytypism with WZ being the main crystal phase as was discussed previously. The ratio of WZ/ZB segments could be approximately determined by utilizing the simulations done by Harder et al. that revealed the relative intensity of the WZ(103) reflex as a measure for the ZB-rate under the constraint of analyzing WZ-rich NWs.^[88] Contemplating the ratio of the WZ(103)/WZ(110) peaks as proposed in the reference, a ZB-rate of 17% could be retrieved. A more detailed analysis of the parent NWs however, would probably be more beneficial for a deeper insight into the rod-nucleation mechanism, while the crystal structure of the c-ALD grown shell seems to be templated at each half-reaction and should thus be preserved.

Table 5.5: Reference X-ray diffraction reflexes of CdSe and CdS for WZ (top) and ZB (bottom) crystal phase, respectively.

Miller index	CdSe $q / \text{\AA}^{-1}$	CdS $q / \text{\AA}^{-1}$
(100)	1.69	1.77
(002)	1.79	1.88
(101)	1.91	2.00
(102)	2.46	2.56
(110)	2.92	3.04
(103)	3.17	3.31
(112)	3.43	3.57
(201)	3.49	3.65
(111)	1.79	1.87
(220)	2.92	3.05
(311)	3.43	3.59

Using the same approach for a preliminary analysis of the final core/shell sample, this assumption can be fortified as the ZB-rate appears to be of similar extend with 15% and 22% when using the curves for pure CdSe and CdS, respectively. The core material has been found to amount to 71% of the solid, which when presuming a linear dependency of the intensity ratio on the CdS/CdSe ratio would ultimately render a ZB-rate of 18% for the core/shell structure. In addition to differences in WZ(103)/WZ(110) ratio between CdSe and CdS species, does the smaller ion radius of S cause a shift of the XRD reflexes to higher values of wavevector q as is also listed in Table 5.5. However, these shifts are only observable for some reflexes, which is related to the orientation of the lattice planes within the heterostructure. The vectors representing the normals of the relevant planes in a wz-NW (blue) and a zb-NW (gray) are illustrated in (b₁) and (b₂). In case of these highly anisotropic heterostructures, those reflexes with longitudinal and those with radial contributions have to be discriminated. This already applies to the parent structure due to the strikingly different number of planes along and perpendicular to the growth direction of the NW, leading to differences in coherence length, which in turn influences the width of the corresponding peak.

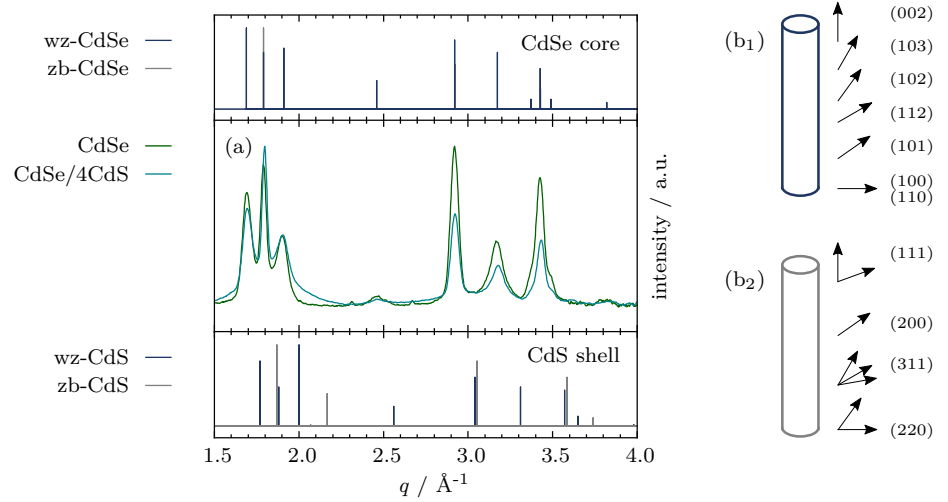


Figure 5.17: XRD of CdSe/ x CdS NWs. Powder diffractograms of core CdSe NWs (green) and core/shell CdSe/4CdS NWs (light blue) are shown in the center panel to estimate the effect of the epitaxially deposited shell (a). The stick patterns of wz-CdSe (PDF-no. 00-008-0459, top, blue) and zb-CdSe (PDF-no. 00-019-0191, top, gray) as well as those of wz-CdS (PDF-no. 00-001-0780, bottom, blue) and zb-CdS (PDF-no. 00-010-0454, bottom, gray) are shown for comparison. The respective miller indices can be retrieved from Table 5.5. The orientations of the lattice-plane normals of WZ (b₁, blue) and ZB (gray, b₂) with respect to the NW are illustrated for clarification.

The coinciding longitudinal reflexes WZ(002) and ZB(111) of the core NWs have been observed to concur with those of the core/shell NWs, although the extensive coherence length along the NW should allow for a significant variation. The lack of this shift supports the hypothesis, that the shell atoms are situated at their templated position rather than what the unstrained crystal structure would imply. However, these peaks are mainly influenced by the phase alternations. The FWHM of the predominantly radial reflexes WZ(100) and WZ(110)/ZB(220) can be used as a measure for the NW diameter, which do suggest a small increase in diameter. In addition to this response, a slight shift would also be expected in first approximation, as the lattice of the adsorbant should be relaxed in the direction perpendicular to the surface. This on the other hand, only applies to epitaxial growth on a two-dimensional substrate. In this specific case, the shell material exhibits even a smaller lattice constant than the cylindrical core material. Furthermore, only four MLs on each side of the projection through these lattice planes contribute to the signal. The main effect on the diffractogram probably originates from strain effects due to compression of the core lattice and deformation of the shell lattice. The WZ(103) reflex, which is also used to determine the ZB-rate, may exhibit the most pronounced variations in both wavevector and shape, as its trajectory includes more than the aforementioned four planes of shell material.

The p-XRD of the core/shell NWs exhibits an almost negligible shift to larger wavevectors, as the lattice spacing of the adsorbant is presumably dictated by the one-dimensional substrate. The shell has thus probably been grown in a highly strained fashion in the absence of additional ions, which could possibly promote relaxation. The hypsochromic shift of the PL highlighted in Figure 5.14 may thus also be a result of the increasing compression and strain within the core/shell nanostructure. To analyze both the spectral characteristics and the morphological effects of the c-ALD growth further, homoepitaxial systems such as CdSe/CdSe or CdS/CdS may be suitable to mitigate strain contributions originating from the lattice mismatch. It would further be interesting to not only analyze the subsequential intact heterostructures that are coated with a complete ML of the shell semiconductor, but also characterize the optical properties after the half-reactions. The c-ALD process was conducted assuming a Cd-rich native NW surface, which is why the anionic species was chosen for the initial ligand-exchange step. Here, it would probably contribute to the understanding of the surface chemistry of SLS-grown NWs to also use the cation as the first anorganic ligand.

Table 5.6: Lifetime parameters of CdSe/*x*CdS NWs per c-ALD cycle *x*. The average lifetime τ_{av} as well as the individual lifetimes τ_1 and τ_2 (in ns) and their corresponding fractional contributions f_1 and f_2 are listed as obtained using a bi-exponential fit.

<i>x</i>	τ_{av}	$\frac{\tau_1}{f_1}$	$\frac{\tau_2}{f_2}$
0	6.25	0.60	7.00
		0.562	0.363
1	1.02	0.63	5.66
		0.740	0.007
2	0.94	0.59	3.48
		0.601	0.014
3	1.02	0.59	4.75
		0.704	0.010
4	1.10	0.59	7.02
		0.694	0.005
5	1.31	0.62	5.26
		0.829	0.017

The growth of an anorganic shell around a semiconducting nanostructure is a common means to tailor the charge-carrier confinement and thus, the effective bandgap of the material. A further benefit is the saturation of surface defects, which also has an impact on the PL decay dynamics. Here, the former can be neglected, as the parent NWs have sufficiently large diameters and do not exhibit confinement effects, while the latter is potentially subject to strong variations due to the c-ALD procedure. Therefore, fluorescence decay curves were collected for each CdSe/*x*CdS sample and plotted on a semi-logarithmic scale in Figure 5.18a using the established color code.

The decay curves were approximated with a bi-exponential function using the Levenberg–Marquardt algorithm, revealing lifetime components around 0.6 ns and 5 ns. The faster component τ_1 is on the timescale of the IRF and should thus not be contemplated in detail when analyzing variations in kinetics associated with shell growth. However, this applies to the absolute values, but not to the percentage, as the possible additional recombination processes could contribute significantly to the fast component, although the specific decay time is not procurable. Consequently, the average lifetime, which is calculated using Equation 2.10 can render an insight into the overall changes in dynamics within the limits of resolution. In fact, the core CdSe species exhibits the longest average lifetime τ_{av} as is specified in Table 5.6. In the absence of any additional shell material, the slower component τ_2 enhances the overall lifetime of the system as the amplitudes at t_0 , A_1 and A_2 , are in the same order of magnitude in case of the parent CdSe NWs.

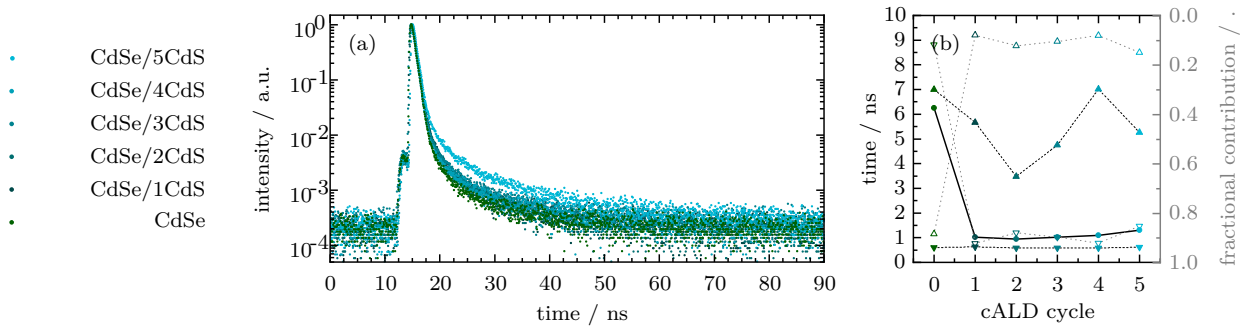


Figure 5.18: PL decay curves of CdSe/*x*CdS NWs. The established color scheme is used to discriminate the data sets. The PL decay curves (a) were fitted bi-exponentially, which rendered the lifetime values τ_1 (solid, downwards triangle) and τ_2 (solid, upwards triangle) and the corresponding fractionals f_1 (empty, downwards triangle) and f_2 (empty, upwards triangle) (b). The average lifetime τ_{av} (solid, circle) was calculated using Equation 2.10.

While a preliminary assumption includes lifetime enhancement due to improved saturation of dangling bonds, this hypothesis does not hold true for the initial shell-growth step that equals an anorganic ligand-exchange reaction. A stark decrease in average lifetime (solid circles) was observed for said CdSe/1CdS sample as is visualized in Figure 5.18b. The solid black line serves as a guide to the eye and emphasizes the evolution of the average lifetime with the increment of shell monolayers. Likewise, the trends of the individual lifetime components τ_1 (solid, downwards triangle) and τ_2 (solid, upwards triangle) are accentuated by black dotted lines. The gray dashed lines highlight the corresponding fractional contributions f_1 (empty, downwards triangle) and f_2 (empty, upwards triangle). Note, that the dedicated ordinate (gray) is inverted to improve lucidity of the subfigure. It becomes apparent, that the reduced average lifetime of the core/shell NWs is governed by the stark decrease in f_2 , which reaches a plateau at low fractional contribution, while f_1 complements the lifetime distribution at high fractional contribution. For the calculation of these fractionals, Equation 5.1 was used. The subsequent addition of shell monolayers results in a slight increase of the average lifetime, which may be attributed to the enhanced screening of the dielectricum at thicker shell conditions or the retroactive saturation of defects remaining from the preceding deposition.

$$f_i = \frac{A_i \tau_i}{\sum_i A_i \tau_i} \quad (5.1)$$

The success of the exchange from organic to inorganic ligands is influenced by the initial stripping of the original surfactants, namely the phosphonic acids, using the salt $(\text{NH}_4)_2\text{S}$. The colloidal stability of the NWs, especially in the intermediate polar phase, and the phase transfer into the unpolar phase using the long-chained organic molecule DDAB, further govern the outcome of the first half-reaction of the LER procedure. If the correct prerequisites are met inadequately, e. g. the concentration of the inorganic ligand is spuriously high, the exchange could be expedited beyond the usually concurrent phase transfer, resulting in the coagulation of the NWs. Likewise, an insufficient concentration will probably result in an incomplete ligand exchange and consequently an incomprehensive sulfide layer on the one hand, while the phase transfer will most likely also be impeded, due to some of the original organic molecules remaining on the surface.

To be able to compare not only the spectral position and the decay kinetics, but also the absolute intensities of the native CdSe NWs and the core/shell NWs, both species were deposited on the same substrate. The position of the NWs on the substrate was mapped after each deposition step in order to discriminate core and core/shell NWs. In preparation, an investigation of CdSe and CdS NWs was conducted as proof of principle, since the two materials can be distinguished easily, due to their pronounced emission maxima. A spectrally resolved map of an area containing both species was obtained by raster scanning the excitation beam while collecting a spectrum for each pixel. The individual spectra were subsequently fitted with a Gaussian as to evaluate the respective emission maximum. A 2D-map illustrating the spatial distribution of the retrieved PL peak wavelengths is provided in Figure 5.19a₁. To obviate fitting of the background signal, a threshold was implemented. Pixels with an insignificant signal were elided during the fitting procedure.

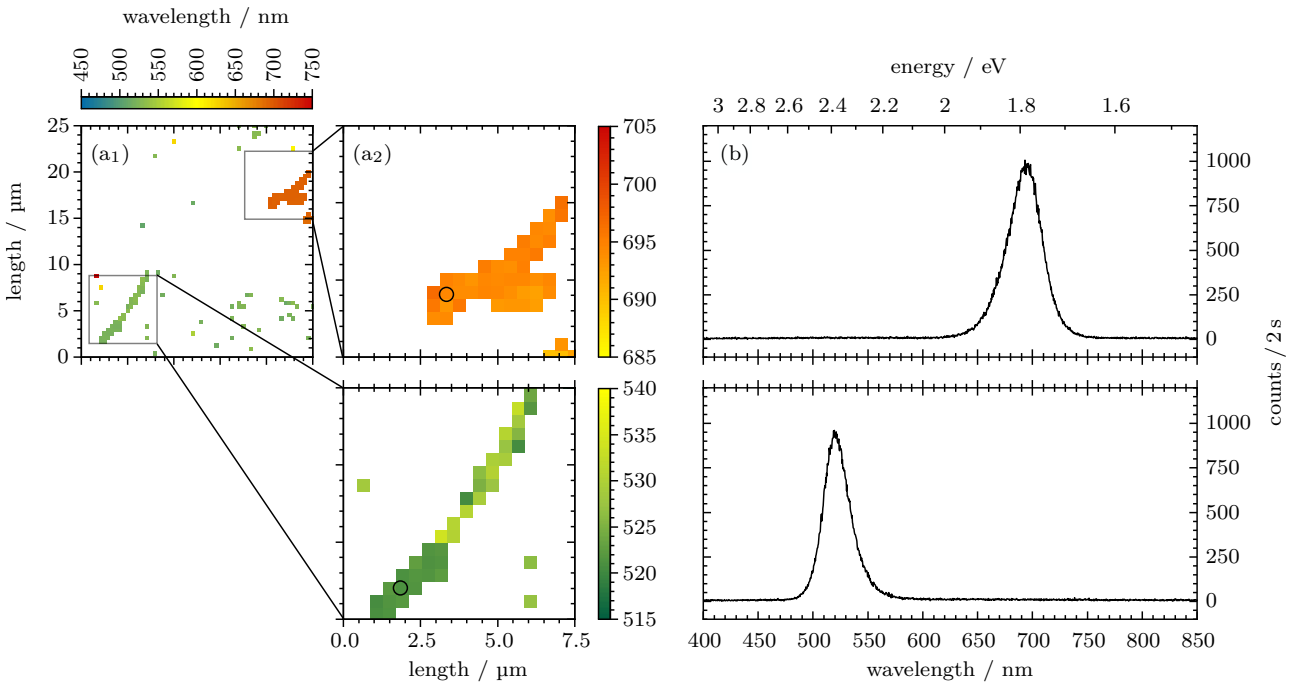


Figure 5.19: Spectrally resolved map of CdSe and CdS NWs. The spatial distribution of the PL maxima of both species (a₁) and the maps showing the emission wavelengths of CdSe (a₂, top) and CdS (a₂, bottom) individually, reveal PL-maxima modulations along the NWs. Exemplary spectra of CdSe (top) and CdS (bottom) were extracted from the pixels highlighted in the 2D-data (b).

The remaining pixels can largely be assigned to either CdSe (reddish) or CdS (greenish) NWs. The sporadic pixels, which do not exhibit any conjunction to a nanostructure, most likely result from the delicate choice of the count threshold level. While these contributions of the background

could be rejected reliably, the partially weak signal of the NW would also be discarded. For a more detailed investigation, the CdSe and CdS NWs are represented in separate channels (a_2). Fluctuations of the peak wavelength with respect to the intrawire position are perceptible. This effect is especially pronounced for the CdS NW (bottom). The ends of the one-dimensional structure exhibit a smaller peak wavelength than the middle part. The exemplary spectra (Figure 5.19b) retrieved from individual pixels at the NW tips of both CdSe and CdS compare well with the effective band energy reported for the respective bulk material. Consequently, the red-shift of the peak wavelength at the CdSe NW center should not be induced by the lifting of confinement due to an increase of NW diameter.

As colloiddally synthesized NWs are prone to agglomerate and form bundles, not only the emission wavelength but also the intensity should be contemplated. The correlation of both may give an insight into the arrangement of individual NWs within the investigated bundle. For comparison, 2D-maps representing the spatial distribution of the peak wavelengths and intensities are shown in Figures 5.20a and b, respectively.

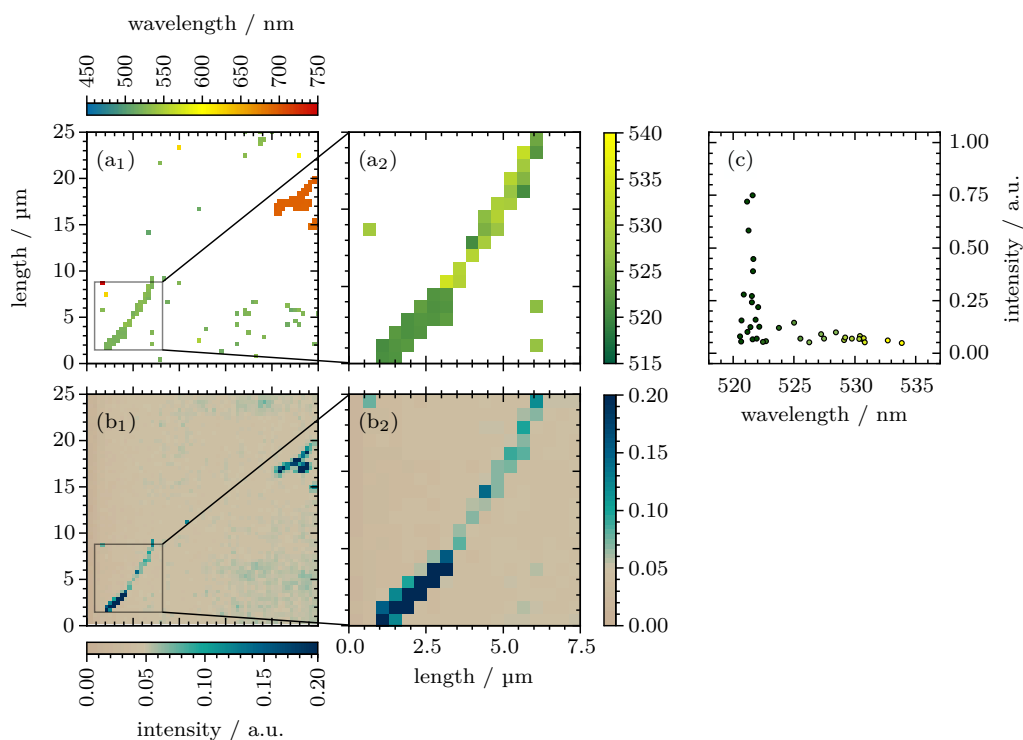


Figure 5.20: Correlation of PL wavelength and intensity of CdS NWs. The spatial distribution of the PL wavelength within the whole scan area (a_1) and an excerpt representing the CdS structure (a_2) is compared to the PL intensity distribution (b) within the same spatial region. The values extracted at identical positions are subsequently correlated (c).

The aforementioned insular pixels, which are visible in the spectrally resolved map (a₁), can also be distinguished in the intensity map (b₁). The diffuse shape of the signal strongly suggests, that the counts originate from a background evoked by some kind of residue on the substrate. The correlation of the emission wavelength and intensity of the CdS NW represented in the excerpt reveals, that the middle section of the one-dimensional structure is of lesser intensity at higher emission wavelength. The ends of the structure on the other hand partially exhibit much higher intensities, but luminesce at shorter wavelengths. One possible explanation may simply be the smaller relative contribution of the background to the overall emission at pixels with higher intensities.

While the proof-of-principle investigation using the two different material systems worked perfectly, no distinct differences between CdSe and CdSe/1CdS could be observed, although the two species were registered successfully after the respective deposition step. No PL-intensity enhancement due to the shell was noticeable upon direct comparison. Consequently, a similar procedure as the heat treatment using the TGA setup was conducted, in order to promote the rearrangement of the atoms within the crystal lattice and thus suppress defects through annealing. Contrary to the experience reported for the CdTe NWs, the emission of the respective species remained intact. However, not only could the PL be preserved, but no significant intensity variation of the core/shell sample with respect to the parent structures was observed. Instead, an increase in the structure/substrate intensity ratio was observed for all NW species. This can probably be attributed to the inactivation of the luminescent residues that were discussed before.

In future experiments, the annealing procedures should be repeated using different experimental parameters. Moreover, samples with thicker shells may be of higher interest than the single-monolayer sample, although on the other hand, the rearrangement of only a single monolayer is probably more facile. A slightly different approach to the annealing investigation might be conducted by monitoring the morphology of the NWs in a TEM while using a heating mount as to directly monitor the influence of the procedure on the crystal lattice. On that note, strain-mapping could contribute to the suite of methodologies and may render insights into the compression of the core NW caused by the small lattice mismatch between core and shell material.

Furthermore, the effects of a c-ALD-mediated shell on core NWs exhibiting confinement should be investigated. In that case, two competing effects on the lifetime characteristics of the core/shell system might be evoked. Lifting of confinement may prolong the average lifetime and the imperfect nature of the shell might lead to a reduction of the average lifetime as was discussed above. Instead of producing a radial heterostructure with two different semiconductors, it would further be of interest to deposit a shell of the same material onto a core structure. In this quasi-heterostructure, lattice-mismatch effects should in principle be circumvented. When using CdS as a model system, the intensity of the emission at 700 nm could be used as a measure for newly introduced trap states. Using the c-ALD method to exchange the organic ligands of the CdTe NWs to form a CdTe/ x CdTe sample could be an alternate route to investigate the origin of the NIR-replicas.

An IR-investigation of the subsample species such as CdSe, CdSe/S and CdSe/S/Cd may render insight into the organic remnants used to promote the anorganic LER, although the success of the phase-transfer during the c-ALD already provides feedback about shell-growth. In addition, the optical properties of these subspecies should be analyzed. This has however been challenging to date, as the synthesis needs to be scaled up for these experiments, which has been difficult thus far.

5.3 Influence of the Synthesis Ligand-System on the PL

In the last sections, the influence of organic and inorganic surfactants on the optical characteristics of NWs was discussed. To investigate the effect of the different ligands, while the semiconductor nanostructures remain comparable, the organic matrix was altered only after synthesis. In the following section, the effect of individual ligand species used for complexation during synthesis on the resulting NWs will be discussed. In addition to the surface-ligand interaction, the influence of the organic molecule on the morphology of the nanostructure has to be contemplated. More specifically, the choice of ligand may affect the overall crystal structure and geometry as well as the lattice defect density. The SLS synthesis can be divided into two subphases, namely the pre-nucleation phase and the crystal-growth phase. During the former, the ligands complexate the precursor and thus limit the speed of the reaction. This is due to the size-dependent diffusion speed of the complex and the cleavage efficiency at the solution/liquid interface of the catalyst particle. The subsequent directional crystal growth is further promoted by the preferential adsorption of the coordinating ligands on the side facets. Both the reaction kinetics and the surface passivation play a significant role in the reduction of defect sites and thus, charge-carrier trap states.

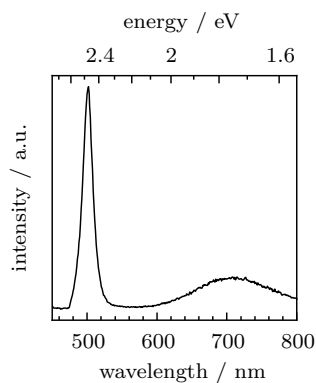


Figure 5.21: A typical spectrum of CdS NWs. The luminescence of CdS at RT usually comprises a narrow NBE signal and a broad trap band.

The wide-band-gap semiconducting CdS NWs are well suited as a model system for the investigation of defects due to their distinct emission spectrum. An exemplary spectrum of CdS NWs is reproduced in Figure 5.21. Auxiliary to the narrow near-band edge (NBE) signal, a broad emission feature can be observed at lower energies. The red-shifted emission band has been reported to originate from trap states.^[167] The reduction of the recombination energy and concomitantly, the photon energy, is ascribed to the interaction of the photo-generated charge-carriers with lattice defects such as vacancies and interstitials. The positively charged sulfur vacancies have been identified as the main defects that contribute to the trap emission. The excess of cadmium ions has been reported to have a similar effect as they increase the number of electron scavengers and thus equal sulfur vacancies.^[168] Unsaturated cadmium surface sites with their dangling bonds may present an analogous case and therefore augment the trap emission. The reduction of lattice defects during synthesis as well as an enhanced surface–ligand interaction may consequently attenuate the defect-mediated recombination.

For the synthesis of cadmium chalcogenide nanostructures, alkyl phosphonic acids (PA) are well established. While the interaction strength of ligand and NW surface was to be modified, the general binding motif should remain unaltered. Variation of the aliphatic residue affects the acidity of the head group and may thus also influence the coordination to the cadmium surface site.^[169] Therefore, the optical characteristics of CdS NWs that have been synthesized from different cadmium precursors, were probed. The diprotic acids used for the preliminary complexation of the cadmium are represented in Figure 5.22. The choice of PA derivatives included octylphosphonic acid (OPA), tetradecylphosphonic acid (TDPA) and octadecylphosphonic acid (ODPA).

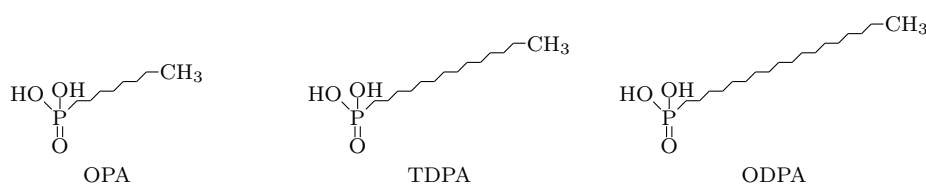


Figure 5.22: Phosphonic acids used for the synthesis of the CdS NWs. The chain length of the aliphatic residue was varied, rendering OPA (left), TDPA (middle) and ODPA (right), respectively.

The binding energy of the surfactants is not only correlated with the binding motif of the head group itself but with the electron-releasing nature of the substituent group, namely the hydrocarbon chain.^[170] The positive inductive effect (+I) of the alkyl chain increases the electron density in the head group, thus decreasing the acidity of the functional group. However, the inductive effect is considered to only be significant over a short distance, rendering even the variation between butyl- and pentyl-residue negligible with respect to the electron-releasing character. Nonetheless, the length of the ligands has been reported to have a pronounced influence on the formation cadmium chalcogenide nanorods.^[85] These findings are attributed to the increased thermal stability and the smaller diffusion coefficient of complexes with longer chains. The shorter chain ligands were thus assumed to be more reactive, ultimately promoting anisotropic growth but also the generation of lattice defects.^[171,172] While these properties mainly apply to conventional colloidal synthesis, including the homogeneous nucleation and subsequent growth of the nanostructures, a similar surmise can be made for the anisotropic growth rate during SLS synthesis, with the too high growth rate of small reactive precursors causing higher defect densities.^[152] In addition to the poorer quality of the final NW, the homogeneous nucleation competes the SLS growth, thus either necessitating the use of an inhibitor or a less reactive precursor.^[78]

As stated above, the extend of the trap emission may not only be influenced by the passivation of the final nanostructure, but also by the morphology that is a direct consequence of the synthesis parameters. The decrease of the NW diameter may contribute to the trap-mediated recombination due to the enhanced surface to volume ratio. The size distributions of the different NW samples were thus investigated. Exemplary TEM images and the corresponding histograms are arranged in Figures 5.23a-b with decreasing residue-chain length from top to bottom.

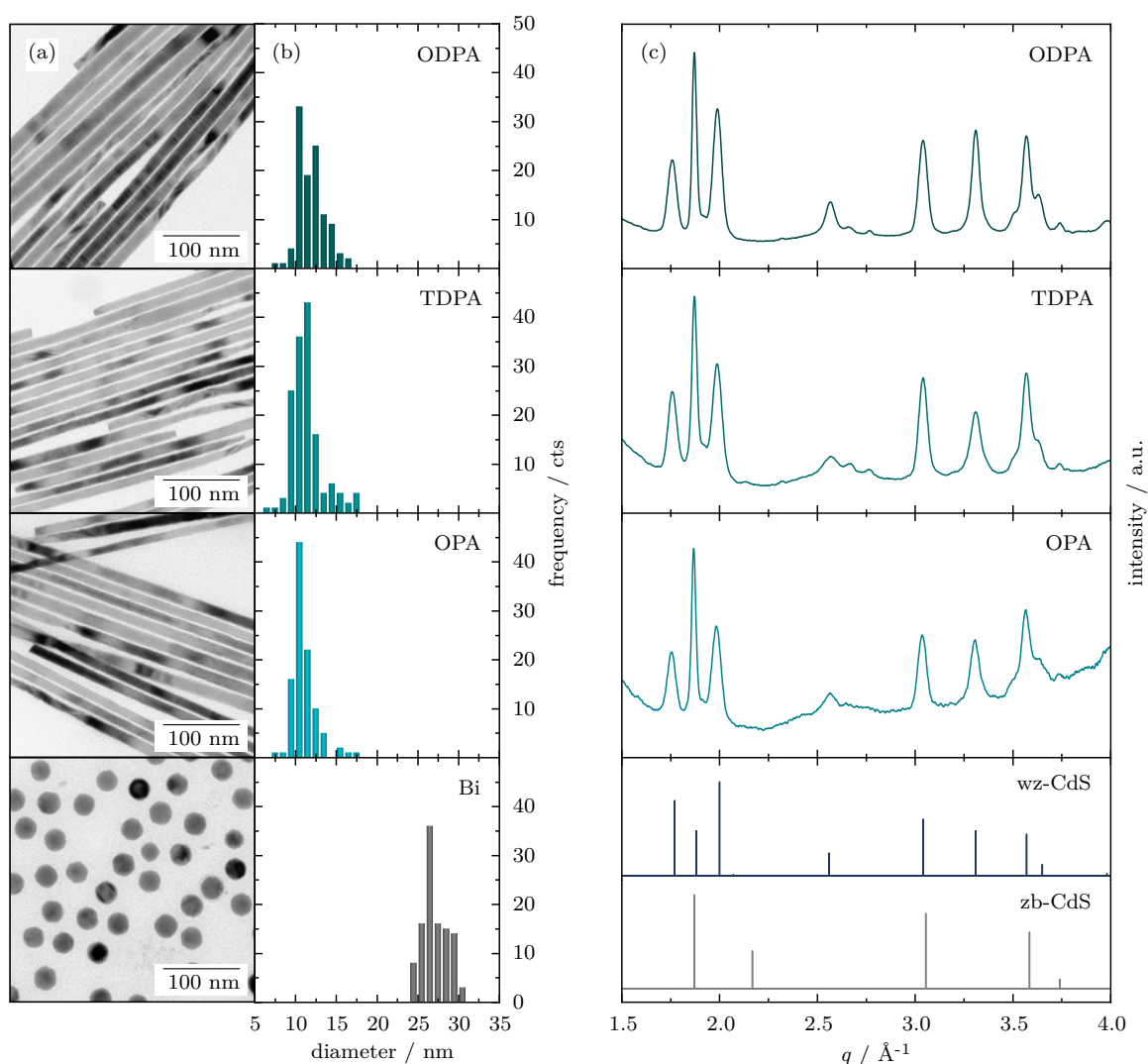


Figure 5.23: PA-dependent structural characteristics of CdS NWs. TEM images (a) and the NW size distributions (b) extracted from the micrographs are shown with decreasing PA chain length from top to bottom, respectively. The diffractograms are reproduced accordingly (c). An electron micrograph and the histogram of the catalyst particles are shown for comparison. The stick patterns of wz-CdS (PDF-no. 00-001-0780) and zb-CdS (PDF-no. 00-010-0454) are given as reference.

In the electron micrographs, straight NWs with homogeneous intrawire diameters are primarily observable. The corresponding diameter histograms do not reveal pronounced differences between the NW samples. The extracted mean diameters amount to $11.9 \text{ nm} \pm 1.7 \text{ nm}$, $11.4 \text{ nm} \pm 1.9 \text{ nm}$ and $11.1 \text{ nm} \pm 1.5 \text{ nm}$ for ODPa, TDPA and OPA, respectively. As previously elaborated, it is assumed, that the small molecules build less stable complexes that are, however, more mobile due to their reduced sterical hindrance. Consequently, the monomer is more readily available and the resulting growth is faster.^[85] For the comparatively short ligand OPA, the growth of CdS nanorods as a competing side process was reported,^[173] which may have been caused by the precursor decomposition of the catalyst NP that is necessary for the subsequent heterogeneous nucleation of the semiconductor in the liquid phase being slower than the homogeneous process in solution. Aside from the side-nucleated nanorods, which could be removed during the purification process, the variation of the PAs did not induce a significant disparity in diameter distributions. This is in line with the assumption that the main effect of the fast supersaturation of the anorganic compounds in the Bi-NP and the concomitant enhanced growth rate is a heightened defect density, while the NW diameter is largely predetermined by the size of the catalyst particle. The transmission electron micrograph and the size histogram of the bismuth catalyst particles ($27.3 \text{ nm} \pm 1.5 \text{ nm}$) are shown for comparison at the bottom of (a) and (b), respectively. A narrow size distribution of the catalyst NP is aspired, to ultimately obtain a sharper diameter distribution of the SLS-grown NWs.

The crystal structure of the three samples was evaluated using the XRD data in Figure 5.23c. As already discussed for the CdTe NWs, SLS-growth promotes the formation of polytypic NWs that comprise WZ and ZB segments. Indeed, reflexes of both crystal phases can be observed in all three diffractograms. The respective stick patterns of the references for wz-CdS (dark blue, PDF-no. 00-001-0780) and zb-CdS (gray, PDF-no. 00-010-0454) are shown below the diffractograms for comparison and additionally listed in Table 5.7. The reflex positions of the experimental data are in good agreement with the stick pattern of the bulk reference of wz-CdS. However, the relative intensity of the reflex at 1.88 \AA^{-1} deviates significantly from the reported value. This is probably caused by an overlap of the aforementioned WZ(002) and the ZB(111) reflexes. While the (200) ZB-reflex is not discernible in any of the experimental diffractograms, the less intense ZB(222) reflex can be observed at 3.74 \AA^{-1} , which further backs the surmise of polytypism. The extensive analysis of the pXRD-data has

Table 5.7: Reference X-ray diffraction reflexes of wz-CdS and zb-CdS.

	Miller index	$q / \text{\AA}^{-1}$
wz-CdS	(100)	1.77
	(002)	1.88
	(101)	2.00
	(102)	2.56
	(110)	3.04
	(103)	3.31
	(112)	3.57
	(201)	3.65
zb-CdS	(111)	1.87
	(200)	2.17
	(220)	3.05
	(311)	3.59
	(222)	3.74

been shown to give a good estimate of the WZ/ZB ratio.^[88] Contemplating the proposed relation between the intensity of the WZ(103) reflex normalized to the WZ(110)/ZB(220) reflex and the ZB-rate reveal values of 7%, 11% and 8% for ODPA, TDPA and OPA, respectively. Although the error of the evaluation method was estimated to be small for low ZB-rates ($\pm 1\%$ at 15%),^[88] the value retrieved for the OPA-terminated NWs may be erroneous due to the pronounced background present in this diffractogram. An influence of the chain length of the PA on the phase-purity of the nanowires can not be confirmed and for the further discussion the WZ-rich NWs are assumed to exhibit polytypism to similar extents.

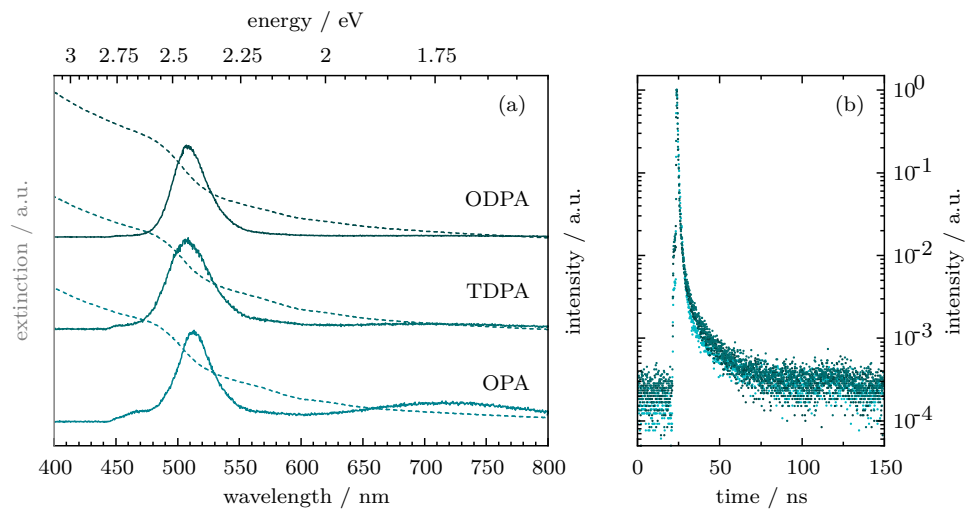


Figure 5.24: Influence of chain length on the spectral properties. UV-Vis (dashed) and PL (solid) spectra of CdS NWs terminated with ODPA (top, green), TDPA (center, turquoise) and OPA (bottom, blue) (a). The extinction spectra are normalized to the inflection point of the first transition. The normalized PL intensity decay curves are represented on a logarithmic scale accordingly.

The chain length of the organic ligand on the optical properties is expected to be limited to a variation of the trap band rather than the NBE. Nonetheless, non-quantized NW samples were chosen for this study as to obviate the convolution of size-quantization effects and surface chemistry influences. The normalized extinction (dashed) and emission spectra (solid) are reproduced in Figure 5.24. The UV-Vis spectra were normalized to the inflection point of the local absorption maximum around 505 nm. The PL spectra of all three samples exhibit a pronounced NBE band at 507 nm (ODPA), 509 nm (TDPA) and 513 nm (OPA) respectively that was used for normalization. The red-shifted trap emission centered at 715 nm is well observable for the OPA-covered sample amounting to an

intensity ratio of 23%. Already for the TDPA-terminated NWs a significant reduction of the trap emission to 7% is observable, while the emission is not discernible for the ODPA-terminated sample. Note, that the extinction spectra are retrieved from colloidal ensemble samples, whereas the emission spectra represent the optical properties on a single particle level. To enhance comparability of the PL data, an area of interest was raster-scanned and the center along a NW (or more likely, a bundle of wires) was selected rather than the end of NWs at which the ligand density is presumably different. The typical detection scheme for individual NPs such as quantum dots is not applicable for NWs due to the lack of clearly discernible on and off states. Nonetheless, the presence of multiple NWs should not affect the surface chemistry and thus, the contribution of shallow trap states to the charge-carrier recombination. In addition to the changes in trap/NBE ratio, an increase in NBE intensity was observed in the presence of the longer ligands. As can be deduced from Figure 5.25, the recombination between the charge-carrier trap states entails not only lower energies than the excitonic recombination, but also different lifetimes and crossover times.^[174]

While the shallow traps contribute to the radiative recombination (wavy arrow) and cause a simultaneous increase of the average PL lifetime, the deep traps that introduce mid-gap energy levels often promote non-radiative relaxation (straight arrow), which nonetheless also contributes to the PL lifetime of the system. For reasons of clarity, only the radiative recombination between shallow electron and hole traps and the radiationless relaxation from a deep electron trap level to shallow hole traps are illustrated, although a multitude of further de-excitation schemes are possible. The different lifetimes τ_e , τ_t can be attributed to excitonic and trap recombination, respectively. The latter can be discriminated further into shallow (st) and deep (dt) trap lifetimes to account for the different kinetics caused by the depth of the defect. Additionally, the crossover times τ_c should be taken into account for the various trap types. Better saturation of the dangling bonds should reduce the number of surface traps and consequently elongate the crossover time τ_c , which results in an increase of the NBE intensity. Electron traps located 0.63–0.7 eV below the CB that are attributed to excess surface Cd have been identified to cause the broad trap emission.^[28] Although these traps lie deep within the band gap with the offset from the band edge by far exceeding the 25 meV that are commonly taken as an estimate to differentiate shallow and deep traps, recombination via these midgap states is radiative and can be observed as the broad emission band.

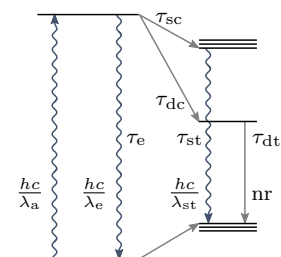


Figure 5.25: Radiative and non-radiative recombination pathways. After the initial absorption of a photon with wavelength λ_a , various recombination paths entailing different lifetimes τ are possible including the relaxation via shallow and deep trap states. Adapted from ref.^[174]

The difference between the observed NBE and trap emission has been determined to range between 0.68 eV–0.71 eV, which is in good agreement with the proposed energetic position of the defect. The energy of the trap-mediated transition appears to be stable, irrespective of the surface ligation and should furthermore be independent of quantization as it is positioned relative to the CB edge and not the electronic levels. Indeed, the trap emission has been found to be of equal width and centered at the same wavelength for all three investigated sample systems.

The deactivation of the surface traps should inhibit this relaxation path and thus increase the intensity of the NBE band and alter the PL lifetime. While an increase in NBE emission was observed with increasing chain length, no pronounced effect on the PL lifetime was retrieved from the decay curves in Figure 5.24(b). The histograms of the PL intensities are represented on a logarithmic scale for a time range of 150 ns and the IRF was measured on each substrate to ensure that it is much faster than the PL response of the nanoscopic semiconductor.

A TGA was conducted to evaluate the thermal stability and the desorption schemes of the different surfactants from the semiconductor surface. The thermogravigrams (colored) and the corresponding derivatives (gray, dashed) in Figure 5.26 reveal a rapid thermal response with degradation peaks observable at 480 °C for CdS/ODPA (top, green), 468 °C for CdS/TDPA (center, turquoise) and 433 °C for CdS/OPA (bottom, blue), respectively. All samples exhibit a plateau until a temperature of 180 °C is reached followed by a slow mass loss of approximately 10% that hints at the same residue being removed in all cases. While water and toluene have boiling points at 100 °C and 111 °C, this initial thermal response may be attributed to the vaporization of organic contaminations introduced during synthesis or purification that could not sufficiently be removed during drying of the samples prior to the TGA. Comparison to the thermogravimetric characteristic of free ligands (such as DOPA and TOPO in Figure 5.9 in Section 5.1.2) reveals, that this slow mass loss can indeed be attributed to the overall sample containing remnants of different solvents and surfactants rather than the pure ligands, which remain intact without any loss of mass until they decompose at a specific temperature.

These characteristic onsets of the thermal response, however, are well distinguishable for the different phosphonic acids. The steep slope of the gravigrams indicates that vaporization of the aliphatic molecules is the prevalent thermal response that, as expected, occurs at lower temperatures for shorter chain lengths. The symmetric shape of the prominent DTG peaks further backs the assumption of a single mechanism evoking the rapid mass loss of around 80% to reach preliminary remaining mass fractions of 7.6% (ODPA), 7.8% (TDPA) and 8.0% (OPA). Especially the TGA curve of the CdS/OPA sample exhibits a further decomposition step starting at 450 °C and resulting in a final residual mass of 1.9%. A similar behavior is noticeable for the CdS/ODPA sample with an onset temperature of 497 °C and a mass of 4.8% for the stable residue. In case of the CdS/TDPA sample, this second decomposition is hardly distinguishable. However, the careful analysis of the gravigram reveals a slight mass loss beyond 486 °C that mark the end of the first step to reach a final stable residual mass of 6.8%. The two observed separate decomposition steps could in theory be attributed to the bidentate nature of the head group.

However, the second process is much less pronounced and may rather be evoked by the actual desorption of the bound ligand while the preceding extensive mass loss is caused by the removal of the free ligands. The comparatively low constant masses at high temperatures indicate that the ratio of organic to inorganic components exceeds the amount of ligand for a perfect surface passivation by far, even if the ligand is assumed to only form one bond with the semiconductor surface. The resemblance of the steep process with the thermal response of the pure ligand further ratifies the hypothesis. and the decomposition of the semiconductor can be omitted as the cause of the second transition as nanoscopic CdS has been reported to be thermally stable in the temperature range covered in the TGA.^[175] Conclusively, the adsorption schemes seem to be similar for the three investigated ligands.

For a more detailed analysis of the thermal stability, it could be beneficial to use CdS nanodots instead of elongated structures in order to avoid the profuse bundling of these colloidal particles and thus reduce the amount of free ligand in the sample. Furthermore, the thermal response could be analyzed using differential thermal analysis (DTA), which renders insight into changes of enthalpy of the system upon heating. Although the obtained TGA data imply a single-step desorption mechanism of the ligand from the semiconductor surface, a subsequently conducted gas chromatography–mass spectrometry (GC–MS) may render valuable information about the nature of the ligand after desorption. The ligands

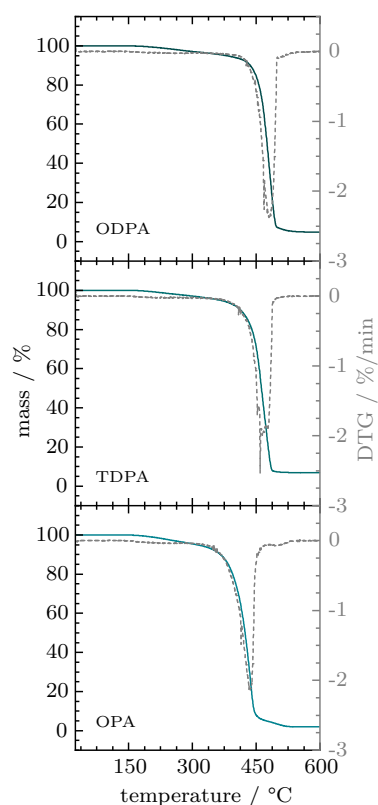


Figure 5.26: Thermogravimetric analysis of the PA-covered CdS NWs. Thermogravigrams (colored) and the respective differentials DTG (gray) of the CdS/ODPA (top, green) CdS/TDPA (center, turquoise) and CdS/OPA (bottom, blue) NWs.

utilized during synthesis were found to have a pronounced influence on the spectral properties of the CdS NWs and especially the trap emission, which is a measure for the passivation of electron traps that result from unsaturated surface sites. While these differences may also be attributed to the morphology of the colloidal nanostructures, TEM and XRD studies revealed the samples to be similar in terms of size distribution and crystal structure. For this initial analysis, non-quantized NW samples were chosen as to preclude the superposition of ligation and quantization effects. It also appears as if the larger diameter contributes to less coagulation and thus a less troublesome sample transfer. In addition to the NW geometry, the length of the ligand also seems to influence the tendency to form bundles, with longer aliphatic chains enhancing this tendency and thus complicating the sample preparation procedure. For future investigations, PL measurements in solution may contribute to a more facile evaluation of the optical properties as ensemble-averaging effects may strongly reduce the bias of the experimenter.

However, single-particle measurements are the ultimate goal as to gain more insight into the influence of the morphology on a nanoscopic level along the wire onto the optical properties. Here it is highly recommended to analyze freshly synthesized samples and deposit them on a TEM substrate supplied with markers for orientation to correlate the spectral characteristics with the position along the NW. Finally, these samples could be submitted to an annealing or ligand-stripping process after an initial round of laser microscopy as to further investigate the influence of the ligands on the optical properties after synthesis. An alternative approach could also be the modification of the surface using cALD to be either sulfur rich or by depositing a complete monolayer and using the method as means for a ligand-exchange reaction.

5.4 X-ray Microscopy Analysis of SLS-QNWs

The optical properties of cadmium chalcogenide NWs are strongly dependent on the organic-capping agents used during colloidal synthesis, as has been discussed in the previous sections. However, insight in not only the optical but also the electrical characteristics is essential for the optimization of NW based applications. By combining the analysis of the elemental distribution and the electrical response of the device by means of XRF and XBIC, local variations in device performance may be correlated to the structural inhomogeneities.

In preparation of the electrical measurements, the substrate with the contacted CdTe NWs was attached to a PCB and electrical contact between the conductive tracks of the PCB and the gold pads of the device was established via copper wire bonds. The construction was fixed to sample holder, which in turn was mounted on an aluminum base. By use of this configuration (Figure 5.27a), sample changes at the beamline are rendered more facile and a more robust direct connection to coaxial cables can be implemented via the plugs.^[129] The KLayout Editor mask defining the electrical architecture (b_1) was designed to comprise two separate sample areas (black boxes) from within which suitable nanostructures were selected to be lithographically contacted. The microscopic gold (yellow) structures and the nanoscopic platinum (red) markers were fabricated prior to NW deposition. In addition to the electronically relevant gold components, triangular markers were included between the two sample areas to ease the sample-positioning procedure that is complicated by the usually limited field of view at the beamline.

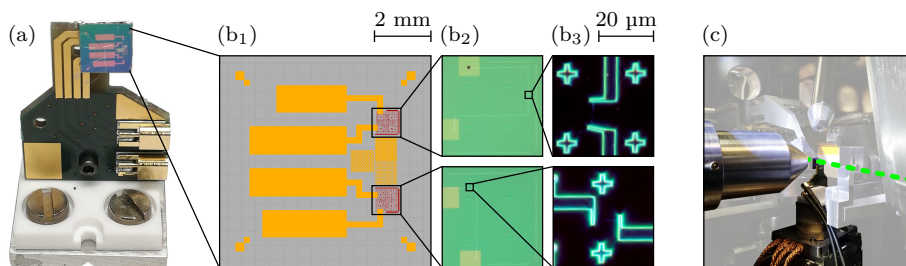


Figure 5.27: Sample architecture and setup. The contacted sample glued to a PCB is mounted on the sample holder (a). The KLayout Editor mask (b_1) illustrates the electrical architecture with gold (yellow) contact pads and tracks, platinum (red) markers and leads. Bright field (b_2) and dark field (b_3) optical microscopy images show the location of the contacted CdTe NWs within the top and the bottom panel, respectively. The experiment geometry (c) within the vacuum chamber at beamline 26-ID-C comprises the XRF detector (left) and the sample (center) that is positioned on a motor stack.

The thin platinum leads were tailored to the location and orientation of the transferred NWs, which were ascertained by means of optical microscopy. The bright (b_2) and dark field (b_3) images show the position of the NWs on the substrate for the top and bottom device, respectively. In order to minimize the region of interest for X-ray microscopy and thus reduce the measurement time, NWs oriented parallel to either of the substrate edges were selected. The experiment configuration at beamline 26-ID-C is shown in Figure 5.27c, with the sample (center) being positioned on a motor stack in a vacuum chamber. The XRF detector (left) is situated in close proximity to the sample at an angle of 90° with respect to the X-ray beam (green highlight) that would be entering the image from the left. The fixed position of the XRF detector entails a rotation of the sample towards the detector to reduce self-absorption in the sample volume. However, this effect is negligible in case of the nanoscopic wires.

The CdTe NWs are well suited as a model system to be investigated at this hard X-ray beamline that can provide beam energies ranging between 6–12 keV allowing for excitation above the X-ray L-absorption edges as is shown in Table 5.8. The chosen beam energy of 8.4 keV enables the evaluation of the spatial distribution of all main elements in the sample including both compounds of the binary semiconductor Cd ($E_{\text{LIII}}^{\text{abs}}(\text{Cd}) = 3.5$ keV) and Te ($E_{\text{LIII}}^{\text{abs}}(\text{Te}) = 4.3$ keV), as well as the Pt metal contact ($E_{\text{M}}^{\text{abs}}(\text{Pt}) = 3.3$ keV) and the Si substrate ($E_{\text{K}}^{\text{abs}}(\text{Si}) = 1.8$ keV).^[176]

Table 5.8: X-ray absorption edges of cadmium and chalcogens.^[176]

	K / keV	L _{III} / keV
Cd	26.71	3.54
S	2.47	0.23
Se	12.65	1.43
Te	31.81	4.34

In addition to these clearly discernible elements, residual Bi catalyst-particles were conjectured to be remaining attached to a fraction of the NWs. The XRF spectra were recorded with a multi-element silicon drift detector. For the evaluation of the data, each element was treated individually, to account for the different energy calibration and geometry with respect to the sample as was detailed by Ziska et al.^[125] Furthermore, a custom background subtraction algorithm was applied to facilitate the analysis of the vestigial fluorescence signal of the catalyst particles (Bi M-lines) in the low energy region of the recorded XRF spectra, as is exemplarily shown for detector module two in Figure 5.28. Complementary to the XRF sum spectrum (black) integrated over all scan points and the background (yellow), both the fit of the sum (solid green) and the sum of fits (dashed green) are illustrated. While the former fit is directly retrieved from the sum spectrum, the latter is procured by adding the individual fits of each single pixel spectrum, thus giving a measure of the representation of the highly localized features that contribute only few counts. Both fits were found to be in overall good agreement with the sum spectrum.

The sum of fits exceeds the number of integrated counts at energies higher than 4 keV, which can either be attributed to the strong local variations in the sample structure or insufficient background optimization on the single pixel level. The background was assumed to be homogeneous throughout the scan area and the contribution was thus estimated by fitting the integrated spectrum and subsequently dividing the obtained sum background by the number of pixels. The critical energy region of interest containing the Pt M-lines (light blue), Bi M-lines (turquoise), Cd L-lines (dark blue) and Te L-lines (gray) exhibits a good agreement between the fit of sum and the sum of fits, albeit showing a significant overestimation of the platinum contribution. While this behavior is unsatisfactory with respect to the fit results themselves, other factors such as the elemental separation and, ultimately, the 2D elemental distribution should be considered for the evaluation of the confidence of the fit.

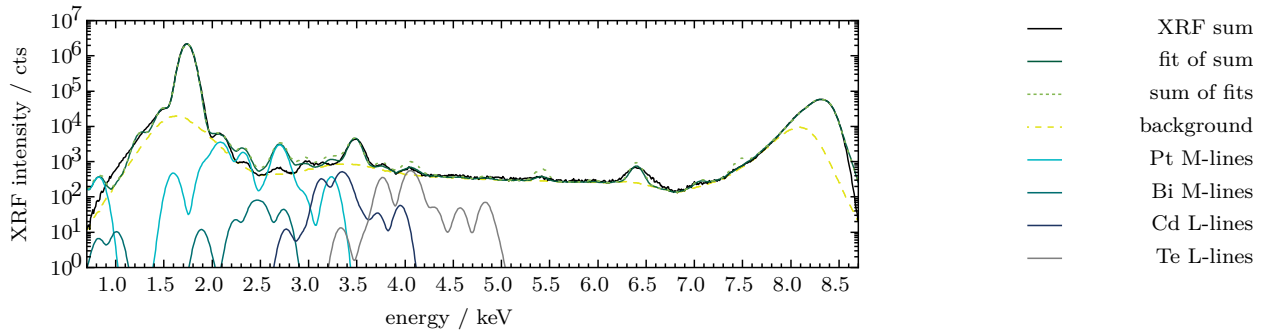


Figure 5.28: XRF sum spectrum of the contacted CdTe NW. The sum background (yellow) is snipped from integrated counts (black) prior to applying the fit of sum (solid green). The sum of fits (dashed green) represents the integration of the individual fits to the single pixel spectra. The XRF transitions taken into consideration mainly evoke superposed signals in the energy region of interest between 2.0 keV–4.2 keV.

To achieve elemental separation and extricate the Bi lines, thus verifying the presence of catalyst particles, the various XRF lines listed in Table 5.9 were taken into account using fixed intensity ratios within the group of XRF transitions arising from the respective elements. Due to the overlap of the Bi signals with either Pt or Cd, only the most prominent Bi M-line (M5N7) at 2.42 keV was used to achieve elemental separation in the subsequent analysis. In Figure 5.28 the fixed-ratio Ansatz including all listed Bi transitions is shown to illustrate the intricate conjunction of XRF lines and the need for an elaborate fit procedure to disentangle background and individual elemental contributions especially with regard to correlative analysis of the other modalities.^[134]

Table 5.9: Characteristic electronic transitions used for the analysis of the X-ray fluorescence spectra.^{[134][176]}

	X-ray transitions		
		line	E_{line} / keV
Cd	$L\alpha_1$	L3M5	3.13
	$L\beta_1$	L2M4	3.32
	$L\beta_2$	L3N5	3.53
Te	$L\alpha_1$	L3M5	3.77
	$L\alpha_2$	L3M4	3.76
	$L\beta_1$	L2M4	4.03
	$L\beta_2$	L3N5	4.30
	$L\beta_3$	L1M3	4.12
	$L\beta_4$	L1M2	4.07
Pt	$M\alpha$	M5N7	2.05
	$M\beta$	M4N6	2.13
	$M\gamma$	M3N5	2.33
		M2N4	1.59
Si	$K\alpha_1$	KL3	1.74
	$K\alpha_2$	KL2	1.74
	$K\beta_1$	KM3	1.84
Bi	$M\alpha$	M5N7	2.42
	$M\beta$	M4N6	2.53
	$M\gamma$	M3N5	2.74
		M2N4	1.88

The spatial distribution of the relevant elements is represented in Figure 5.29a as 2D maps of the respective XRF count-rate f_i of the individual elements i that was retrieved for each scan pixel by normalizing the integral of the fitted peaks to the dwell time and the photon flux. The macroscopic electrodes are clearly discernible in the Pt channel (a_1). The contour of the metal contacts was retrieved and used to highlight the area in the other maps. The substrate (a_2) evokes much higher count rates with a slight shadowing in the electrode area, which may be attributed to reduced transmission of the Si fluorescence through the 20 nm thick platinum layer and the coincidence of the XRF lines of both elements. The separation of these copious sample components was deferred as such, but interrelates with the unambiguous mapping of the nanostructures, which is why the Si channel is illustrated supplementary. Nonetheless, both semiconductor compounds Cd (a_3) and Te (a_4) could be extracted with a high signal-to-noise ratio even in the electrode area thus indicating an effective disentanglement of Pt and Cd XRF.

The NW can clearly be observed to extend below the contacts with some additional CdTe material being discernible in the top third of the structure and the lower section at a length of 3.5 μm , which implies the presence of further NWs. The SLS QNWs have been found to form small bundles rather than being transferred onto the substrate completely singular. The catalyst-assisted colloidal synthesis further causes Bi NPs to be attached to half of the NW ends in principle. While some of them may break off during stirring and sample transfer, Bi NPs are commonly observed at the NW ends in TEM images but hardly ever as individual NPs, since smaller structures are removed during the sample-preparation procedure. The catalyst particles found on the substrate are consequently indicative of NW ends. Hence, the intricate fit procedure was developed to unambiguously ratify the presence of Bi in proximity to the NWs. The Bi channel (a_5) appears to be comparably noisy, which is however rather caused by the small number of counts that originate from the minuscule amount of Bi. Assuming a diameter of 7.6 nm for the pristine Bi NPs before SLS synthesis and a Bi density of 9.8 g/cm³, the XRF signal of as few as ~6500 atoms could be detected even with the intrinsically arduous M transitions. Contemplating the electrode area, the deconvolution of Pt and Bi can be assumed as successful due to the slightly reduced number of counts in those regions, proving that no Pt counts were wrongfully attributed to the Bi XRF. However, the shape of the NW can be tracked in the Bi channel without bias to the eye from the other maps. This may be due to the remaining interference of the Bi M5N7-line and the Cd counts.

In contrast to the Pt used for the electrodes, the Cd counts are not only energetically close to the Bi signal, but are also spatially highly correlated, which renders a clear distinction difficult. Nonetheless, three regions of interest with heightened Bi count rates manifest at (1) $[(1.6\text{--}2.2)\ \mu\text{m} \times (2.7\text{--}4.1)\ \mu\text{m}]$ close to the bottom of scan, at (2) $[(1.4\text{--}1.6)\ \mu\text{m} \times (9.5\text{--}9.8)\ \mu\text{m}]$ and at (3) $[(1.4\text{--}1.6)\ \mu\text{m} \times (11.0\text{--}11.3)\ \mu\text{m}]$ in the upper part in map (a₅).

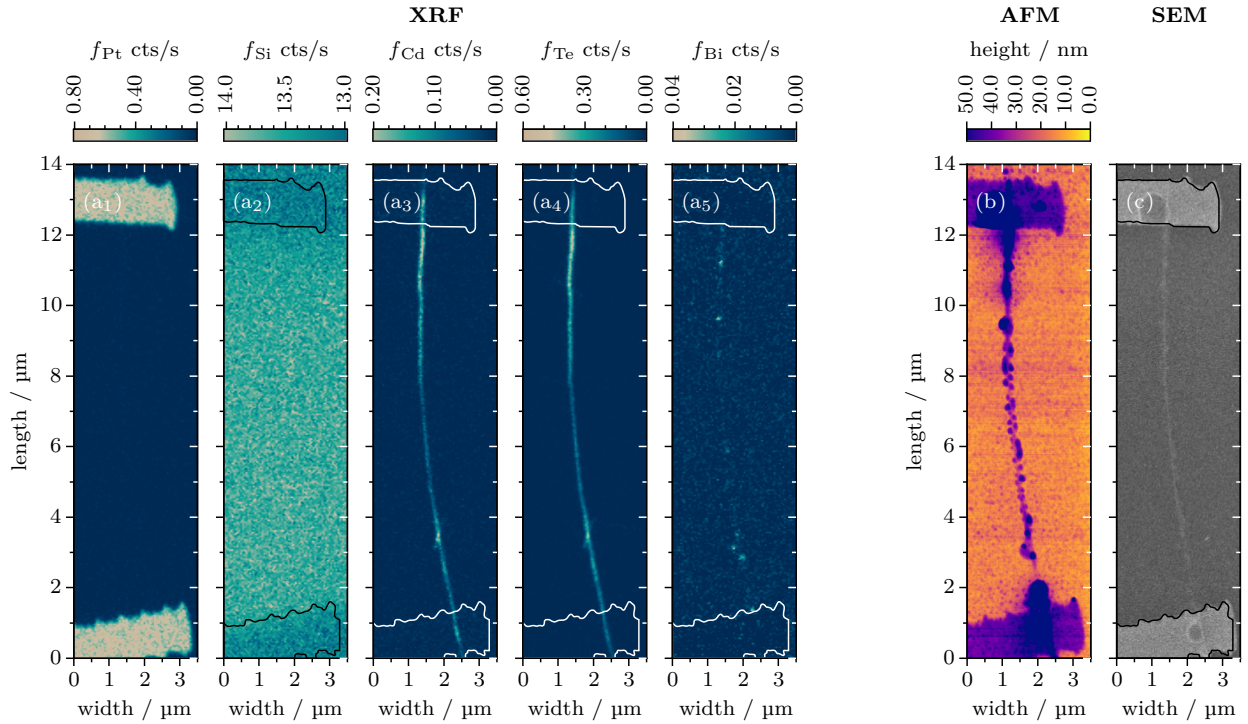


Figure 5.29: Maps of the contacted CdTe NW. From the high-resolution XRF scan, maps (a) of the relevant elements (Pt, Si, Cd, Te, Bi) contained in the sample were retrieved using the custom XRF fitting code. In fixed ratio and Bi M5N7 configuration. The position of the contacts retrieved from the Pt channel is highlighted. The four detector modules were averaged to obtain the final maps. The position of the contacts retrieved from the Pt channel is highlighted. An AFM (b) and an SEM (c) micrograph are shown for comparison. Note, that the SEM image has been sheered in horizontal direction to account for the large sample drift during the measurement, which however was assumed to be constant.

All ROI do concur with the aforementioned regions exhibiting elevated count rates of both, Cd and Te, that hint at the presence of additional semiconductor material and thus more than a single NW as the intrawire diameter should remain constant in first approximation. In fact, an auxiliary structure is observable at an angle with respect to the main NW in the top section of ROI(1). This ROI comprises a total of three potential Bi NPs with one of them being positioned to the left of the primary NW but supposedly at the end of the diagonally oriented NW. The other two

spots coincide with regions of elevated count rates along the main structure. The same observation can be made for RIO (2) and (3) in the top section of the scan with at least two additional NWs presumably forming a strand of NWs. Since a maximum of 50% of SLS-NW ends can have catalyst particles attached to them, it can be speculated that even more than the suspected five additional NWs are present. Neither that, nor the integrity of the complete one-dimensional semiconductor nanostructure between the electrical contacts can be confirmed or denied with certainty by means of XRF.

To evaluate the geometric structure of the sample and gain further insight into the presence of additional NWs, AFM and SEM images were collected, however only after the synchrotron-based measurements. Especially the atomic force micrograph in Figure 5.29b reveals a multitude of bubble like structures that follow the trajectory of the NW, thus completely obscuring the semiconductor and possible catalyst particles, although the presumed positions of the Bi NPs may be perceived. Contemplating not only the amplitude of the cantilever oscillation, but also the phase, renders material contrast ancillary to the mere sample topology. Based on the AFM-phase information and knowledge of the sample-preparation procedure, it can be assumed, that lift-off during lithography was incomplete and residues of the organic photoresist remain on the nanostructured sample. Interestingly, the second contacted NW on the substrate (see Figure 5.27b₁ for sample architecture) does appear pristine, suggesting that the bubbles are an indication of radiation damage. The electron micrograph in Figure 5.29c reveals a similar trend. The scan of the primary sample precludes the extraction of information about the presence of additional NWs or catalyst particles. Although operating at the limit of resolution for SEM, individual species within a bundle of NWs could be observed in the micrograph of the secondary sample. Contrary to the assumption that the X-ray radiation damage mainly affects the organic photoresist, the semiconductor itself is hardly observable in the region just above the bottom electrode in the SEM image, while the compounds Cd and Te are clearly discernible in the respective XRF channels. The higher magnified SEM scan in Figure 5.30 of an area corresponding to ROI(1) does strongly support the presence of NPs at the positions in question and further confirms the existence of the diagonally oriented NW. Due to the extent of the damage to the sample and the nature of the methods, the NPs could not be confirmed to consist of Bi with certainty.

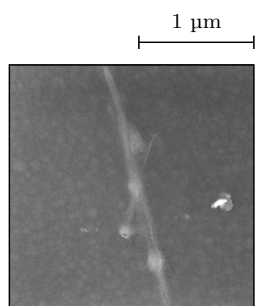


Figure 5.30: High magnification SEM image. ROI(1) defined from the Bi map of the XRF comprises at least one additional NW oriented at an angle with respect to the primary NW. Three NP-like structures are also discernible at the suspected positions.

Thus, the XRF-analysis was repeated at the P06 microprobe using a beam energy of 18.0 keV, which is above the L_1 absorption edge of Pt and, more importantly, Bi. The accessible absorption edges of all the elements of interest are listed in Table 5.10 for the experiment configurations at P06 (bold) and 26-ID-C (italic). The corresponding XRF L-lines can be assigned much more unambiguously than the respective M-Lines. Instead of having to resort to the custom fit method, the established program PyMCA that was developed at ESRF could be used. The elemental distribution of both, Pt and Bi are shown in Figure 5.31a. The prominent vertical line is caused by a beam dump that occurred mid scan. Furthermore, a large horizontal sample drift could be observed, resulting in a distortion of the map in comparison to the micrographs retrieved via the other methods. It was refrained from showing the maps of the semiconductor compounds, as both beam energy and resolution were not optimal to obtain information that contribute beyond the insight gained from the previous nano-XRF analysis. The Pt contacts (a_1) serve as orientation to

Table 5.10: X-ray absorption edges of the elements of interest accessible at a beam energy of 18.0 keV (bold) used at P06 and at 8.4 keV (italic) used at 26-ID-C.^[176]

	L_{III} / keV	M / keV
Cd	3.54	0.41
Te	4.34	0.57
Pt	11.56	<i>2.12</i>
Bi	13.41	<i>2.58</i>

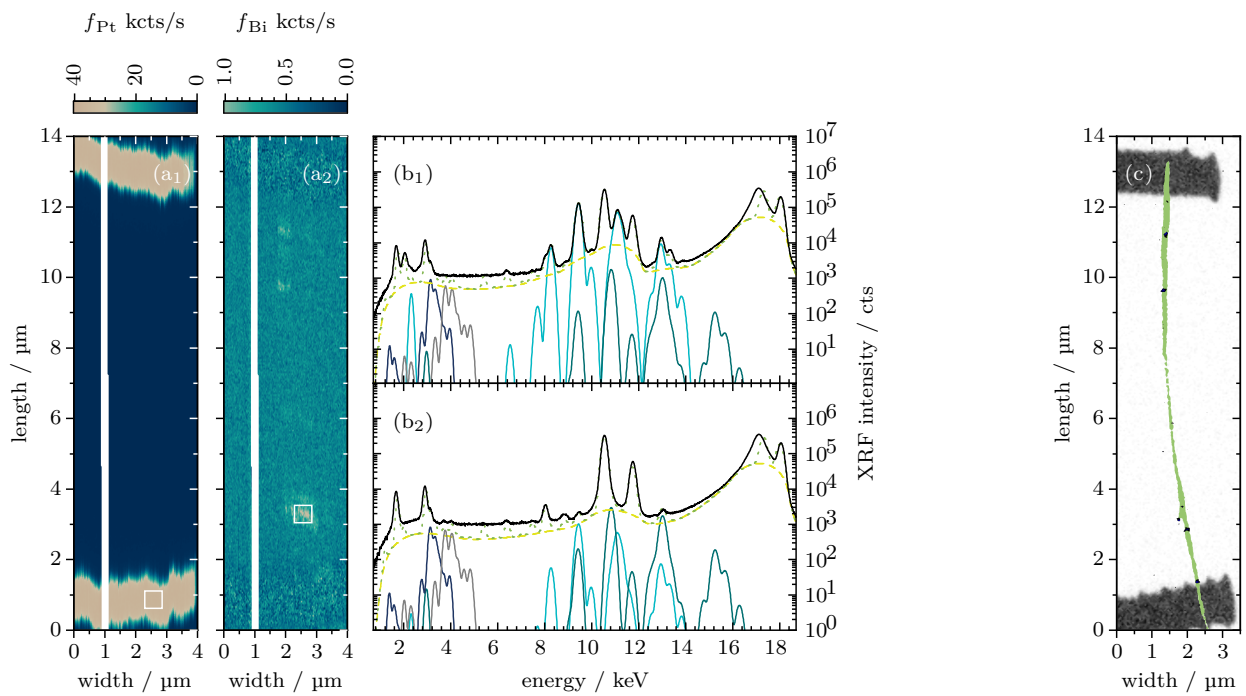


Figure 5.31: XRF-analysis of Bi and Pt L-lines. The probe energy of 18.0 keV at the P06 microprobe allowed for the investigation of the elemental distribution of Pt (a_1) and Bi (a_2) using their XRF L-lines. The spectra (b) represent the energetical count distribution within the two regions of interest highlighted with white rectangles, with (b_1) corresponding to the Pt contact area and (b_2) to the Bi signal. The nanograph comprising an overlay of the XRF-channels Pt (gray), Te (green) and Bi (blue) obtained at 26-ID-C is shown for comparison.

correlate the position of the Bi (a_2) signals to the ROI that were defined based on Figure 5.29. Two sub-sum spectra retrieved from the areas highlighted in scans (a_1) and (a_2) with white rectangles are shown in (b_1) and (b_2). For the representation of the fits, the same color code was used as in Figure 5.28 with the integrated counts illustrated in black, the background in yellow and the sum of fits in green (dashed). In both cases a clear energetical separation between the compound L-lines (Cd (dark blue), Te (gray)) and the metal L-lines (Pt (light blue), Bi (turquoise)) is apparent, thus verifying that the surmised Bi signal is not evoked by erroneously attributed Cd counts. However, the fit program attributes counts to both elements in both sub-spectra, due to the still insufficient separation between Pt and Bi L-lines. A strong reduction of the Pt L-lines can be observed in the Bi-rich spectrum (b_2), while only few counts are attributed to the catalyst in the Pt-rich spectrum (b_1) This is in line with the presumption, that no Pt has been deposited outside the electrode area during lithography. The prominent peaks at 10.4 keV and 11.8 keV are assigned to arsenic, which has been found in multiple other experiments at the beamline as well. The custom fit method may also contribute to a more effective elemental separation, however the goal of the experiment was to ratify the existence of Bi-NPs on the substrate using an independent approach. In Figure 5.31c the Pt (gray), Te (green) and Bi (blue) channel retrieved from the nanographs of the experiment at 26-ID-C are overlayed for comparison. It can be seen, that the vertical position of the Bi signal along the length of the NW coincide well in both scans conducted at the different beamlines, indicating the effective detection of the catalyst particles.

The probe energy of 18.0 keV furthered the elemental differentiation by enabling the excitation of the metals above the L-edge, thus evoking the stronger XRF L-lines, while sacrificing sensitivity to the semiconductor compounds. The latter were investigated in detail and with better spatial resolution using the probe energy of 8.4 keV provided at 26-ID-C. The catalyst Bi-NPs that hint at the presence of additional NWs could be detected along the one-dimensional nanostructure and at least one NW laying at an angle to the primary structure was identified. It may be assumed that instead of a single NW, a bundle of NWs was contacted. By all means available, it could not be established whether a fraction of the individual NWs within the bundle span the gap between the electrodes and are contacted on both sides.

In the multi-modal approach, the electrical characteristics of the NW sample were ascertained in parallel to the elemental distribution. The sample mounted on the PCB shown in Figure 5.27a was connected to a pre-amplifier (PrA) that was positioned in proximity to the vacuum chamber. The pre-amplified signal was either used as input for the Lock-in amplifier (LIA) or directly read-out by the analogue-to-digital converter (ADC). The electrical setup, including the grounding scheme, is illustrated in Figure 5.32 including hole (red) and electron (blue) current. Auxiliary to the main XBIC-signal, a parasitic replacement current may be evoked to maintain charge neutrality as surface electrons are ejected from the sample into the vacuum and ultimately absorbed at the chamber wall (CW). In this specific case, with the device under test being oriented perpendicular to the beam in the sample plane, the choice of ground electrode is irrelevant. In electronic devices such as solar cells however, the front contact should be grounded to avoid misinterpretation of the current replacing the ejected photoelectrons as XBIC signal.^[128]

The XBIC signal was retrieved using the post-processing scheme detailed in ref.^[129], using a pre-amplification factor A_{PrA} of 0.2 V/pA and a Lock-in-amplification factor A_{LIA} of 200 V/V. The ADC featured a voltage acceptance range R_V of 5 V spanning a frequency range of R_f of 1 MHz. Although being modulated by a mechanical disc chopper, the waveform of the input signal was assumed to be square as the on- and off- periods are significantly longer than the transition time, which is dependent on the chopper frequency, sharpness of the blade edges and the probe size. The large pre-amplification factor entails a slow response of the instrument, which is why the probe was modulated with a frequency of 7.3 Hz. The direct signal was split and one channel was inverted prior to V2F-conversion to account for negative currents. In post-processing, the two channels were combined to compute a single direct current with positive and negative contributions. The spatial distributions of the demodulated XBIC-signal and the directly digitalized XBIC for a bias voltage of 0 V are shown in Figure 5.33a and (c), respectively. In both cases, the top contact is clearly observable as well as a fraction of the NW. Contrary to the expectations, the bottom contact is also discernible, which may be attributed to photoelectrons ejected from that area absorbing at the top electrode rather than the chamber wall, consequently contributing to a current being registered in spite of the bottom electrode being grounded. The dashed arrow (electron, blue) spanning the gap between the electrodes in Figure 5.32 was included in the sketch to showcase this process.

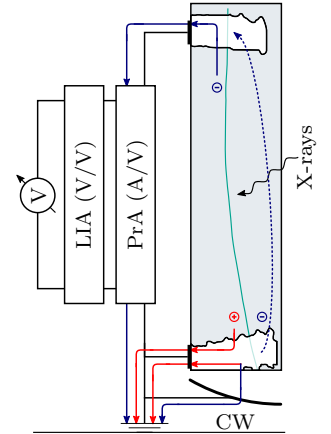


Figure 5.32: Scheme of XBIC setup. The electrical signal is pre-amplified and subsequently analyzed with the Lock-in amplifier. The grounding scheme is included to illustrate the possible contribution of the replacement current caused by ejected photoelectrons that are collected at the chamber wall (CW).

It can be seen, that the charge imbalance caused by reabsorbed photoelectrons at the top contact is registered by the PrA with the opposite sign compared to the original compensation current localized at the bottom contact that can not be detected in this setup. In order to compare and potentially disentangle DC bias and XBIC of the NW, a pixel mask was created on the basis of the spatial distribution of Pt and Te counts. The AC and DC values are histogrammed in the violin plots in Figure 5.33b for the series of applied bias voltages. In all subsets, the mean value is marked with a white dashed line, while the 25th and 75th percentile are highlighted with dotted lines in the color of the respective violin. Black lines connecting the mean values within each series are used to emphasize disparities between the distributions. The XBIC histograms (bold, bot-

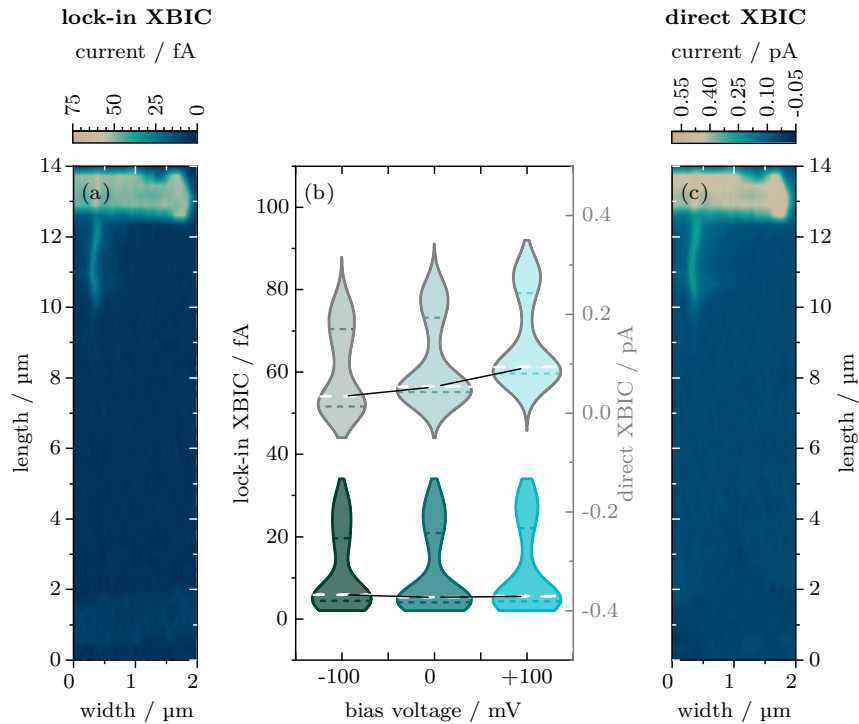


Figure 5.33: Comparison of lock-in and direct XBIC. The spatial distributions of the demodulated and direct X-ray beam induced current with a bias voltage of 0 V applied are mapped in (a) and (c), respectively. Using the Pt and Te XRF-channels as template, the pixel values of only the NW were extracted from both, AC and DC map. The lock-in (bold, bottom) and direct XBIC (grayish, top) distributions extracted from each individual scan within the bias series are histogrammed in (b).

tom) appear to be of nearly equal shape and constant mean value, whereas the direct current histograms (grayish, top) exhibit an increase in mean value. Note, that setting a positive bias in the PrA resulted in a negative voltage in the scope of the LIA. Consequently, the nominal bias settings

were inverted. In addition to the change in mean value, a variation in shape is apparent for the direct signal. Both non-zero bias measurements show a cut-off edge in the distribution, which can be attributed to the design of the pixel mask and the choice of count limits for Pt and Te. As the XRF-signal was normalized to the photon flux, the mask limits were maintained constant throughout the series. The balance between discarding possible NW counts and erroneously including substrate/background counts proved to be delicate. The final limit was chosen as to ensure that the registered pixels do contain the NW, while conceding to potentially exclude some fainter signals originating from the nanostructure. Due to the excellent SRN in the Pt channel, the limit was uncritical. Nonetheless, it affects the shape of the current distributions, as the contact region with an overlap between NW and electrode was excluded to minimize the convolution of semiconductor and metal contribution. Consequently, a sharp onset of direct current values can be seen in the negative bias case on the lower end that originates from the bottom electrode. Likewise, the exclusion of the Pt area results in a similar behavior in the positive case on the top electrode for high current values.

Finally, the spatial variation of the electrical signal along the NW was analyzed by extracting profiles of the various channels. In order to find the correct positions and "straighten" the bent NW, the pixel index correlating to the maximum Te count in each row was derived by means of Gaussian fits to the Te distribution. A slight distortion with respect to the actual length NW due to its original orientation on the substrate was condoned, especially considering the step size of $0.27\ \mu\text{m}/\text{px}$. The overlay of the Pt (gray), Te (light green) and Bi (blue) XRF-channels representing the high-resolution scan is reproduced in Figure 5.34a to enable the correlation between electrical signal and structural characteristics along the NW. The position of the electrodes with respect to the NW is highlighted by the gray boxes in (b), while the location of the Bi-NPs is indicated by the dashed blue vertical lines. The obtained profiles of the direct current are shown in (b) (bottom set, bold) for the three bias voltages +100 mV (light blue), 0 mV (turquoise) and -100 mV (dark green). In these profiles, the effect of the left Pt electrode is clearly discernible. Throughout the bias series, a local minimum of the direct current is visible between the edge of the electrode, followed by a plateau of nearly constant current, before the signal decreases at a length of $\sim 3.6\ \mu\text{m}$. The mid-section of the NW exhibits a second plateau, until the proximity to the ground electrode (right) causes a further decrease at a length around $10\ \mu\text{m}$.

The Bi-NPs located between 10.4 μm –11.2 μm that have been found to be attached to the small additional NW, can be correlated to a small local minimum in the current profiles. A similar, yet even more indistinct, local minimum may be perceived at 2.8 μm , which would coincide with the location of another catalyst particle. However, this observation can not be unambiguously confirmed, as the resolution of the bias scans was reduced in order to afford the completion of the series within a reasonable time frame. In contrast, no elevated Bi count rate was detected at 3.6 μm which would coincide with the abrupt decrease of the direct current.

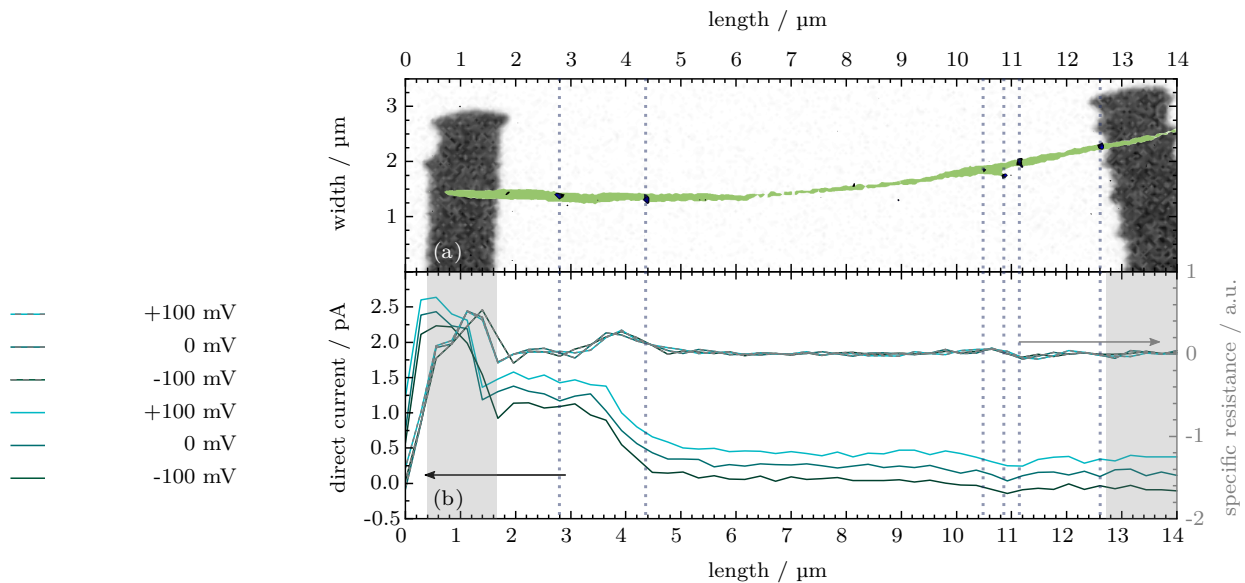


Figure 5.34: Direct XBIC profile along the NW. The profiles (b) were extracted from the bias-series scans by retrieving the position of the NW from the Te XRF-channel. The high-resolution scan (a) allows for the correlation between the elemental distribution and the electrical characteristics. The derivatives of the direct current profiles (bold, bottom set) were calculated to find the specific resistance (gray dashed, top set) at each position along the NW. The gray boxes and the dashed blue lines highlight the location of the electrodes and the Bi-NPs, respectively.

The last NP of interest has been identified at 4.4 μm which is in the range of the transition between the aforementioned decrease and the mid-section plateau. Due to the presumably defect limited electrical conductivity of the semiconductor and the nanofocus of the probe, it is likely, that no conducting channel has been activated under the highly localized illumination. The sudden onset of the decay contra-indicates the hypothesis, that a characteristic charge-collection length has been reached at that point. Taking the previously noted increased Te count rate in proximity to the left electrode into account, it is more likely, that at least one of the

NWs forming the superstructure ends at that point. The local maxima of the derivatives of the direct current, which may be considered as a measure for the specific resistance along the NW, further supports the latter assumption. The gradual decrease of the current spanning a length of approximately $1\ \mu\text{m}$ indicates, that charge transport between the individual NWs in the bundle is existent.

In other XBIC experiments, front-contact grounding was applied as to suppress the suspected contribution of a replacement current to the XBIV and XBIC signal of the system.^[128,177] The geometry of the NW sample with the plane of the electrical response being oriented perpendicular to the incident beam, renders these precautions irrelevant. It is suspected, that the electrical signal of not only the contacts, but of the NW bundle itself is primarily caused by the compensation of photo-ejected electrons. This experiment can thus be comprehended as a strong indication for the in case of other sample systems such as solar cells often detrimental replacement current.

6 | Summary

In this thesis, the optical properties of one-dimensional cadmium chalcogenide nanostructures were analyzed and correlated to the morphology of the nanowires to elucidate the structure–property relationship. The structural characteristics include the diameter that governs quantization, phase alternations between wurtzite and zinc-blende segments in colloiddally synthesized nanowires and the ligand system used to complexate the precursor and passivate the surface of the final nanostructure.

Primarily wurtzite-phase CdTe nanowires with reduced phase-alternation frequency were found to exhibit a series of feature-rich PL-emission lines that are subject to spectral discontinuities, which occur as discrete jumps between "memorized" energies. In addition, replicas in the NIR could be allocated to all these lines, which may be induced by exciting the organic ligand shell surrounding the photo-active semiconductor.

Consequently, surface-alteration procedures were conducted, including both, organic and inorganic ligand-exchange reactions. The latter was executed via the cALD approach, which is based on phase-transfer reactions in order to purge excessive material. Here, CdSe/CdS was chosen as the sample system as it has an optimal lattice mismatch for epitaxial growth and it was used to demonstrate the feasibility of the procedure in case of nanorods and nanoplatelets in the literature. The more challenging nanowires, concerning their colloidal stability, were successfully subjected to this layer-by-layer deposition and the resulting core/shell nanowires were spectroscopically characterized. Due to the comparatively large diameter of the parent nanowires beyond the quantization limit, no pronounced changes in the emission wavelength were observed. The deposition of the shell did however affect the kinetics of the recombination and decreased the already short photoluminescence lifetime, which may be attributed to the insufficient quality of the shell introducing defects and deficient passivation of the shell surface.

CdS itself does exhibit two emission bands, one of which can be assigned to trap emission. This red-shifted photoluminescence can thus serve as a measure for the amount of active surface traps present on the semicon-

ductor. Different phosphonic acids serving as ligands were hence employed during synthesis in order to circumvent post-synthetic exchange-reactions. While the morphology of the resulting CdS nanowires remained comparable, the trap emission was observed to decrease with increase of the alkyl residue of the ligand.

Finally, a sample of electrically contacted CdTe nanowires was X-ray microscopically analyzed to correlate the elemental distribution to the electrical response of the device. The recorded electric signal can probably be attributed to a replacement current compensating for ionization events that eject electrons from the sample area. In addition, the presence of individual bismuth catalyst-particles along the nanowires was ratified, despite the small number of atoms incorporated in a single particle.

In future experiments, the established synthesis parameters for CdTe should be back-transferred to CdSe quantum-nanowires as they photoluminesce more reliably than their CdTe counterparts and are less susceptible to ambient conditions, rendering both, synthesis and sample handling more facile. In a further step, homoepitaxial surface-modification could be conducted via the cALD method to evaluate the influence of the altered surface chemistry without the obscuring effect of a heterostructure. Beyond that, the cadmium chalcogenide nanowires are well suited for multi-modal X-ray microscopy, concerting X-ray fluorescence, X-ray beam induced current, X-ray excited optical luminescence and potentially X-ray diffraction investigations. This powerful set of modalities may even be employed on ex-situ sample-treatment experiments such as doping, cation exchange and ligand-exchange reactions.

Bibliography

- [1] F. Wang, A. Dong, and W. E. Buhro, “Solution–Liquid–Solid Synthesis, Properties, and Applications of One-Dimensional Colloidal Semiconductor Nanorods and Nanowires”, *Chem. Rev.*, **2016**, *116*, 18, 10888–10933.
- [2] Y. Li, F. Qian, J. Xiang, and C. M. Lieber, “Nanowire electronic and optoelectronic devices”, *Mater. Today*, **2006**, *9*, 10, 18–27.
- [3] A. Littig, H. Lehmann, C. Klinke, T. Kipp, and A. Mews, “Solution-Grown Nanowire Devices for Sensitive and Fast Photodetection”, *ACS Appl. Mater. Interfaces*, **2015**, *7*, 22, 12184–12192.
- [4] F. Patolsky, G. Zheng, and C. M. Lieber, “Nanowire-Based Biosensors”, *Anal. Chem.*, **2006**, *78*, 13, 4260–4269.
- [5] N. P. Dasgupta, J. Sun, C. Liu, S. Brittman, S. C. Andrews, J. Lim, H. Gao, R. Yan, and P. Yang, “25th anniversary article: Semiconductor nanowires - Synthesis, characterization, and applications”, *Adv. Mater.*, **2014**, *26*, 14, 2137–2184.
- [6] M. Law, H. Kind, B. Messer, F. Kim, and P. Yang, “Photochemical Sensing of NO₂ with SnO₂ Nanoribbon Nanosensors at Room Temperature”, *Angew. Chem. Int. Ed*, **2002**, *41*, 13, 2405–2408.
- [7] H. Dang and V. P. Singh, “Nanowire CdS-CdTe Solar Cells with Molybdenum Oxide as Contact”, *Sci. Rep.*, **2015**, *5*, 1, 14859.
- [8] J. E. M. Haverkort, E. C. Garnett, and E. P. A. M. Bakkers, “Fundamentals of the nanowire solar cell: Optimization of the open circuit voltage”, *Appl. Phys. Rev.*, **2018**, *5*, 3, 031106.
- [9] X. Duan, Y. Huang, Y. Cui, J. Wang, and C. M. Lieber, “Indium phosphide nanowires as building blocks for nanoscale electronic and optoelectronic devices”, *Nature*, **2001**, *409*, 6816, 66–69.
- [10] N. Tessler, V. Medvedev, M. Kazes, S. H. Kan, and U. Banin, “Efficient near-infrared polymer nanocrystal light-emitting diodes”, *Science (80-.)*, **2002**, *295*, 5559, 1506–1508.

-
- [11] H. Kind, H. Yan, B. Messer, M. Law, and P. Yang, “Nanowire Ultraviolet Photodetectors and Optical Switches”, *Adv. Mater.*, **2002**, *14*, 2, 158–160.
- [12] D. Van Dam, D. R. Abujetas, R. Paniagua-Domínguez, J. A. Sánchez-Gil, E. P. Bakkers, J. E. Haverkort, and J. Gómez Rivas, “Directional and Polarized Emission from Nanowire Arrays”, *Nano Lett.*, **2015**, *15*, 7, 4557–4563.
- [13] R. Yan, D. Gargas, and P. Yang, “Nanowire photonics”, *Nat. Photonics*, **2009**, *3*, 10, 569–576.
- [14] T. J. Trentler, K. M. Hickman, S. C. Goel, A. M. Viano, P. C. Gibbons, and W. E. Buhro, “Solution-Liquid-Solid Growth of Crystalline III-V Semiconductors: An Analogy to Vapor-Liquid-Solid Growth”, *Science (80-.)*, **1995**, *270*, 5243, 1791–1794.
- [15] S. Ithurria and D. V. Talapin, “Colloidal Atomic Layer Deposition (c-ALD) using Self-Limiting Reactions at Nanocrystal Surface Coupled to Phase Transfer between Polar and Nonpolar Media”, *J. Am. Chem. Soc.*, **2012**, *134*, 45, 18585–18590.
- [16] A. Nag, M. V. Kovalenko, J.-S. Lee, W. Liu, B. Spokoyny, and D. V. Talapin, “Metal-free Inorganic Ligands for Colloidal Nanocrystals: S^{2-} , HS^- , Se^{2-} , HSe^- , Te^{2-} , HTe^- , TeS_3^{2-} , OH^- , and NH_2^- as Surface Ligands”, *J. Am. Chem. Soc.*, **2011**, *133*, 27, 10612–10620.
- [17] D. V. Talapin, R. Koeppel, S. Götzinger, A. Kornowski, J. M. Lupton, A. L. Rogach, O. Benson, J. Feldmann, and H. Weller, “Highly Emissive Colloidal CdSe/CdS Heterostructures of Mixed Dimensionality”, *Nano Lett.*, **2003**, *3*, 12, 1677–1681.
- [18] D. B. Straus, E. D. Goodwin, E. A. Gaulding, S. Muramoto, C. B. Murray, and C. R. Kagan, “Increased Carrier Mobility and Lifetime in CdSe Quantum Dot Thin Films through Surface Trap Passivation and Doping”, *J. Phys. Chem. Lett.*, **2015**, *6*, 22, 4605–4609.
- [19] D. Franz, A. Reich, C. Strelow, Z. Wang, A. Kornowski, T. Kipp, and A. Mews, “Quantum-Confined Emission and Fluorescence Blinking of Individual Exciton Complexes in CdSe Nanowires”, *Nano Lett.*, **2014**, *14*, 11, 6655–6659.
- [20] F. Wang, R. A. Loomis, and W. E. Buhro, “Spectroscopic Properties of Phase-Pure and Polytropic Colloidal Semiconductor Quantum Wires”, *ACS Nano*, **2016**, *10*, 10, 9745–9754.
-

- [21] T. B. Hoang, A. F. Moses, H. L. Zhou, D. L. Dheeraj, B. O. Fimland, and H. Weman, “Observation of free exciton photoluminescence emission from single wurtzite GaAs nanowires”, *Appl. Phys. Lett.*, **2009**, *94*, 13, 133105.
- [22] F. Wang and W. E. Buhro, “Crystal-Phase Control of Catalytically Grown Colloidal CdTe Quantum Wires: Dual Role of *n*-Tetradecylphosphonic Acid”, *Chem. Mater.*, **2018**, *30*, 4, 1316–1323.
- [23] A. L. Efros and D. J. Nesbitt, “Origin and control of blinking in quantum dots”, *Nat. Nanotechnol.*, **2016**, *11*, 8, 661–671.
- [24] P. Frantsuzov, M. Kuno, B. Jankó, and R. A. Marcus, “Universal emission intermittency in quantum dots, nanorods and nanowires”, *Nat. Phys.*, **2008**, *4*, 7, 519–522.
- [25] C. R. Carey, Y. Yu, M. Kuno, and G. V. Hartland, “Ultrafast Transient Absorption Measurements of Charge Carrier Dynamics in Single II-VI Nanowires”, *J. Phys. Chem. C*, **2009**, *113*, 44, 19077–19081.
- [26] X. S. Zhao, J. Schroeder, P. D. Persans, and T. G. Bilodeau, “Resonant-Raman-scattering and photoluminescence studies in glass-composite and colloidal CdS”, *Phys. Rev. B*, **1991**, *43*, 15, 12580–12589.
- [27] S. Okamoto, Y. Kanemitsu, H. Hosokawa, K. Murakoshi, and S. Yanagida, “Photoluminescence from surface-capped CdS nanocrystals by selective excitation”, *Solid State Commun.*, **1998**, *105*, 1, 7–11.
- [28] A. Veamatahau, B. Jiang, T. Seifert, S. Makuta, K. Latham, M. Kanehara, T. Teranishi, and Y. Tachibana, “Origin of surface trap states in CdS quantum dots: relationship between size dependent photoluminescence and sulfur vacancy trap states”, *Phys. Chem. Chem. Phys.*, **2015**, *17*, 4, 2850–2858.
- [29] J. C. Slater and G. F. Koster, “Simplified LCAO Method for the Periodic Potential Problem”, *Phys. Rev.*, **1954**, *94*, 6, 1498–1524.
- [30] M. Fox, *Optical Properties of Solids*, Oxford University Press, *2nd ed.*, **2012**.

-
- [31] C. Kittel, *Einführung in die Festkörperphysik*, Oldenbourg, 15th ed., **2013**.
- [32] G. Morello, M. De Giorgi, S. Kudera, L. Manna, R. Cingolani, and M. Anni, “Temperature and Size Dependence of Nonradiative Relaxation and Exciton-Phonon Coupling in Colloidal CdTe Quantum Dots”, *J. Phys. Chem. C*, **2007**, 111, 16, 5846–5849.
- [33] M. Grundmann, *The Physics of Semiconductors an Introduction Including Nanophysics and Applications*, Springer, 4th ed., **2021**.
- [34] A. Nag, A. Hazarika, K. V. Shanavas, S. M. Sharma, I. Dasgupta, and D. D. Sarma, “Crystal Structure Engineering by Fine-Tuning the Surface Energy: The Case of CdE (E = S/Se) Nanocrystals”, *J. Phys. Chem. Lett.*, **2011**, 2, 7, 706–712.
- [35] U. Soni, V. Arora, and S. Sapra, “Wurtzite or zinc blende? Surface decides the crystal structure of nanocrystals”, *CrystEngComm*, **2013**, 15, 27, 5458–5463.
- [36] F. Wang and W. E. Buhro, “Crystal-Phase Control by Solution–Solid–Solid Growth of II–VI Quantum Wires”, *Nano Lett.*, **2016**, 16, 2, 889–894.
- [37] G. H. Wannier, “The Structure of Electronic Excitation Levels in Insulating Crystals”, *Phys. Rev.*, **1937**, 52, 3, 191–197.
- [38] S.-H. Lohmann, P. Harder, F. Bourier, C. Strelow, A. Mews, and T. Kipp, “Influence of Interface-Driven Strain on the Spectral Diffusion Properties of Core/Shell CdSe/CdS Dot/Rod Nanoparticles”, *J. Phys. Chem. C*, **2019**, 123, 8, 5099–5109.
- [39] D. T. I. Broser, R. Broser, H. Finkenrath, R.R. Galazka, H.E. Gumlich, A. Hoffmann, J. Kossut, E. Mollwo, H. Nelkowski, G. Nimtz, W. von der Osten, M. Rosenzweig, H.J. Schulz, D. Theis, *Physics of II–VI and I–VII Compounds, Semimagnetic Semiconductors in Numerical Data and Functional Relationships in Sci*, Springer, **1982**.
- [40] W. Y. Liang, “Excitons”, *Phys. Educ.*, **1970**, 5, 4, 003.
- [41] N. Chestnoy, T. D. Harris, R. Hull, and L. E. Brus, “Luminescence and Photophysics of CdS Semiconductor Clusters: The Nature of the Emitting Electronic State”, *J. Phys. Chem.*, **1986**, 90, 15, 3393–3399.

- [42] A. Hässelbarth, A. Eychmüller, and H. Weller, “Detection of shallow electron traps in quantum sized CdS by fluorescence quenching experiments”, *Chem. Phys. Lett.*, **1993**, 203, 2-3, 271–276.
- [43] D. Krasikov and I. Sankin, “Defect interactions and the role of complexes in the CdTe solar cell absorber”, *J. Mater. Chem. A*, **2017**, 5, 7, 3503–3513.
- [44] K. Shum, “Density of states in semiconductor nanostructures”, *J. Appl. Phys.*, **1991**, 69, 9, 6484–6487.
- [45] A. Rahimi-Iman, *Semiconductor Photonics of Nanomaterials and Quantum Structures*, vol. 196 of *Springer Series in Solid-State Sciences*. Springer, **2021**.
- [46] L. E. Brus, “A simple model for the ionization potential, electron affinity, and aqueous redox potentials of small semiconductor crystallites”, *J. Chem. Phys.*, **1983**, 79, 11, 5566–5571.
- [47] L. Brus, “Electronic wave functions in semiconductor clusters: experiment and theory”, *J. Phys. Chem.*, **1986**, 90, 12, 2555–2560.
- [48] L. E. Brus, “Electron–electron and electron-hole interactions in small semiconductor crystallites: The size dependence of the lowest excited electronic state”, *J. Chem. Phys.*, **1984**, 80, 9, 4403–4409.
- [49] A. M. Smith and S. Nie, “Semiconductor Nanocrystals: Structure, Properties, and Band Gap Engineering”, *Acc. Chem. Res.*, **2010**, 43, 2, 190–200.
- [50] P. Reiss, M. Protière, and L. Li, “Core/Shell Semiconductor Nanocrystals”, *Small*, **2009**, 5, 2, 154–168.
- [51] V. E. Borisenko and S. Ossicini, *What is What in the Nanoworld*, Wiley-VCH, 1st ed., **2004**.
- [52] E. D. Goodwin, B. T. Diroll, S. J. Oh, T. Paik, C. B. Murray, and C. R. Kagan, “Effects of Post-Synthesis Processing on CdSe Nanocrystals and Their Solids: Correlation between Surface Chemistry and Optoelectronic Properties”, *J. Phys. Chem. C*, **2014**, 118, 46, 27097–27105.
- [53] Y. Kobayashi, L. Pan, and N. Tamai, “Effects of Size and Capping Reagents on Biexciton Auger Recombination Dynamics of CdTe Quantum Dots”, *J. Phys. Chem. C*, **2009**, 113, 27, 11783–11789.

- [54] J. R. Lakowicz, *Principles of Fluorescence Spectroscopy*, Springer US, 3rd ed., **2006**.
- [55] A. L. Efros, M. Rosen, M. Kuno, M. Nirmal, D. J. Norris, and M. Bawendi, “Band-edge exciton in quantum dots of semiconductors with a degenerate valence band: Dark and bright exciton states”, *Phys. Rev. B*, **1996**, 54, 7, 4843–4856.
- [56] O. Labeau, P. Tamarat, and B. Lounis, “Temperature Dependence of the Luminescence Lifetime of Single CdSe/ZnS Quantum Dots”, *Phys. Rev. Lett.*, **2003**, 90, 25, 257404.
- [57] L. Biadala, B. Siebers, Y. Beyazit, M. D. Tessier, D. Dupont, Z. Hens, D. R. Yakovlev, and M. Bayer, “Band-Edge Exciton Fine Structure and Recombination Dynamics in InP/ZnS Colloidal Nanocrystals”, *ACS Nano*, **2016**, 10, 3, 3356–3364.
- [58] A. L. Efros, “Almost always bright”, *Nat. Mater.*, **2008**, 7, 8, 612–613.
- [59] C. Galland, Y. Ghosh, A. Steinbrück, M. Sykora, J. A. Hollingsworth, V. I. Klimov, and H. Htoon, “Two types of luminescence blinking revealed by spectroelectrochemistry of single quantum dots”, *Nature*, **2011**, 479, 7372, 203–207.
- [60] A. A. Cordones and S. R. Leone, “Mechanisms for charge trapping in single semiconductor nanocrystals probed by fluorescence blinking”, *Chem. Soc. Rev.*, **2013**, 42, 8, 3209–3221.
- [61] J. Cui, A. P. Beyler, I. Coropceanu, L. Cleary, T. R. Avila, Y. Chen, J. M. Cordero, S. L. Heathcote, D. K. Harris, O. Chen, J. Cao, and M. G. Bawendi, “Evolution of the Single-Nanocrystal Photoluminescence Linewidth with Size and Shell: Implications for Exciton–Phonon Coupling and the Optimization of Spectral Linewidths”, *Nano Lett.*, **2016**, 16, 1, 289–296.
- [62] A. M. Kelley, “Electron–Phonon Coupling in CdSe Nanocrystals”, *J. Phys. Chem. Lett.*, **2010**, 1, 9, 1296–1300.
- [63] A. M. Kelley, “Electron–Phonon Coupling in CdSe Nanocrystals from an Atomistic Phonon Model”, *ACS Nano*, **2011**, 5, 6, 5254–5262.
- [64] D. M. Sagar, R. R. Cooney, S. L. Sewall, E. A. Dias, M. M. Barsan, I. S. Butler, and P. Kambhampati, “Size dependent, state-resolved

- studies of exciton-phonon couplings in strongly confined semiconductor quantum dots”, *Phys. Rev. B*, **2008**, *77*, 23, 235321.
- [65] K. H. Rhys and Avril, “Theory of light absorption and non-radiative transitions in F-centres”, *Proc. R. Soc. London. Ser. A. Math. Phys. Sci.*, **1950**, *204*, 1078, 406–423.
- [66] H. Zhao and H. Kalt, “Energy-dependent Huang-Rhys factor of free excitons”, *Phys. Rev. B*, **2003**, *68*, 12, 125309.
- [67] C. Lin, K. Gong, D. F. Kelley, and A. M. Kelley, “Size-Dependent Exciton-Phonon Coupling in CdSe Nanocrystals through Resonance Raman Excitation Profile Analysis”, *J. Phys. Chem. C*, **2015**, *119*, 13, 7491–7498.
- [68] S. A. Empedocles and M. G. Bawendi, “Quantum-confined stark effect in single CdSe nanocrystallite quantum dots”, *Science*, **1997**, *278*, 5346, 2114–2117.
- [69] S.-H. Lohmann, C. Strelow, A. Mews, and T. Kipp, “Surface Charges on CdSe-Dot/CdS-Rod Nanocrystals: Measuring and Modeling the Diffusion of Exciton-Fluorescence Rates and Energies”, *ACS Nano*, **2017**, *11*, 12, 12185–12192.
- [70] M. J. Fernée, B. Littleton, T. Plakhotnik, H. Rubinsztein-Dunlop, D. E. Gómez, and P. Mulvaney, “Charge hopping revealed by jitter correlations in the photoluminescence spectra of single CdSe nanocrystals”, *Phys. Rev. B*, **2010**, *81*, 15, 155307.
- [71] M. J. Fernée, T. Plakhotnik, Y. Louyer, B. N. Littleton, C. Potzner, P. Tamarat, P. Mulvaney, and B. Lounis, “Spontaneous Spectral Diffusion in CdSe Quantum Dots”, *J. Phys. Chem. Lett.*, **2012**, *3*, 12, 1716–1720.
- [72] M. Bayer, G. Ortner, O. Stern, A. Kuther, A. A. Gorbunov, A. Forchel, P. Hawrylak, S. Fafard, K. Hinzer, T. L. Reinecke, S. N. Walck, J. P. Reithmaier, F. Klopff, and F. Schäfer, “Fine structure of neutral and charged excitons in self-assembled In(Ga)As/(Al)GaAs quantum dots”, *Phys. Rev. B*, **2002**, *65*, 19, 195315.
- [73] M. G. Bawendi, W. L. Wilson, L. Rothberg, P. J. Carroll, T. M. Jedju, M. L. Steigerwald, and L. E. Brus, “Electronic Structure and Photoexcited-Carrier Dynamics in Nanometer-Size CdSe Clusters”, *Phys. Rev. Lett.*, **1990**, *65*, 13, 1623–1626.

-
- [74] H. Bui, A. Karpulevich, and G. Bester, “Excitonic fine structure of zinc-blende and wurtzite colloidal CdSe nanocrystals and comparison to effective mass results”, *Phys. Rev. B*, **2020**, *101*, 11, 115414.
- [75] R. S. Wagner and W. C. Ellis, “VAPOR-LIQUID-SOLID MECHANISM OF SINGLE CRYSTAL GROWTH”, *Appl. Phys. Lett.*, **1964**, *4*, 5, 89–90.
- [76] S. K. C. Lee, Y. Yu, O. Perez, S. Puscas, T. H. Kosel, and M. Kuno, “Bismuth-Assisted CdSe and CdTe Nanowire Growth on Plastics”, *Chem. Mater.*, **2010**, *22*, 1, 77–84.
- [77] F. Wang, W. E. Buhro, W. F., and B. WE, “An Easy Shortcut Synthesis of Size-Controlled Bismuth Nanoparticles and Their Use in the SLS Growth of High-Quality Colloidal Cadmium Selenide Quantum Wires”, *Small*, **2010**, *6*, 4, 573–581.
- [78] F. Wang, A. Dong, J. Sun, R. Tang, H. Yu, and W. E. Buhro, “Solution-Liquid-Solid Growth of Semiconductor Nanowires”, *Inorg. Chem.*, **2006**, *45*, 19, 7511–7521.
- [79] Z. Li, Ö. Kurtulus, N. Fu, Z. Wang, A. Kornowski, U. Pietsch, and A. Mews, “Controlled Synthesis of CdSe Nanowires by Solution–Liquid–Solid Method”, *Adv. Funct. Mater.*, **2009**, *19*, 22, 3650–3661.
- [80] E. A. Olson, M. Y. Efremov, M. Zhang, Z. Zhang, and L. H. Allen, “Size-dependent melting of Bi nanoparticles”, *J. Appl. Phys.*, **2005**, *97*, 3, 034304.
- [81] Z. Li, A. Kornowski, A. Myalitsin, and A. Mews, “Formation and Function of Bismuth Nanocatalysts for the Solution-Liquid-Solid Synthesis of CdSe Nanowires”, *Small*, **2008**, *4*, 10, 1698–1702.
- [82] Y. Yin and A. P. Alivisatos, “Colloidal nanocrystal synthesis and the organic–inorganic interface”, *Nature*, **2005**, *437*, 7059, 664–670.
- [83] A. Puzder, A. J. Williamson, N. Zaitseva, G. Galli, L. Manna, and A. P. Alivisatos, “The Effect of Organic Ligand Binding on the Growth of CdSe Nanoparticles Probed by Ab Initio Calculations”, *Nano Lett.*, **2004**, *4*, 12, 2361–2365.
- [84] X. Peng, L. Manna, W. Yang, J. Wickham, E. Scher, A. Kadavanich, and A. P. Alivisatos, “Shape control of CdSe nanocrystals”, *Nature*, **2000**, *404*, 6773, 59–61.
-

- [85] W. Wang, S. Banerjee, S. Jia, M. L. Steigerwald, and I. P. Herman, “Ligand Control of Growth, Morphology, and Capping Structure of Colloidal CdSe Nanorods”, *Chem. Mater.*, **2007**, *19*, 10, 2573–2580.
- [86] F. Wang and W. E. Buhro, “Role of Precursor-Conversion Chemistry in the Crystal-Phase Control of Catalytically Grown Colloidal Semiconductor Quantum Wires”, *ACS Nano*, **2017**, *11*, 12, 12526–12535.
- [87] F. Wang and W. E. Buhro, “Morphology Control of Cadmium Selenide Nanocrystals: Insights into the Roles of Di-*n*-octylphosphine Oxide (DOPO) and Di-*n*-octylphosphinic Acid (DOPA)”, *J. Am. Chem. Soc.*, **2012**, *134*, 11, 5369–5380.
- [88] P. Harder, A. Nielsen, A.-K. Sassnau, D. Bonatz, M. Perbandt, T. Kipp, and A. Mews, “Determination of the Wurtzite and Zinblende Fractions in II–VI Semiconductor Nanowires”, *Chem. Mater.*, **2021**, *33*, 3, 1061–1069.
- [89] N. C. Anderson, M. P. Hendricks, J. J. Choi, and J. S. Owen, “Ligand Exchange and the Stoichiometry of Metal Chalcogenide Nanocrystals: Spectroscopic Observation of Facile Metal-Carboxylate Displacement and Binding”, *J. Am. Chem. Soc.*, **2013**, *135*, 49, 18536–18548.
- [90] J. M. Azpiroz and F. De Angelis, “Ligand Induced Spectral Changes in CdSe Quantum Dots”, *ACS Appl. Mater. Interfaces*, **2015**, *7*, 35, 19736–19745.
- [91] H. Zhang, J. Jang, W. Liu, and D. V. Talapin, “Colloidal Nanocrystals with Inorganic Halide, Pseudohalide, and Halometallate Ligands”, *ACS Nano*, **2014**, *8*, 7, 7359–7369.
- [92] A. Hazarika, I. Fedin, L. Hong, J. Guo, V. Srivastava, W. Cho, I. Coropceanu, J. Portner, B. T. Diroll, J. P. Philbin, E. Rabani, R. Klie, and D. V. Talapin, “Colloidal Atomic Layer Deposition with Stationary Reactant Phases Enables Precise Synthesis of “Digital” II–VI Nano-heterostructures with Exquisite Control of Confinement and Strain”, *J. Am. Chem. Soc.*, **2019**, *141*, 34, 13487–13496.
- [93] N. E. Richey, C. de Paula, and S. F. Bent, “Understanding chemical and physical mechanisms in atomic layer deposition”, *J. Chem. Phys.*, **2020**, *152*, 4, 040902.

-
- [94] M. Green, "A new approach to the formal classification of covalent compounds of the elements", *J. Organomet. Chem.*, **1995**, *500*, 1-2, 127–148.
- [95] Y. Zhou and Y. Wang, *Perovskite Quantum Dots*, Springer, **2020**.
- [96] H. Sun and W. E. Buhro, "Contrasting Ligand-Exchange Behavior of Wurtzite and Zinc-Blende Cadmium Telluride Nanoplatelets", *Chem. Mater.*, **2021**, *33*, 5, 1683–1697.
- [97] J. De Roo, K. De Keukeleere, Z. Hens, and I. Van Driessche, "From ligands to binding motifs and beyond; the enhanced versatility of nanocrystal surfaces", *Dalt. Trans.*, **2016**, *45*, 34, 13277–13283.
- [98] R. G. Pearson, "Hard and Soft Acids and Bases, HSAB, Part 1: Fundamental principles", *J. Chem. Educ.*, **1968**, *45*, 9, 581–587.
- [99] W. Wang, Z. Pan, H. Rao, G. Zhang, H. Song, Z. Zhang, and X. Zhong, "Proton Initiated Ligand Exchange Reactions for Colloidal Nanocrystals Functionalized by Inorganic Ligands with Extremely Weak Coordination Ability", *Chem. Mater.*, **2020**, *32*, 1, 630–637.
- [100] N. Razgoniaeva, L. Carrillo, D. Burchfield, P. Moroz, P. Adhikari, P. Yadav, D. Khon, and M. Zamkov, "Colloidal Synthesis of Monodisperse Semiconductor Nanocrystals through Saturated Ionic Layer Adsorption", *Chem. Mater.*, **2016**, *28*, 8, 2823–2833.
- [101] N. Naredi-Rainer, J. Prescher, A. Hartschuh, and D. C. Lamb, *Confocal Microscopy in Fluorescence Microscopy*, Wiley-VCH, *1st ed.*, **2013**.
- [102] G. B. Airy, "On the Diffraction of an Object-glass with Circular Aperture", *Trans. Cambridge Philos. Soc.*, **1835**, *5*, 283.
- [103] R. W. Cole, T. Jinadasa, and C. M. Brown, "Measuring and interpreting point spread functions to determine confocal microscope resolution and ensure quality control", *Nat. Protoc.*, **2011**, *6*, 12, 1929–1941.
- [104] L. Novotny and B. Hecht, *Principles of Nano-Optics*, Cambridge University Press, *2nd ed.*, **2012**.
- [105] R. H. Webb, "Confocal optical microscopy", *Rep. Prog. Phys.*, **1996**, *59*, 427–471.
-

- [106] G. Brooker, *Modern Classical Optics*, Oxford University Press, 1st ed., **2003**.
- [107] A. Systems, *User Manual, attocube systems pulse tube cooling system*, attocube, **2010**.
- [108] M. T. A. Linnemann, S. Kühl, B. Ilsinger, S. Lenz, *Grundlagen der Licht- und Elektronenmikroskopie*, Verlag Eugen Ulmer, 1st ed., **2018**.
- [109] D. B. Williams and C. B. Carter, *Transmission Electron Microscopy*, Springer, 2nd ed., **2009**.
- [110] D. B. Williams and C. B. Carter, *Amplitude Contrast in Transmission Electron Microscopy*, Springer, 2nd ed., **2009**.
- [111] D. J. Smith, *High Resolution Transmission Electron Microscopy in Handbook of Microscopy for Nanotechnology*, Springer US, 1st ed., **2005**.
- [112] T. Oku, *Structure Analysis of Advanced Nanomaterials*, De Gruyter, 1st ed., **2014**.
- [113] J. Liu, *High-Resolution Scanning Electron Microscopy in Handbook of Microscopy for Nanotechnology*, Springer US, 1st ed., **2005**.
- [114] G. Binnig, C. F. Quate, and C. Gerber, “Atomic Force Microscope”, *Phys. Rev. Lett.*, **1986**, 56, 9, 930–933.
- [115] E. Meyer, “Atomic force microscopy”, *Prog. Surf. Sci.*, **1992**, 41, 1, 3–49.
- [116] R. García and R. Pérez, “Dynamic atomic force microscopy methods”, *Surf. Sci. Rep.*, **2002**, 47, 6-8, 197–301.
- [117] A. Schirmeisen, B. Anczykowski, and H. Fuchs, *Dynamic Modes of Atomic Force Microscopy in Springer Handbook of Nanotechnology*, Springer, **2007**.
- [118] W. H. Bragg and W. L. Bragg, “The Reflection of X-rays by Crystals”, *Proc. R. Soc. London. Ser. A*, **1913**, 88, 428–438.
- [119] R. E. Dinnebier and S. J. L. Billinge, *Chapter 1. Principles of Powder Diffraction in Powder Diffraction: Theory and Practice*, Royal Society of Chemistry, 1st ed., **2008**.

- [120] Ö. Kurtuluş, Z. Li, A. Mews, and U. Pietsch, “X-ray investigation of CdSe nanowires”, *Phys. Status Solidi A*, **2009**, *206*, 8, 1752–1756.
- [121] M. Haschke, *XRF-Basics in Laboratory Micro-X-Ray Fluorescence Spectroscopy*, Springer International Publishing, *1st ed.*, **2014**.
- [122] B. Beckhoff, B. Kanngießer, N. Langhoff, R. Wedell, and H. Wolff, *Handbook of Practical X-Ray Fluorescence Analysis*, Springer, *1st ed.*, **2006**.
- [123] R. Jenkins, R. Manne, R. Robin, and C. Senemaud, “IUPAC—nomenclature system for x-ray spectroscopy”, *X-Ray Spectrom.*, **1991**, *20*, 3, 149–155.
- [124] M. Van Gysel, P. Lemberge, and P. Van Espen, “Description of Compton peaks in energy-dispersive x-ray fluorescence spectra”, *X-Ray Spectrom.*, **2003**, *32*, 2, 139–147.
- [125] C. Ziska, C. Ossig, N. Pyrlík, R. Carron, E. Avancini, G. Fevola, A. Kolditz, J. Siebels, T. Kipp, Z. Cai, M. V. Holt, and M. E. Stuckelberger, “Quantifying the Elemental Distribution in Solar Cells from X-Ray Fluorescence Measurements with Multiple Detector Modules”, in *2020 47th IEEE Photovolt. Spec. Conf.*, pp. 1085–1092, IEEE, jun 2020.
- [126] T.-K. Sham and R. A. Rosenberg, “Time-Resolved Synchrotron Radiation Excited Optical Luminescence: Light-Emission Properties of Silicon-Based Nanostructures”, *ChemPhysChem*, **2007**, *8*, 18, 2557–2567.
- [127] C. A. Klein, “Bandgap Dependence and Related Features of Radiation Ionization Energies in Semiconductors”, *J. Appl. Phys.*, **1968**, *39*, 4, 2029–2038.
- [128] M. Stuckelberger, B. West, T. Nietzold, B. Lai, J. M. Maser, V. Rose, and M. I. Bertoni, “Engineering solar cells based on correlative X-ray microscopy”, *J. Mater. Res.*, **2017**, *32*, 10, 1825–1854.
- [129] C. Ossig, T. Nietzold, B. West, M. Bertoni, G. Falkenberg, C. G. Schroer, and M. E. Stuckelberger, “X-ray Beam Induced Current Measurements for Multi-Modal X-ray Microscopy of Solar Cells”, *J. Vis. Exp.*, **2019**, 150, e60001.

- [130] C. Ossig, C. Strelow, J. Flügge, A. Kolditz, J. Siebels, J. Garrevoet, K. Spiers, M. Seyrich, D. Brückner, N. Pyrlík, J. Hagemann, F. Seiboth, A. Schropp, R. Carron, G. Falkenberg, A. Mews, C. Schroer, T. Kipp, and M. Stuckelberger, “Four-Fold Multi-Modal X-ray Microscopy Measurements of a Cu(In,Ga)Se₂ Solar Cell”, *MDPI Mater.*, **2021**, *14*, 1, 228.
- [131] I. Lokteva, N. Radychev, F. Witt, H. Borchert, J. Parisi, and J. Kolny-Olesiak, “Surface Treatment of CdSe Nanoparticles for Application in Hybrid Solar Cells: The Effect of Multiple Ligand Exchange with Pyridine”, *J. Phys. Chem. C*, **2010**, *114*, 29, 12784–12791.
- [132] R. P. Winarski, M. V. Holt, V. Rose, P. Fuesz, D. Carbaugh, C. Benson, D. Shu, D. Kline, G. Brian Stephenson, I. McNulty, and J. Maser, “A hard X-ray nanoprobe beamline for nanoscale microscopy”, *J. Synchrotron Radiat.*, **2012**, *19*, 6, 1056–1060.
- [133] C. G. Schroer, P. Boye, J. M. Feldkamp, J. Patommel, D. Samberg, A. Schropp, A. Schwab, S. Stephan, G. Falkenberg, G. Wellenreuther, and N. Reimers, “Hard X-ray nanoprobe at beamline P06 at PETRA III”, *Nucl. Instruments Methods Phys. Res. Sect. A Accel. Spectrometers, Detect. Assoc. Equip.*, **2010**, *616*, 2-3, 93–97.
- [134] C. Ziska, *Analysis of Synchrotron-Based X-Ray Fluorescence Measurements from Multiple Detector Modules*. Bachelor’s thesis, Universität Hamburg, **2020**.
- [135] A. J. Reich, *Single charge carrier-defect complexes in CdSe and CdS nanowires observed by photoluminescence spectroscopy*. Dissertation, Universität Hamburg, **2019**.
- [136] F. Wang, R. Tang, and W. E. Buhro, “The Trouble with TOPO; Identification of Adventitious Impurities Beneficial to the Growth of Cadmium Selenide Quantum Dots, Rods, and Wires”, *Nano Lett.*, **2008**, *8*, 10, 3521–3524.
- [137] M. Meyns, F. Iacono, C. Palencia, J. Geweke, M. D. Coderch, U. E. Fittschen, J. M. Gallego, R. Otero, B. H. Juárez, and C. Klinke, “Shape Evolution of CdSe Nanoparticles Controlled by Halogen Compounds”, *Chem. Mater.*, **2014**, *26*, 5, 1813–1821.
- [138] F. Gerdes, C. Navío, B. H. Juárez, and C. Klinke, “Size, Shape, and

-
- Phase Control in Ultrathin CdSe Nanosheets”, *Nano Lett.*, **2017**, *17*, 7, 4165–4171.
- [139] F. Gerdes, E. Klein, S. Kull, M. M. Ramin Moayed, R. Lesyuk, and C. Klinke, “Halogens in the Synthesis of Colloidal Semiconductor Nanocrystals”, *Zeitschrift für Phys. Chemie*, **2018**, *232*, 9-11, 1267–1280.
- [140] P.-C. Harder, *Methode zur Bestimmung der Kristallstruktur von Nanodrähten*. Dissertation, Universität Hamburg, **2020**.
- [141] F. Johst, *Synthese und Charakterisierung von Cadmiumtellurid-Nanodrähten und deren Vorläuferverbindungen*. Bachelor’s thesis, Universität Hamburg, **2018**.
- [142] M. Zhao, M. Bosman, M. Danesh, M. Zeng, P. Song, Y. Darma, A. Rusydi, H. Lin, C. W. Qiu, and K. P. Loh, “Visible Surface Plasmon Modes in Single Bi₂Te₃ Nanoplate”, *Nano Lett.*, **2015**, *15*, 12, 8331–8335.
- [143] F. Molva, J. P. Chamonal, and J. L. Pautrat, “Shallow Acceptors in Cadmium Telluride”, *Phys. status solidi*, **1982**, *109*, 2, 635–644.
- [144] E. Lifshitz, “Evidence in Support of Exciton to Ligand Vibrational Coupling in Colloidal Quantum Dots”, *J. Phys. Chem. Lett.*, **2015**, *6*, 21, 4336–4347.
- [145] B. von Holt, S. Kudera, A. Weiss, T. E. Schrader, L. Manna, W. J. Parak, and M. Braun, “Ligand exchange of CdSe nanocrystals probed by optical spectroscopy in the visible and mid-IR”, *J. Mater. Chem.*, **2008**, *18*, 23, 2728–2732.
- [146] A. G. Young, N. Al-Salim, D. P. Green, and A. J. McQuillan, “Attenuated Total Reflection Infrared Studies of Oleate and Trioctylphosphine Oxide Ligand Adsorption and Exchange Reactions on CdS Quantum Dot Films”, *Langmuir*, **2008**, *24*, 8, 3841–3849.
- [147] J. E. Bowen Katari, V. L. Colvin, and A. P. Alivisatos, “X-ray Photoelectron Spectroscopy of CdSe Nanocrystals with Applications to Studies of the Nanocrystal Surface”, *J. Phys. Chem.*, **1994**, *98*, 15, 4109–4117.
- [148] M. Green, “The nature of quantum dot capping ligands”, *J. Mater. Chem.*, **2010**, *20*, 28, 5797–5809.
-

- [149] A. Ghatak, G. H. Debnath, M. Mandal, and P. Mukherjee, “Lanthanide cation-induced tuning of surface capping properties in zinc sulfide nanoparticles: an infrared absorption study”, *RSC Adv.*, **2015**, *5*, 42, 32920–32932.
- [150] J. S. Owen, J. Park, P. E. Trudeau, and A. P. Alivisatos, “Reaction Chemistry and Ligand Exchange at Cadmium-Selenide Nanocrystal Surfaces”, *J. Am. Chem. Soc.*, **2008**, *130*, 37, 12279–12281.
- [151] A. Hassinen, R. Gomes, K. De Nolf, Q. Zhao, A. Vantomme, J. C. Martins, and Z. Hens, “Surface Chemistry of CdTe Quantum Dots Synthesized in Mixtures of Phosphonic Acids and Amines: Formation of a Mixed Ligand Shell”, *J. Phys. Chem. C*, **2013**, *117*, 27, 13936–13943.
- [152] F. Wang, R. Tang, J. L.-F. Kao, S. D. Dingman, and W. E. Buhro, “Spectroscopic Identification of Tri-*n*-octylphosphine Oxide (TOPO) Impurities and Elucidation of Their Roles in Cadmium Selenide Quantum-Wire Growth”, *J. Am. Chem. Soc.*, **2009**, *131*, 13, 4983–4994.
- [153] L.-F. Liao, C.-F. Lien, and J.-L. Lin, “FTIR study of adsorption and photoreactions of acetic acid on TiO₂”, *Phys. Chem. Chem. Phys.*, **2001**, *3*, 17, 3831–3837.
- [154] Sigma-Aldrich, <https://www.sigmaaldrich.com/DE/en>, accessed 2021-07-07.
- [155] A. Vega, P. Thissen, and Y. J. Chabal, “Environment-Controlled Tethering by Aggregation and Growth of Phosphonic Acid Monolayers on Silicon Oxide”, *Langmuir*, **2012**, *28*, 21, 8046–8051.
- [156] T. Noblet, L. Dreesen, S. Boujday, C. Methivier, B. Busson, A. Tadjeddine, and C. Humbert, “Semiconductor quantum dots reveal dipolar coupling from exciton to ligand vibration”, *Commun. Chem.*, **2018**, *1*, 76.
- [157] B. R. Watson, Y. Z. Ma, J. F. Cahill, B. Doughty, and T. R. Calhoun, “Probing ligand removal and ordering at quantum dot surfaces using vibrational sum frequency generation spectroscopy”, *Journal of Colloid and Interface Science*, **2019**, *537*, 389–395.
- [158] R. D. Harris, S. Bettis Homan, M. Kodaimati, C. He, A. B. Nepomnyashchii, N. K. Swenson, S. Lian, R. Calzada, and E. A. Weiss,

- “Electronic Processes within Quantum Dot-Molecule Complexes”, *Chemical Reviews*, **2016**, *116*, 21, 12865–12919.
- [159] M. V. Kovalenko, M. Scheele, and D. V. Talapin, “Colloidal Nanocrystals with Molecular Metal Chalcogenide Surface Ligands”, *Science (80-.)*, **2009**, *324*, 5933, 1417–1420.
- [160] C. Pu and X. Peng, “To Battle Surface Traps on CdSe/CdS Core/Shell Nanocrystals: Shell Isolation versus Surface Treatment”, *J. Am. Chem. Soc.*, **2016**, *138*, 26, 8134–8142.
- [161] J. J. Li, Y. A. Wang, W. Guo, J. C. Keay, T. D. Mishima, M. B. Johnson, and X. Peng, “Large-Scale Synthesis of Nearly Monodisperse CdSe/CdS Core/Shell Nanocrystals Using Air-Stable Reagents via Successive Ion Layer Adsorption and Reaction”, *J. Am. Chem. Soc.*, **2003**, *125*, 41, 12567–12575.
- [162] A. I. Ekimov, F. Hache, M. C. Schanne-Klein, D. Ricard, C. Flytzanis, I. A. Kudryavtsev, T. V. Yazeva, A. V. Rodina, and A. L. Efros, “Absorption and intensity-dependent photoluminescence measurements on CdSe quantum dots: assignment of the first electronic transitions”, *J. Opt. Soc. Am. B*, **1993**, *10*, 1, 100–107.
- [163] S. Grunewald, *Kolloidale Atomlagenabscheidung (c-ALD) an Halbleiternanodrähten*. Master’s thesis, Universität Hamburg, **2019**.
- [164] Z. Li, X. Ma, Q. Sun, Z. Wang, J. Liu, Z. Zhu, S. Z. Qiao, S. C. Smith, G. M. Lu, and A. Mews, “Synthesis and Characterization of Colloidal Core–Shell Semiconductor Nanowires”, *Eur. J. Inorg. Chem.*, **2010**, *27*, 4325–4331.
- [165] L. Manna, E. C. Scher, and A. P. Alivisatos, “Synthesis of Soluble and Processable Rod-, Arrow-, Teardrop-, and Tetrapod-Shaped CdSe Nanocrystals”, *J. Am. Chem. Soc.*, **2000**, *122*, 51, 12700–12706.
- [166] J. E. Prieto and I. Markov, “Stranski–Krastanov mechanism of growth and the effect of misfit sign on quantum dots nucleation”, *Surf. Sci.*, **2017**, *664*, 172–184.
- [167] S. Karan, M. Majumder, and B. Mallik, “Controlled surface trap state photoluminescence from CdS QDs impregnated in poly(methyl methacrylate)”, *Photochem. Photobiol. Sci.*, **2012**, *11*, 7, 1220–1232.

- [168] J. J. Ramsden and M. Grätzel, “Photoluminescence of Small Cadmium Sulphide Particles”, *J. Chem. Soc. Faraday Trans. 1*, **1984**, *80*, 4, 919–933.
- [169] T. Schmaltz, A. Khassanov, H.-G. Steinrück, A. Magerl, A. Hirsch, and M. Halik, “Tuning the molecular order of C₆₀-based self-assembled monolayers in field-effect transistors”, *Nanoscale*, **2014**, *6*, 21, 13022–13027.
- [170] H. Liu, “Tuning the Binding Energy of Surfactant to CdSe Nanocrystal: A Theoretical Study”, *J. Phys. Chem. C*, **2009**, *113*, 8, 3116–3119.
- [171] J. I. Kim and J. K. Lee, “Sub-kilogram-Scale One-Pot Synthesis of Highly Luminescent and Monodisperse Core/Shell Quantum Dots by the Successive Injection of Precursors”, *Adv. Funct. Mater.*, **2006**, *16*, 16, 2077–2082.
- [172] Z. A. Peng and X. Peng, “Mechanisms of the shape evolution of CdSe nanocrystals”, *J. Am. Chem. Soc.*, **2001**, *123*, 7, 1389–1395.
- [173] A.-K. Sassnau, *Synthese eindimensionaler Nanostrukturen nach der Solution-Liquid-Solid-Methode und deren strukturelle und optische Charakterisierung*. Dissertation, Universität Hamburg, **2019**.
- [174] Y. Spanhel, M. Haase, H. Weller, and A. Hengleir, “Photochemistry of colloidal semiconductors. 20. Surface modification and stability of strong luminescing CdS particles”, *J. Am. Chem. Soc.*, **1987**, *109*, 19, 5649–5655.
- [175] G. S. Paul, P. Gogoi, and P. Agarwal, “Structural and stability studies of CdS and SnS nanostructures synthesized by various routes”, *J. Non. Cryst. Solids*, **2008**, *354*, 19-25, 2195–2199.
- [176] B. Ravel and M. Newville, “*ATHENA*, *ARTEMIS*, *HEPHAESTUS*: data analysis for X-ray absorption spectroscopy using *IFEFFIT*”, *J. Synchrotron Radiat.*, **2005**, *12*, 4, 537–541.
- [177] M. E. Stuckelberger, T. Nietzold, B. West, R. Farshchi, D. Poplavskyy, J. Bailey, B. Lai, J. M. Maser, and M. I. Bertoni, “Understanding the activation and annihilation of nanoscopic defects in CIGS solar cells by X-ray microscopy”, tech. rep., 2019.







Appendices

A Safety and Disposal








Safety Instructions of the Utilized Substances










The safety instructions of the utilized chemicals with their respective pictograms, hazard and precautionary statements according to the Globally Harmonized System of Classification and Labeling of Chemicals (GHS) are listed in Table A.1. ^[154]

Table A.1: Safety instructions of the utilized chemicals and their disposal.

Substance	Pictograms	Hazard Statements	Precautionary Statements
Acetone	 danger	225-319-336 EUH066	210- 305+351+338
BiCl ₃	 warning	315-319	302+352 305+351+338
1-Bromo heptane	 warning	226	-
Cd(ac) ₂	 danger	302-312-332- 350-410	201-261-273- 208-308+313- 501
CdO	 danger	330-341-350- 361fd-372-410-	201-202-260-264- 273-304+340+310
1-Chloro heptane	 warning	226	210-370+378

Appendices

Substance	Pictograms	Hazard Statements	Precautionary Statements
DOP		Not classified in accordance with GHS	
DOPA	 warning	319	305+351+338
DOPO		Not classified in accordance with GHS	
Hexane	 danger	225-304-315-336- 361f-373-411	201-210-273- 301+310+331- 302+352-308+313
1-Iodo heptane	-	-	-
Li[N(SiMe ₃) ₂]	 danger	228-314- EUH014	210-260-280 301+330+331- 303+361+353- 305+351+338
Methanol	 danger	225-301+311+331- 370	210-233-280- 301+310+330 302+352-312- 304+340+311
ODE	 danger	304-EUH066	301+330-331
Octanoic acid	 danger	314-412	273-280- 301+330+331- 303+361+353 305+351+338+310
ODPA	-	-	-
OPA	 danger	302-314-373	280 305+351+338 310

Substance	Pictograms	Hazard Statements	Precautionary Statements
PHD- <i>co</i> -PVP	-	-	-
Propan-2-ol	 danger	225-319-336	210- 305+351+338
Pyridin	 danger	225-302+312+332- 315-319	210-280- 301+312 303+361+353
Selenium	 danger	301-331-373-413	260-264-273- 301+310- 304+340+311-314
Sulfur	 warning	228-315	210-240+241 264-280-302+352
Tellurium	 danger	317-332-360-412	201-273-280- 302+352- 304+340+312- 308+313
TDPA	-	-	-
THF	 danger	225-302-319 335-336-351	201-210 301+312+330 305+351+338 308+313
TOP	 danger	314	280-301+330+331- 303+361+353- 305+351+338
TOPO	 danger	315-318-412	273-280- 305+351+338+310
Toluene	 danger	225-304-315- 361d-373-412	201-210-273- 301+310+331- 302+352-308+313

Hazard Statements

Nature of hazards attributed to dangerous substances and mixtures:

H225	Highly flammable liquid and vapour.
H226	Flammable liquid and vapour.
H228	Flammable solid.
H301	Toxic if swallowed.
H301+H311+H331	Toxic if inhaled.
H302	Harmful if swallowed.
H302+H312+H332	Suspected of causing genetic defects.
H304	May be fatal if swallowed and enters airways.
H312	Harmful in contact with skin.
H314	Causes severe skin burns and eye damage.
H315	Causes skin irritation.
H317	May cause an allergic skin reaction.
H318	Causes serious eye damage.
H319	Causes serious eye irritation.
H330	Fatal if inhaled.
H331	Toxic if inhaled.
H332	Harmful if inhaled.
H335	May cause respiratory irritation.
H336	May cause drowsiness or dizziness.
H340	May cause genetic defects.
H341	Suspected of causing genetic defects.
H350	May cause cancer.
H351	Suspected of causing cancer.
H360	May damage fertility or the unborn child.
H361d	Suspected of damaging the unborn child.
H361f	Suspected of damaging fertility.
H361fd	Suspected of damaging fertility. Suspected of damaging the unborn child.
H370	Causes damage to organs.
H372	Causes damage to organs through prolonged or repeated exposure.
H373	May cause damage to organs through prolonged or repeated exposure.
H410	Very toxic to aquatic life with long lasting effects.
H411	Toxic to aquatic life with long lasting effects.
H412	Harmful to aquatic life with long lasting effects.
H413	May cause long lasting harmful effects to aquatic life.
EUH014	Reacts violently with water.
EUH066	Repeated exposure may cause skin dryness or cracking.

Precautionary Statements

Precautionary statements concerning dangerous substances and mixtures used during the course of this thesis:^[154]

P201	Obtain special instructions before use.
P260	Do not breathe dust/fume/gas/mist/vapours/spray.
P264	Wash . . . thoroughly after handling.
P270	Do not eat, drink or smoke when using this product.
P273	Avoid release to the environment.
P280	Wear protective gloves/protective clothing/eye protection/face protection.
P301+P310	IF SWALLOWED: Immediately call a POISON CENTER or doctor/physician.
P301+P312	IF SWALLOWED: Call a POISON CENTER or doctor/physician if you feel unwell.
P301+P312+P330	IF SWALLOWED: Call a POISON CENTER or doctor/physician if you feel unwell. Rinse mouth.
P301+P310+P331	IF SWALLOWED: Immediately call a POISON CENTER or doctor/physician. Do NOT induce vomiting.
P301+P330+P331	IF SWALLOWED: rinse mouth. Do NOT induce vomiting.
P302+P352	IF ON SKIN: Wash with plenty of soap and water.
P303+P361+P353	IF ON SKIN (or hair): Remove/Take off immediately all contaminated clothing. Rinse skin with water/shower.
P304+P340	IF INHALED: Remove victim to fresh air and keep at rest in a position comfortable for breathing.
P304+P340+P310	IF INHALED: Remove victim to fresh air and keep at rest in a position comfortable for breathing. Immediately call a POISON CENTER or doctor/physician.
P305+P351+P338	IF IN EYES: Rinse cautiously with water for several minutes. Remove contact lenses, if present and easy to do. Continue rinsing.
P308+P310	IF exposed or concerned: Immediately call a POISON CENTER or doctor/physician.
P308+P313	IF exposed or concerned: Get medical advice/attention.
P314	Get medical advice/attention if you feel unwell.
P370+P378	In case of fire: Use . . . for extinction.
P403+P233	Store in a well-ventilated place. Keep container tightly closed.

B Conference Contributions

- 2017 **Frühjahrstagung der Deutschen Physikalischen Gesellschaft**, Dresden, Germany
S. Patjens, A. Nielsen, P. Harder, T. Kipp, A. Mews
Talk: *Spectroscopic Properties of CdTe Quantum Wires at Cryogenic Temperatures*
- 2017 **NaNaX 8**, Braga, Portugal
S. Patjens, P. Harder, A. Nielsen, C. Strelow, T. Kipp, A. Mews
Poster: *Structural- and Size-Dependent Photoluminescence of CdTe Nanowires*
- 2018 **Frühjahrstagung der Deutschen Physikalischen Gesellschaft**, Berlin, Germany
S. Patjens, A. Nielsen, P. Harder, T. Kipp, A. Mews
Talk: *Spectroscopic Properties of Semiconductor Quantum Wires at Cryogenic Temperatures*
- 2019 **NaNaX 9**, Hamburg, Germany
S. Patjens, C. Strelow, T. Kipp, A. Mews
Poster: *Spectroscopic Properties of Cadmium Telluride Quantum Wires at Cryogenic Temperatures*

C Acknowledgments

I would like to express my special thanks to the many persons who have supported me in conducting my research and ultimately concluding this work. I would like to especially thank:

- Prof. Dr. Alf Mews giving me the opportunity to work on this interesting project under his supervision and the assessment of this dissertation,
- Prof. Dr. Christian Klinke for conducting the second assessment,
- PD Dr. Tobias Kipp and Dr. Christian Strelow for the fruitful discussions and the introduction to laser-based microscopy,
- Dr. Michael Stückelberger for the collaboration on past and ongoing projects and the unceasing support,
- The beamline staff of the microprobe endstation P06 at PETRA III (Deutsches Elektronen-Synchrotron),
- The beamline staff of nanoprobe endstation 26-ID-C at APS (Argonne National Laboratory),
- Dipl.-Ing. Jan Flügge for the continuous assistance with the setups.
- The entire working group the great atmosphere and many interesting collaborations and side-projects,
- FS-PETRA at DESY for introducing me to X-ray science and the many beamtimes already conducted or planned,
- Dr. Tobias Redder, Dr. Ann-Kathrin Sassnau as well as Dr. Charlotte Ruhmlieb for conducting electron microscopy and Andreas Kornowski for HR-TEM imaging. Dr. Thomas Hackl and Ute Gralla for conducting the NMR and FTIR analyses, respectively,
- Andreas Kolditz, Jan Siebels and Nicklas Giese for supporting the EBL-based sample-preparation procedure,
- Dr. Christina Ossig and Catharina Ziska for evaluating the XRF-data,
- Dr. Andreas Nielsen, Dr. Philip Harder, Dr. Ann-Katrin Sassnau and Sara Grunewald for the joint effort and the collaboration with respect to the NW-project,

- Dr. Maximilian Schwarz, Dr. Jannik Rebmann and Dr. Christina Ossig for in-office and out-of-office support and many joint excursions,
- my interns, bachelor and master students, Alexander Meinhardt, Leroy Nack, Fabian Flocken, Stephan Kleine-Doepke, Florian Johst, Artur Strelnikov, Sara Grunewald as well as Sebastian Schüttler and Kathrin Raeker,
- Kolja Funck for the unconditional support, the confidence in me and for always encouraging me,
- my parents, Antje and Günter, and Maiko Patjens for perpetually motivating me and for always being there.

D Eidesstattliche Erklärung

Hiermit versichere ich an Eides statt, die vorliegende Dissertation selbst verfasst und keine anderen als die angegebenen Hilfsmittel benutzt zu haben. Die eingereichte schriftliche Fassung entspricht der auf dem elektronischen Speichermedium. Ich versichere, dass diese Dissertation nicht in einem früheren Promotionsverfahren eingereicht wurde.

Ort, Datum

Svenja Patjens